博士論文

Mechanism of separated-flow control over an airfoil with synthetic jet devices in low-Reynolds-number regime

（低レイノルズ数域におけるシンセティックジェットを用いた翼周り剥離流れ制御のメカニズム）

阿部　圭晃

Abstract

To date, the separation control devices such as flap and vortex generetors have been well developed for practical use, which can enhance the aerodynamic performances of airfoils when the flow is separated. However, it is difficult to propose the further better design for these devices because of its heavy weight and complicated machine mechanism or the property of essentially passive control which only works well at a certain condition of the separated flow. For these reason, the micro devices such as a synthetic jet (SJ) and DBD plasma actuator (DBDPA) are focused on, which are small, less energy consuming, and able to conduct an active control based on the surrounding flow conditions. The SJ consists of the cavity and orifice embedded in the airfoil surface, of which bottom oscillates periodically using a speaker and piezo devices. The resultant periodic flow fluctuation affects the external separated flow, which is suppressed to the attached or less separated flow. A lot of researchers have tucklled on the practical use of the SJ for decades, where the optimal control parameters have been surveyed for the separation control over an airfoil. Nevertheless, the mechanism of the separation control has not been adequately clarified so that it is difficult to suggest the optimal parameters for variety of separated flow conditions. For example, there have been two regimes of the optimal actuation frequency, i.e., $F^+ = O(1)$ and $O(10)$ (F^+ is the actuation frequency normalized by the chord length and uniform flow velocity). The former frequency $F^+ = O(1)$ is reported to be optimal in terms of the higher lift coefficient; on the other hand, the latter frequency $F^+ = O(10)$ is shown to be better because it directly affects the smaller vortex structures in the view point of turbulent transition. The objective of this study is to clarify the mechanism of separation control using the SJ, which can support construction of the criteria for optimal parameters. In this study, a large-eddy simulation is conducted for the highly-accurate unsteady computation because strong turbulent vortex structures are introduced from the SJ. In addition, the oscillation of the cavity bottom is considered using the moving and deforming grids. The target flow is around the NACA0015 airfoil with the chord-Reynolds number 63,000 at the angle of attack 12°, which is completely separated near the leading edge. The SJ is modelled by the simple cavity with a spanwise-uniform shape, which is implemented at the leading edge. The mechanism of the separation control around an airfoil with a synthetic jet device is investigated using high-fidelity computation.

The new methodology for high-order computation of compressible flows on moving and deforming grid is generally constructed in terms of a freestream preservation and conservation of conservative quantities. The scheme includes new evaluations of time metrics and the Jacobian defined as the component of coordinate-transformation matrix when the body-fitted coordinate is adopted. The new form of time metrics and Jacobian, i.e., symmetric conservative metrics hereafter, attains the fully conservative property of conservative quantities as well as satisfying the geometric conservation law (GCL) where any linear high-order finite difference scheme can be employed.

The computation of separation control around NACA0015 airfoil with a synthetic jet (angle of attack is 12 [deg] and chord Reynolds number is 63,000) is conducted using 6th-order compact scheme.The effect of actuation frequency and position of the synthetic jet is arranged by varying the actuation frequency and position of the synthetic jet, and the control performance is surveyed in terms of aerodynamic coefficients. The controlled flow is investigated by time averaged fields, and the relation between separated regions on the suction surface and aerodynamic coefficients is discussed. The significant turbulent statistics is also extracted in terms of momentum addition in freestream direction by the mixing, and the related vortex structure is detected by phase-averaging procedure based on actuation frequency. The $u'w'$ component of Reynolds shear stress is especially focused in this thesis, and turbulent component is mainly enhanced almost all over the airfoil surface. In addition, two-dimensional vortex structure is extracted in phase and span-averaged flow fields, and the Reynolds shear stress is found to be locally enhanced between each vortex structure.

In the appendix, the newly developed geometric interpretations of symmetric conservative metrics is presented. It is based on the spatial discretization by any linear high-order finite-diffrence scheme, and the resulting geometric interpretation of metrics is strongly related to that given by classical finite-volume like interpretations. The spatial symmetry property is also investigated in terms of the robustness and resolution of the high-order finite-difference scheme, and the property is shown significant with the use of highly-skewd stationary grids.

Acknowledgement

First, I would like to express my special gratitude to Prof. Kozo Fujii, who provided me with this attractive and challenging research theme and many appropriate advices and guidance. I am also thankful for his support on my presentation in many international and domestic conferences. Second, I am deeply grateful to Prof. Taku Nonomura for his appropreate advices, constructive discussion and technical support during my whole research. I would like to thank Prof. Akira Oyama for his benefited and helpful advices particularly on my presentation. I also appreciate Dr. Nobuyuki Iizuka for his constructive and helpful comments of keen intelligence. My special thanks also go to my seniors and colleagues giving me so many helpful comments and supports.

Contents

Chapter 1

Introduction

Micro devices for a separation control recently attract a lot of attention because they achieve less energy consumption, comparatively simple structures, and more effective control on unsteady flow fields compared to conventional devices: “steady jet” and “vortex generator”. In this thesis, “synthetic jet” (hereafter, denoted as SJ) is focused. SJ is one of the most advanced micro device to control a separated flow. Figure 1.2 shows a schematic diagram of a synthetic jet. A synthetic jet consists of a cavity and an orifice connected to the cavity whose bottom oscillates with a small amplitude. The brief sequence of separation control using a synthetic jet is as follows. The periodic deformation of the cavity produces blowing and suction flow periodically from the orifice exit. First, the resulting flow from the orifice exit fluctuates the separated shear layer near the exit, and then the fluctuation is amplified as it shedding along an airfoil. Finally, the whole separated flow is modified, and the attached flow is obtained. The momentum flux directly provided from the synthetic jet is so small that piezoelectric devices, piston, and speaker are practically used to oscillate the cavity bottom[14] [4] [13] . Therefore, a synthetic jet is considered suitable for unmanned air vehicles (UAV) and microscale air vehicles (MAV) due to its simple structures and small energy consumption. Recently, some research reports the practical use of a synthetic jet (see Fig. 1.1). In addition, many experimental and numerical studies in related literature report that a synthetic jet is also applicable for separation control not only over an airfoil but for the other fluidic machineries, e.g., turbine blades.

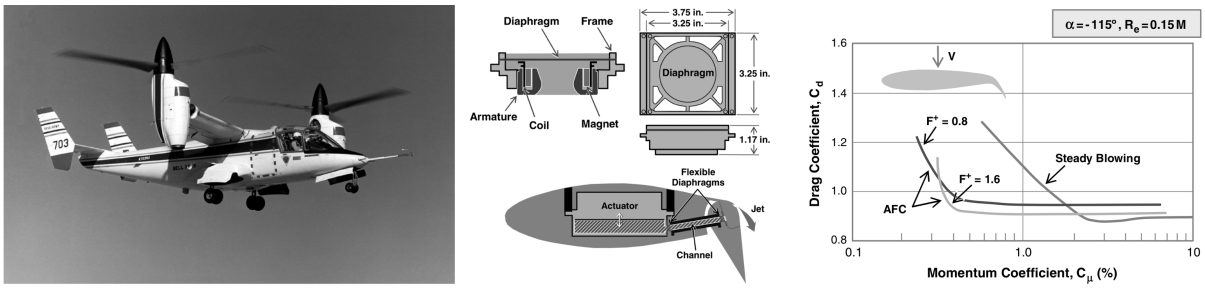

Fig. 1.1: Application of synthetic jet devices to a tiltrotor aircraft by McVeigh et al. [19].

1.1 Overview of the previous studies on separation control using the SJ

To date, a lot of experimental and numerical studies have focused on optimal control variables of a synthetic jet determined by time-averaged flow fields[4][13]. In particular, most of numerical studies adopt a Reynolds-averaged Navier-Stokes (RANS) equations to obtain time-averaged flow fields, and the aerodynamic coefficients and optimal control variables show good agreement with those obtained by experiments[17][9][14]. In these computational studies using RANS, the synthetic jet is often modeled by two-dimensional (in spanwise direction) velocity condition on an airfoil surface although the practical synthetic jet produces blowing and suction flows by oscillating the cavity bottom. Therefore, it implies that the synthetic jet can be modeled by two-dimensional velocity condition on an airfoil in terms of aerodynamic coefficients and optimal control variables determined by time-averaged flow fields adopting RANS analysis. On the other hand, it has been reported that time variant values, e.g., turbulent statistics and phase-averaged flow fields, do not correspond to those of experiments. This may because aerodynamic coefficients of time-averaged flow fields are governed by large flow structures such as large vortices shdding along an airfoil surface, and two-dimensionality is essential to them.

1.2 Numerical studies on the separation control using SJ

Recently, three-dimensional unsteady analyses are getting more and more significant with regards to the physics of the separation control focusing on turbulent structure which

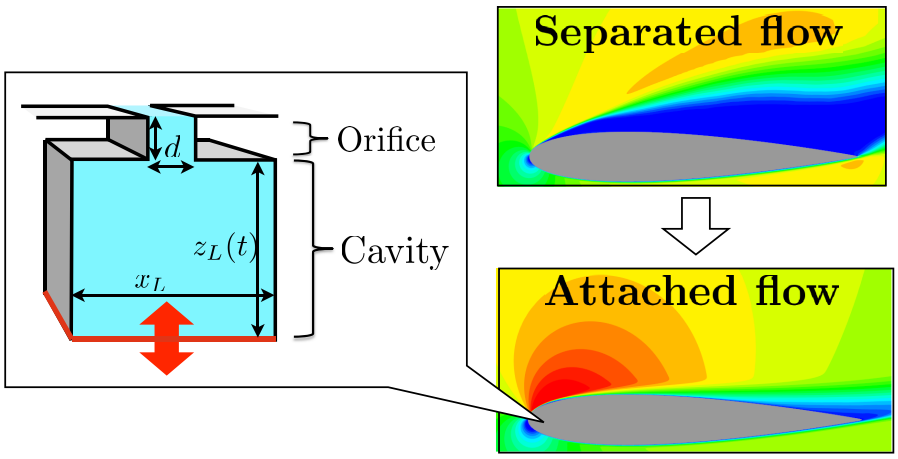

Fig. 1.2: Schematic diagram and geometric configuration of a synthetic jet.

is three-dimensional and unsteady. For example, Rizzetta and Visbal investigated a synthetic jet using a direct numerical simulation of Navier-Stokes equations (DNS) and discussed effects of the Reynolds number defined by the characteristic of the induced jet. However, the induced jet is modeled by a two-dimensional boundary condition given at the orifice exit (without cavity), therefore the effects of the three-dimensional flow structure is not strictly examined. On the other hand, Ravi et al. conducted DNS[26] on an induced jet from the three-dimensional cavity, and reported that the strong three-dimensional unsteady flows exist in the cavity. Accordingly, Okada et al. performed large-eddy simulation of Navier-Stokes equations (LES) on the separation control over a backward facing step using the synthetic jet with three-dimensional cavity[24], and the characteristics of turbulent structures in the external flow controlled by the synthetic jet is discussed. In this way, the computation of unsteady flows both in an external flow and in the deforming cavity using high-resolutional schemes is regarded important among recent studies. They also investigated three-dimensional turbulent structures from the cavity to static air by comparing the synthetic jet modeled by the Cavity and Bc model, and concluded that the turbulent structure is more enhanced with the Cavity model, therefore the Bc model should not be adopted as the model of synthetic jet.

1.3 Investigation of the mechanism for sepaaration control

For an applied flow, You and Moin conducted LES[33] for the separation control around an airfoil, and the aerodynamic coefficients well correspond to those of experimental results. They also reported that the key mechanism of separation control is not only the modification of two-dimensional boundary layer profile by adding or removing momentum in freestream direction, but also three-dimensional turbulent mixing. However, since their synthetic jet produces a jet in the downstream direction, it is difficult to clarify the effect of direct momentum addition from that of turbulent mixing with respect to the mechanism of separation control. Moreover, they have not quantitatively discussed turbulent statistics of controlled flow fields, and the effects of an actuation frequency and position of SJ on the turbulent structure has not been well investigated. In this way, the mechanism of separation control around an airfoil has not been clearly classified especially in terms of three-dimensional turbulent structure in the controlled flow field.

1.4 Outline of this thesis

In this thesis, the effect of an actuation frequency and position of SJ on the aerodynamic performance and turbulent statistics of the separation-controlled flow over NACA0015 airfoil is focused. Therefore, LES is adopted to evaluate the unsteady characteristics of turbulent structures. As refered in the previous pargraph, the flow field inside the cavity includes a turbulent structure, and it much affects the external flow and the resulting perfomance of a separation control. Thus, a high-fidelity computation is needed to simulate the flow field inside the cavity which is deforming according to the acutuation frequency. In the related literature where the flow field inside the deforming cavity is simulated [24], the body-fitted coordinate is adopted to generate computational grids, and the grid is deformed according to the actuation frequency. High-order computation of compressible flow on a moving and deforming grid generally requires special treatment to evaluate the component of a coordinate-transformation matrix (hereafter, denoted as metrics and Jacobian), otherwise a freestream is not correctly computed. The criteria of the adequate evaluation of metrics and Jacobian is known as the geometric conservation

law (GCL), which corresponds to computing the freestream correctly (hereafter, denoted as a freestream preservation). The technique to satisfy the GCL identities with using high-order finite-difference scheme has been proposed to rewrite the governing equation from its strong conservative form to nonconservative form in terms of Jacobian [31][24]. However, this technique adopts the nonconservative form of the governing equation, and so the conservation property of conservative quantities is not strictly ensured. The conservation property is, for example, important to compute a shock speed or evaluate a net mass flux correctly through the finite volume on moving and deforming grid. One of the significant property of the synthetic jet is zero-net property of a mass flux from a cavity to the external flow. Considering this property, the scheme which adopts a strong conservative form of the governing equation and employs high-order finite differencing for the spatial discretization is appropriate to the present computation.

Chapter 2

Problem settings

2.1 Flow condition

In this section, the flow condition and configurations of SJ are presented. Note that in the following section, the asterisk denotes the dimensional value; the terms "leading edge" and "trailing edge" are frequently used, which indicate the location of 0% and 100% of the airfoil chord. The flow is around the NACA0015 airfoil, and the angle of attack is set to 12 [deg]. The freestream Mach number is set to 0.2 as the compressibility of the fluid is almost negligible except near the leading edge. The Reynolds number, defined by the chord length c_h^* and freestream velocity u_∞^*, is set to $63,000$. The flow is completely separated from 2.5% of the airfoil chord without control. The fluid is assumed to be air, and the specific heat ratio and the Prandtl number are set to 1.4 and 0.72, respectively.

2.2 Configuration of the synthetic jet

The synthetic jet is installed at the leading edge ($x/c_h = 0.0$) of the airfoil, and its orifice is normal to the airfoil surface. In this study, we adopt the leading edge as the position of the synthetic jet, which has been reported effective for a wide variety of airfoils [4][14]. In the following, all nondimensional values are based on the freestream velocity, u_∞^*, the wing chord length c_h^*, and the freestream density ρ_∞^*; they are denoted without a superscript "$*$", e.g., pressure p, density ρ, and velocity vector $\boldsymbol{u} = (u, v, w)$. The nondimesional value of actuation frequency f^* is denoted by F^+ according to the

previous studies [14][24][23] which is defined as $F^+ \equiv f^* c_h^* / u_\infty^*$. Note that $c_h \equiv 1$ and $u_\infty \equiv 1$ hold according to the definition above but c_h and u_∞ are often explicitly written for ease of understanding below. For simplicity, two-dimensional shapes along the span are adopted for the orifice and cavity, as shown in Fig.2.1. The orifice width is set to 0.5% of the chord length ($d = 0.005 c_h$), which is often used in previous studies[25] [33]; the orifice height is set to d; the cavity depth is set as $z_{L0} = 10d$; and the cavity bottom width is set as $x_L = 5.5d$. The shapes of the cavity and orifice are similar to those used in a previous study[25]. The bottom of the cavity oscillates in a translational motion

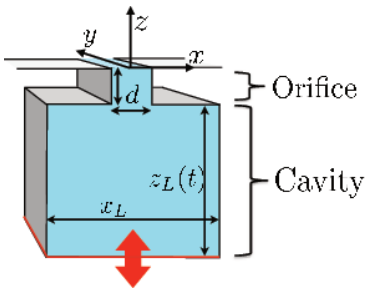

Fig. 2.1: Geometric configuration of synthetic jet

according to Eq.(2.1).The amplitude of oscillation is denoted by A, time is denoted by t, and the depth of cavity is denoted by $z_L(t)$ as follows:

$$z_L(t) = z_{L0} + A\cos(2\pi F^+ t), \qquad F^+ = \frac{f^* c_h^*}{u_\infty^*}. \tag{2.1}$$

The momentum coefficient C_μ is defined by Eq.(2.2), which is the ratio of the momentum induced by the synthetic jet and the freestream. Here, the fluid in the cavity is assumed to be incompressible, and the momentum induced by the synthetic jet $\rho u_{\max}$ is determined according to the cavity depth, $z_L(t)$.

$$C_\mu \equiv \frac{\rho u_{\max}^2 d}{\rho u_\infty^2 c_h}, \qquad u_{\max} d \equiv x_L \max\left(\frac{dz_L(t)}{dt}\right) = 2\pi x_L A F^+. \tag{2.2}$$

Note that the amplitude A is changed according to F^+ when C_μ is kept constant as $A = u_\infty \sqrt{c_h C_\mu d}/(2\pi F^+ x_L)$.

2.3 Boundary condition models

Chapter 3

Numerical methods

3.1 Flow solver

In this study, LANS3D[10], a fluid analysis solver developed at the ISAS/JAXA, is employed for the series of computations. The governing equations are three-dimensional compressible Navier-Stokes equations. These equations are solved in the body fitted coordinates (ξ, η, ζ). As the fluid structure in the cavity and orifice is very small and unsteady, a high-resolution unsteady computational method is required. Thus, the spatial derivatives of convective terms and viscous terms, metrics, and the Jacobian are evaluated by a six-order compact difference scheme[18]. Near the boundary, second-order explicit difference schemes are used. Tenth-order filtering[30] [12] is used with a filtering coefficient of 0.495. For time integration, lower-upper symmetric alternating direction implicit and symmetric Gauss-Seidel(ADI-SGS)[21] methods are used. To ensure time accuracy, a backward second-order difference formula is used for time integration, and five sub-iterations[32] are adopted. The computational time step is 2×10^{-4} in nondimensional time to obtain a maximum Courant-Friedrichs-Levy (CFL) number of approximately 1.8. Using these methods, implicit LES approach (ILES[32]) is adopted. In the ILES approach, no additional stress and heat flux is appended as the sub-grid-scale (SGS) models. Instead, a high-order, low-pass filter selectively damps only poorly resolved high-frequency waves in this study. At the outflow boundary, all variables are extrapolated from one point in front of the outflow boundary (pressure is fixed to that of the freestream). For the surface of airfoil, cavity, and orifice, no-slip conditions are

adopted. A periodic boundary condition is applied to the boundaries in the spanwise direction. Note that on the deforming grid (ZONE4), the geometric conservation law (the GCL identity) is satisfied with using symmetric conservative metrics proposed by Abe et al.[1].

$$Q^*_{t^*} = -E^*_{x^*} - F^*_{y^*} - G^*_{z^*}, \tag{3.1}$$

$$Q^* = \begin{bmatrix} \rho^* \\ \rho^* u^* \\ \rho^* v^* \\ \rho^* w^* \\ e^* \end{bmatrix}, E^* = \begin{bmatrix} \rho^* u^* \\ \rho^* u^* u^* + p \\ \rho^* v^* u^* \\ \rho^* w^* u^* \\ (e^* + p^*) u^* \end{bmatrix}, \quad F^* = \begin{bmatrix} \rho^* v^* \\ \rho^* u^* v^* \\ \rho^* v^* v^* + p \\ \rho^* w^* v^* \\ (e^* + p^*) v^* \end{bmatrix}, G^* = \begin{bmatrix} \rho^* w^* \\ \rho^* u^* w^* \\ \rho^* v^* w^* \\ \rho^* w^* w^* + p \\ (e^* + p^*) w^* \end{bmatrix},$$

$$e^* = \frac{p^*}{\gamma - 1} + \frac{1}{2}\rho^*(u^{*2} + v^{*2} + w^{*2}) \tag{3.2}$$

$$p^* = (\gamma - 1)\left(e^* - \frac{1}{2}\rho^*(u^{*2} + v^{*2} + w^{*2})\right), \quad a^* = \sqrt{\frac{\gamma p^*}{\rho^*}}, \quad M = \frac{1}{a}\sqrt{u^{*2} + v^{*2} + w^{*2}} \tag{3.3}$$

$$\rho = \frac{\rho^*}{\rho^*_\infty}, \quad u = \frac{u^*}{a^*_\infty}, \quad v = \frac{v^*}{a^*_\infty}, \quad w = \frac{w^*}{a^*_\infty}, \quad a = \frac{a^*}{a^*_\infty}, \quad p = \frac{p^*}{p^*_\infty \gamma}, \quad e = \frac{e^*}{e^*_\infty}\left(\frac{1}{\gamma(\gamma-1)} + \frac{1}{2}M^2_\infty\right) \tag{3.4}$$

$$\rho = q_1, \quad u = \frac{q_2}{q_1}, \quad v = \frac{q_3}{q_1}, \quad w = \frac{q_4}{q_1}, \tag{3.5}$$

$$p = (\gamma - 1)(e - \frac{1}{2}\rho(u^2 + v^2 + w^2)), \quad a = \sqrt{\frac{\gamma p}{\rho}}, \quad M = \frac{1}{a}\sqrt{u^{*2} + v^{*2} + w^{*2}} \tag{3.6}$$

$$a^*_\infty = \sqrt{\frac{\gamma p^*_\infty}{\rho^*_\infty}}, \quad e^*_\infty = \frac{p^*_\infty}{\gamma - 1} + \frac{1}{2}\rho^*_\infty (a^*_\infty M_\infty)^2 \tag{3.7}$$

$$\rho_\infty = 1, \quad a_\infty = 1, \quad \sqrt{u^2_\infty + v^2_\infty + w^2_\infty} = M_\infty, \quad p_\infty = \frac{1}{\gamma}, \quad e_\infty = \frac{1}{\gamma(\gamma-1)} + \frac{1}{2}M^2_\infty, \tag{3.8}$$

$$(\rho^* u^*)_{t^*} = -(\rho^* u^* u^* + p^*)_{x^*} - (\rho^* u^* v^*)_{y^*} - (\rho^* u^* w^*)_{z^*} \tag{3.9}$$

$$\iff \frac{1}{a^*_\infty}(\rho u)_{t^*} = -(\rho u u + p)_{x^*} - (\rho u v)_{y^*} - (\rho u w)_{z^*} \tag{3.10}$$

$$(e^*)_{t^*} = -((e^* + p^*)u^*)_{x^*} - ((e^* + p^*)v^*)_{y^*} - ((e^* + p^*)w^*)_{z^*} \tag{3.11}$$

$$\iff \frac{1}{a^*_\infty}(e)_{t^*} = -((e + p)u)_{x^*} - ((e + p)v)_{y^*} - ((e + p)w)_{z^*} \tag{3.12}$$

$$Q_t = -E_x - F_y - G_z, \tag{3.13}$$

$$Q = \begin{bmatrix} \rho \\ \rho u \\ \rho v \\ \rho w \\ e \end{bmatrix}, \quad E = \begin{bmatrix} \rho \\ \rho u \\ \rho v \\ \rho w \\ e + p \end{bmatrix}, F = \begin{bmatrix} \rho \\ \rho u \\ \rho v \\ \rho w \\ e + p \end{bmatrix}, G = \begin{bmatrix} \rho \\ \rho u \\ \rho v \\ \rho w \\ e + p \end{bmatrix},$$

$$e = \frac{p}{\gamma - 1} + \frac{1}{2}\rho(u^2 + v^2 + w^2) \tag{3.14}$$

3.2 Computational grids

A zonal grid approach[11] is employed: background grid around airfoil (ZONE1), cavity of the synthetic jet (ZONE4), orifice of the synthetic jet (ZONE3), and intermediate region (ZONE4) are generated separately as shown in Fig. 3.1. Every five or ten points in each direction are shown in this figure. On the boundaries of zonal grid connected with each other, around 20 grid points are overlapped and the flow variables are exchanged with small errors[11]. The total number of grid points is approximately 30 million (Table **??**).

3.2.1 Background grid

The C-type grid is adopted around an airfoil, and the outer boundary is located at $25c_h$ away from the leading edge. The length of the computational region in the span direction (y direction) is $0.2c_h$, and a periodic boundary condition is applied to the spanwise boundaries. The boundary-fitted coordinate system (ξ, η, ζ) is employed for the computation; the minimum grid size in the direction normal to the airfoil surface (ζ

direction) is 0.12% of the chord length c_h. Note that the attached flow (angle of attack is 9 [deg]) is computed for ZONE1 grid, and the grid size in each direction is obtained as $(\Delta\xi^+, \Delta\eta^+, \Delta\zeta^+) \leq (8, 9, 1)$ with using wall units. These values satisfy the criteria of grid spacing to resolve a near-wall turbulence proposed by Kawai et al.[16].

3.2.2 Grids around the synthetic jet

All grids (ZONE1 to ZONE4) are employed for the computation. The minimum grid size of orifice and cavity grid (ZONE3 and ZONE4) correspond to that of background grid (ZONE1). The grid system for the cavity region (ZONE4) deforms[20] according to the oscillation of the cavity bottom.

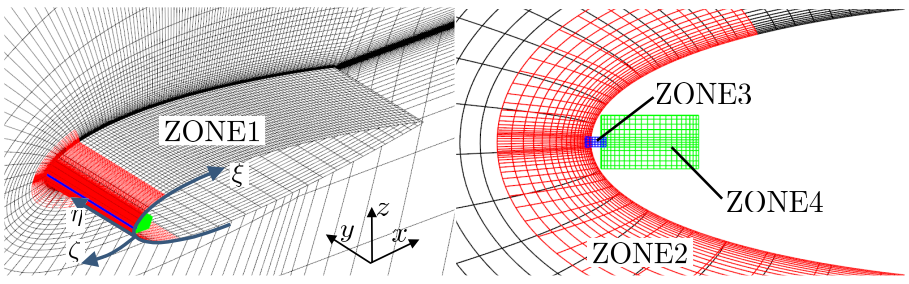

Fig. 3.1: Computational grids

3.3 Tools for analysis

3.3.1 Averaging procedure

3.3.2 Fourier analysis

3.3.3 Linear stability analysis

3.4 Verification and validation of the flow solver

3.4.1 Convergence study of the grid spacing

First, we conducted a series of verification tests for the separated flow around the NACA0015 airfoil, where the angle of attack is 12 [deg]. Three types of computational grids were prepared for verification: coarse, medium and fine grids, in which the number of grid points is 9 million, 19 million, and 44 million, respectively. The medium grid corresponds to the grid presently used in this paper. Table 3.1 shows the aerodynamic coefficients (C_L, C_D, and C_L/C_D); both C_L and C_D slightly increase with the grid density. On the other hand, the suction peak at the leading edge and the plateau pressure distribution are similarly observed for all grids, as shown in Fig. 3.2. In addition, for the separation controlled flow with $F^+ = 6.0$, the grid sizes in the wall unit were obtained as $(\Delta\xi^+, \Delta\eta^+, \Delta\zeta^+) \leq (10, 9, 1)$ in the attached-flow region over the airfoil (see Fig. 3.3). These values satisfy the criteria of grid spacing to resolve a near-wall turbulence proposed by Kawai and Fujii [16] and Teramoto [29] . Therefore, the grid density of the medium grid is sufficient for discussion on the separation control effects in this paper. Note that the aerodynamic coefficients of the noncontrolled case have been validated by comparing with those of the experiments [22] . In addition, the Mach number effect for the computation with and without control has been verified using the same grid and scheme although a dielectric barrier discharge (DBD) plasma actuator is employed [6] .

Second, the controlled flow with $C_\mu = 2.0 \times 10^{-3}$ of $F^+ = 6.0$ is computed using the medium and fine grids.

Table 3.1: Aerodynamic coefficients

Grid density	C_L	C_D	C_L/C_D
Coarse	0.410	0.143	2.85
Medium	0.458	0.157	2.92
Fine	0.477	0.159	2.99

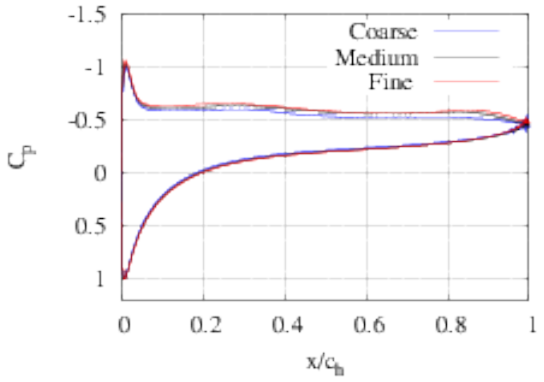

Fig. 3.2: C_p distribution of time-averaged flow fields on fine, medium, and coarse grids.

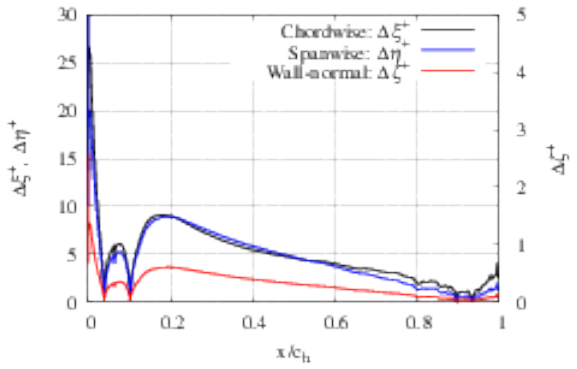

Fig. 3.3: Grid sizes in the wall units near the wing surface are shown for the controlled case ($F^+ = 6.0$).

3.4.2 Verification of the time step size

Here, the separated flow around the NACA0015 airfoil with the angle of attack 12 [deg] is computed using the medium grid. The computational time-step size in the wall unit was obtained as $\Delta t^+ \leq 0.1$ in Fig 3.4, which is sufficiently smaller than that proposed by Choi [8] for turbulent flow.

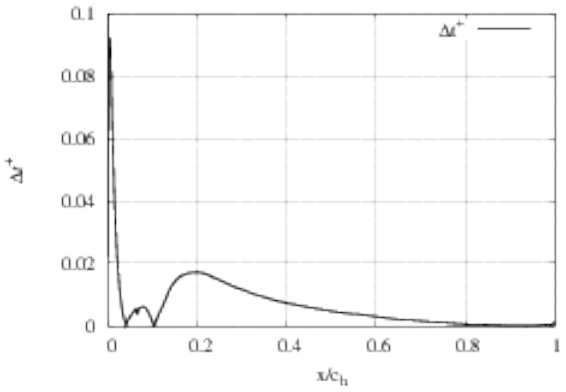

Fig. 3.4: Time-step size in the wall unit is shown for the controlled case ($F^+ = 6.0$).

3.4.3 Verification of the spanwise length for the computation

3.4.4 Validation of the flow solver

3.5 Verification of the LST tools

Chapter 4

Effects of the actuation frequency on the separation control using a synthetic jet

4.1 Outline

For example, Okada et al. performed a large-eddy simulation (LES) on the separation control over a backward facing step using a synthetic jet with a three-dimensional cavity[24]. The characteristics of turbulent structures in external flow controlled by the synthetic jet were also discussed. You and Moin also conducted LES[33] on the separation control around an airfoil; the aerodynamic coefficients from the simulation corresponded well to those obtained experimentally. They also reported that the key mechanisms of separation control include not only the modification of two-dimensional boundary layer profile by adding or removing momentum in the freestream direction, but also three-dimensional turbulent mixing. However, they did not examine control effects on actuation frequency, and a quantitative discussion has never been conducted in terms of the relationship between turbulent mixing and separation control over an airfoil.

4.2 Case description

The following computational cases are discussed in this chapter: the SJ is installed at the leading edge of the airfoil, and the momentum coefficient is set to $C_\mu = 2.0 \times 10^{-3}$ and 2.0×10^{-5}; the actuation frequency is set to $F^+ = 1.0, 6.0, 10, 15, 20$, and 30.

The momentum coefficient C_μ show the strength of induced jet from the SJ, which is set to relaatively smaller value than the previous studies, e.g., $C_\mu = 3.5 \times 10^{-3}$ by Amitay and Glezer[4], $C_\mu = 1.23 \times 10^{-3}$ by You and Moin[33], $C_\mu = 2.13 \times 10^{-4}$ by Zhang et al.[34], and $C_\mu = 2.00 \times 10^{-3}$ by Okada et al.[**?**][**?**] The present study adopt the smaller C_μ so that the contributions of direct momentum addition and development of disturbances from SJ would be effectively clarified in the separation control mechanism (see Sec. **??**). Note that the definitions of the momentum coefficient C_μ is not strictly

Table 4.1: Computational cases. The synthetic jet is installed at the leading edge of the airfoil.

case name	input momentum (C_μ)	F^+
Off control	—	—
strong input	2.0×10^{-3}	1.0, 6.0, 10, 15, 20, 30
weak input	2.0×10^{-5}	1.0, 6.0, 10, 15, 20, 30

the same among the studies above. Here again, the definition of C_μ is presented:

$$C_\mu \equiv \frac{\rho u_{\max}^2 d}{\rho u_\infty^2 c_h}, \tag{4.1}$$

which has been introduced in Eq.(**??**). The present study, You and Moin[33], and Okada et al.[**?**] adopt the definition of $u_{\max}$ as

$$u_{\max} d \equiv x_L \max\left(\frac{dz_L(t)}{dt}\right) = 2\pi x_L A F^+, \tag{4.2}$$

where the jet is assumed to be incompressible fluid and have the spatially uniform profile on the orifice exit plane. On the other hand, the definition of $u_{\max}$ by Amitay and Glezer[4] is

$$u_{\max} d \equiv \frac{2d}{T_{\text{peri}}} \int_0^{T_{\text{peri}}/2} \langle u_{\text{jet}}(\phi, 0, 0)^2 \rangle_\phi d\phi, \tag{4.3}$$

where $\langle\bullet\rangle_\phi$ indicates the phase average based on the actuation frequency F^+; $T_{\rm peri} = 1/F^+$. The jet velocity $u_{\rm jet}(\phi, x_{\rm jet}, z_{\rm jet})$ is assumed to be a point value at the center of the orifice exit plane $(x_{\rm jet}, z_{\rm jet}) = (0, 0)$ although in their paper, the location is not specifically denoted except for the "jet exit plane". The definition of $u_{\rm max}$ by Zhang et al.[34] is, whereas,

$$u_{\rm max} d \equiv \frac{2d}{T_{\rm peri}} \int_{-d/2}^{d/2} \int_0^{T_{\rm peri}/2} \langle u_{\rm jet}(\phi, x_{\rm jet}, 0)^2 \rangle_\phi d\phi dx_{\rm jet}. \tag{4.4}$$

The velocity profile of $u_{\rm jet}$ in their study is assumed to be Poiseuille-type one: $0.2u_\infty[1 - (x_{\rm jet}/d)^2]\sin(2\pi F^+ t)$ with spanwise-uniform profile on the orifice exit plane. The following table summarizes the C_μ values of the present study in the different definitions above. The results do not show remarkable differences up to $\pm$%, which would be acceptable for the discussion in this study because the main focus of this study lies on the actuation frequency F^+.

Table 4.2: C_μ of the present study in different definitions ($F^+ = 6.0$)

C_μ of Eq.(4.2) (present study, You and Moin[33], Okada et al.[**?**])	C_μ of Eq.(4.3) (Amitay and Glezer[4])	C_μ of Eq.(4.4) (Zhang et al.[34])
2.0×10^{-3}	2.1×10^{-3}	1.8×10^{-3}
2.0×10^{-5}	2.1×10^{-5}	1.8×10^{-5}

The actuation frequency F^+ covers equally to or higher values compared with the previous studies [4][33][**?**][34] including the optimum ones $F^+ \simeq 1$[4][34] and $F^+ \simeq 10$[4]. The other criteria for the present range of F^+ comes from the previous studies for airfoil-flow separation control using DBDPA[7][22][27], which shows the effective F^+ to be approximately 6 to 10. The results using SJ will be compared with those using DBDPA in Chap.**??**. Note that the different definition of F^+ has been also proposed in the previous studies [**?**], where the reference length is taken to be the lengh of a separation bubble near the leading edge:$F^+_{\rm sep} \equiv f^{*+}/L_{\rm sep}$. Let $L_{\rm sep}$ be the separation length defined in Sec.**??** (Fig.**??**), then the following values are obtained as the $F^+_{\rm sep}$ for the case with $C_\mu = 2.0 \times 10^{-5}$.

Table 4.3: F^+ of the present study in different definitions ($C_\mu = 2.0 \times 10^{-3}$)

F^+ of Eq.(4.2) (present study, You and Moin[33], Okada et al.[**?**])	$F^+_{\rm sep}$ of Eq.(4.3) (Amitay and Glezer[4])
1.0	1.8×10^{-3}
6.0	1.8×10^{-5}

4.3 Capabilities of the SJ in separation control based on aerodynamic coefficients

In this section, the capabillities of the SJ are arranged in terms of its time-averaged aerodynamic coefficients. Figure 4.1 shows the time history of the aerodynamic coefficients C_L and C_D, which fluctuats based on the actuation frequency F^+. The C_L and C_D show significant increase and reduction from the baseline case (absence of the control), respectively, which indicate the stall recovery for each controlled cases in Fig.4.1. Note that again, the period $20 \leq t/u_\infty c_h \leq 28$ is regarded as the quasi-steady state and taken for the time averaging procedure as explained in Sec.**??**.

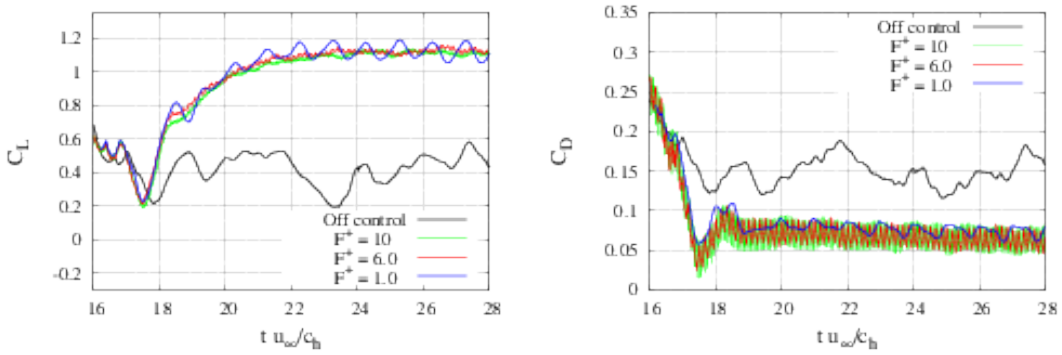

(a) C_L (b) C_D

Fig. 4.1: Time history of the aerodynamic coefficients in the cases with $C_\mu = 2 \times 10^{-3}$: (a) lift coefficient C_L; (b) drag coefficient C_D.

4.3.1 Time-averaged aerodynamic performances

The definitions of C_L and C_D are as follows:

$$C_L = \frac{\text{Lift}}{\frac{1}{2}\rho_\infty u_\infty^2 c_h y_{\text{span}}}, \quad C_D = \frac{\text{Drag}}{\frac{1}{2}\rho_\infty u_\infty^2 c_h y_{\text{span}}}, \tag{4.5}$$

where y_{span} indicates the spanwise length (y_{span} is set to $0.2/c_h$ in the present study). C_{Dp} and C_{Dv} indicates the contribution of the drag from pressure and skin friction.

Table 6.2 and Fig. 4.2 show time-averaged aerodynamic coefficients. In Table 6.2, the values of lift coefficient C_L, drag coefficient C_D, lift-drag ratio C_L/C_D, pressure

drag C_{Dp}, frictional drag C_{Df}, and standard deviation of C_L and C_D. The Δ indicates the improvement ratio from the baseline case, e.g., $\Delta C_L \equiv C_{L;\text{controlled}}/C_{L;\text{control off}}$, and $\Delta C_D \equiv C_{D;\text{control off}}/C_{D;\text{controlled}}$. In Fig.4.2, the effect of F^+ on C_L and C_D is shown, where blue line shows the strong input $C_\mu = 2.0 \times 10^{-3}$, and red line shows the weak input $C_\mu = 2.0 \times 10^{-5}$ cases, respectively. The fluctuation of C_L and C_D in time direction is also shown by error bars in Fig.4.2(a) and (b), where the length of each error bars is 75 times larger than actual fluctuation for ease of visualization. In Fig.4.2, the absolute value of fluctuation can be compared with each other cases although its length do not show the accurate value.

Table 4.4: Time averaged aerodynamic coefficients

C_μ	F^+	C_L	C_D	C_L/C_D	C_{Dp}	C_{Dv}	σ_{C_L}	σ_{C_D}
Control off	—	1.10	0.0775	14.2				
2.0×10^{-3}	1.0	1.10	0.0775	14.2				
	6.0	1.10	0.0775	14.2				
	10	1.10	0.0775	14.2				
	15	1.10	0.0775	14.2				
	20	1.10	0.0775	14.2				
	30	1.10	0.0775	14.2				
2.0×10^{-5}	1.0	1.10	0.0775	14.2				
	6.0	1.10	0.0775	14.2				
	10	1.10	0.0775	14.2				
	15	1.10	0.0775	14.2				
	20	1.10	0.0775	14.2				
	30	1.10	0.0775	14.2				

In the cases with a strong input ($C_\mu = 2.0 \times 10^{-3}$), all the actuation frequencies attain stall recovery for $\Delta C_L/C_D \simeq 200\%$. Figure 4.2(a) shows the C_L variation for F^+. The strong input case (blue line: $C_\mu = 2.0 \times 10^{-3}$) shows the most improved C_L at $F^+ = 1.0$. However, the lift-drag ratio of the case with $F^+ = 1.0$ shows the less recovery than the other F^+. This is mainly caused by the less improvement of C_D, which is dominated by the pressure drag C_{Dp}. This implies that the drag reduction would be more effective

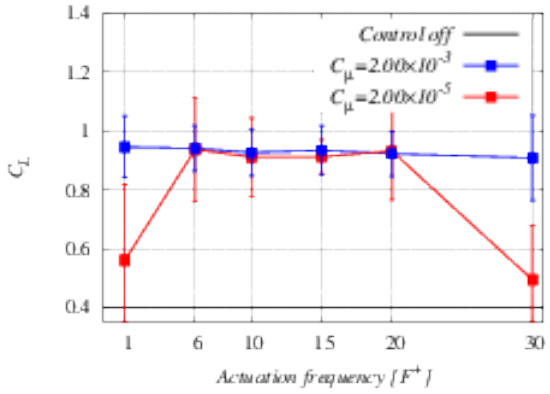

(a) C_L

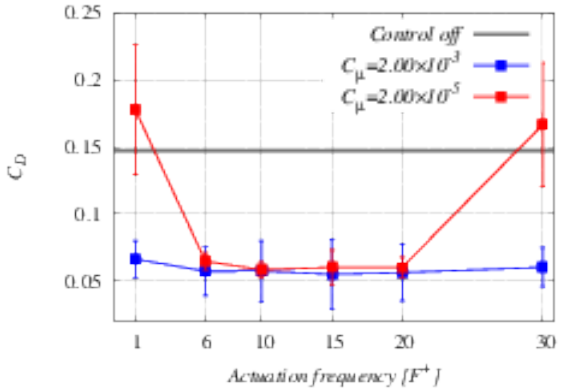

(b) C_D

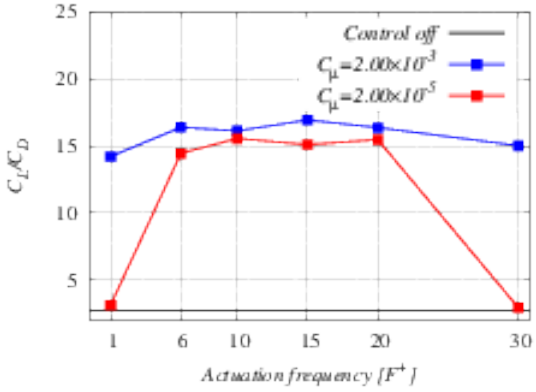

(c) C_L/C_D

Fig. 4.2: Time-averaged aerodynamic coefficients are shown; the fluctuation of C_L and C_D in time direction is shown by error bars, where the length of each error bars is 75 times larger than actual fluctuation for ease of visualization.

for the improvement of the lift-drag ratio in the present conditions for the baseline flow ($Re = 63,000$, NACA0015, $AoA = 12$[deg]) and the actuator position. The superiority of $6 \leq F^+ \leq 20$ to $F^+ = 1.0, 30$ is more clearly observed in weak input cases in Fig.4.2 (red lines: $C_\mu = 2.0 \times 10^{-5}$), where only the cases with $6.0 \leq F^+ \leq 20$ can achive the stall recovery ($\Delta C_L/C_D \simeq$??%). Therefore, in the present baseline flow/acturator conditions, the effect of the actuation frequency on the SJ capability is summarized as follows: the optimum frequency for the separation control is localized within $6.0 \leq F^+ \leq 20$ regime. In this thesis, hereinafter, the capability of the SJ is evaluated by the time-averaged lift-drag ratio. Note that the fluctuation in temporal direction is also smaller in $6.0 \leq F^+ \leq 20$ than $F^+ = 1.0$ as shown in $\sigma_{C_L}, \sigma_{C_D}$ in Table.6.2. The fluctuation of the aerodynamic coefficients will be discussed in Sec.**??** in detail.

However, the significance of the drag reduction and lift increase which has been mentioned in this section can largely rely on the flow/actuator conditions. For example, recent study on separation control over an airfoil using the SJ by Zhang et al.[34] reported that $F^+ = 1.0$ attains better lift-drag ratio than $F^+ = 4.0$ although the drag reduction is better achived by the case with $F^+ = 4.0$. This indicates that in their conditions, the lift increase using $F^+ = 1.0$ would be more effective for the recovery of the lift-drag ratio. The inconsistency with the present result can be explained by the smoothness and quickness of a turbulent transition using a high-frequency mode ($F^+ > 1$). As will be explained in Sec.**??**, one of the key mechanisms for the separation control is turbulent structures over an airfoil, which can effectively exchange the chordwise momentum near the airfoil surface. The chord-Reynolds number of their study is $10,000$, and the SJ is modelled by the two-dimensional (spanwise-uniform) velocity profile on the airfoil surface. These two factors can contribute to the enhancement of spanwise coherent structures on the controlled flows because the Reynolds number of $O(10^4)$ is in a very sensitive regime for a turbulent transition, where $Re = 63,000$ (present study) and $Re = 10,000$ (Zhang et al.[34]) would result in significantly different turbulent structures[**?**]; and the three-dimensional vortex structure can be generated inside the cavity of the SJ, which is omitted in their study but would affect the turbulent transition on the airfoil surface.

4.3.2 Basic features of controlled flows on time-averaged C_p and C_f

The pressure coefficient C_p and skin friction C_f are similarly defined as functions of (x, z) (coordintes in the chordwise and vertical direction), where the spatial averaging procedure is conducted in the spanwise (y) direction.

$$C_p = \frac{p_{\text{airfoil surface}}}{\frac{1}{2}\rho_\infty u_\infty^2}, \quad C_f = \frac{\partial U/\partial \xi_{\text{airfoil surface}}}{\frac{1}{2}\rho_\infty u_\infty^2}, \tag{4.6}$$

Fig.4.3 shows the pressure coefficient C_p on the airfoil surface in the case with $F^+ = 1.0, 6.0$ and 10 of $C_\mu = 2.0 \times 10^{-3}$ (Fig.4.3(a)) and 2.0×10^{-5} (Fig.4.3(b)), where black lines show the case without control (baseline case); blue, red, and green lines show $F^+ = 1.0, 6.0$ and 10 cases, respectively. The other results with $F^+ \geq 15$ will be summarized in Appendix.**??**. In this paragraph, the cases with $F^+ = 1.0, 6.0$ and 10 are discussed because the effect of F^+ on the SJ capability can be sufficiently explaned by the characteristics of these three frequiencies.

First, the strong input case ($C_\mu = 2.0 \times 10^{-3}$; Fig.4.3(a) and (c)) shows that in the controlled cases, the suction peak near the leading edge is much higher than that of the baseline case (black solid line), and the pressure recovery ($C_p = 0.0$) is observed at the trailing edge of the airfoil surface. This indicates that the separation is almost supressed to the atached flow by the actuation with $F^+ = 1.0, 6.0$, and 10. The pressure recovery near the leading edge shows inflection point at $x/c_h \simeq 0.05$ in all the controlled cases, where almost plateau region appears for $0.05 \leq x/c_h \leq 0.1$ in the $F^+ = 1.0$ case. Such a pressure plateau region is frequently observed in a separation bubble, which will be discussed in the next section in detail. The difference between $F^+ = 1.0$ and $F^+ > 1.0$ cases is clear in this C_p distribution, where 1) the larger pressure plateau region in $F^+ = 1.0$ than $F^+ > 1.0$ case and 2) the stronger suction peak in $F^+ > 1.0$ than $F^+ = 1.0$ case are observed in Fig.4.3. The former property, i.e., 1) larger pressure plateau region in the $F^+ = 1.0$ case, contributes to the better lift enhancement as shown in Table6.2 and Fig.4.2(a). This is because in the $F^+ = 1.0$ case, the larger pressure plateau region delays a pressure recovery at $x/c_h \simeq 0.1$, which results in the larger low-pressure region on the airfoil surface; and the wall-normal direction at $x/c_h \simeq 0.1$ is almost vertical in the present flow condition (NACA0015 airfoil and $AoA = 12$[deg]). On the other hand,

the latter property, i.e., 2) the stronger suction peak in $F^+ > 1.0$, contribute to the drag reduction as discussed in the previous part (Table6.2 and Fig.4.2(b)). The reason is that the wall-normal direction at the leading edge corresponds to the chordwise direction (almost horizontal in the present flow conditions), thus the suction at the leading edge mainly enhances the thrust. In the present flow condition, the capability (time-averaged lift-drag ratio) of the SJ is determined by the drag reduction (Table6.2 and Fig.4.2(c)): $F^+ > 1.0$ cases show better capability than the $F^+ = 1.0$ case. Therefore, it suggests that the smaller separation bubble could provide the better capability of separation control. However, as discussed in this paragraph, the lift enhancement and drag reduction show trade off based on the size of a separation bubble generated near the leading edge. Such a property of trade off would be the reason why in a different flow condition, another trend is observed in terms of the F^+ effect for the SJ capability as shown in the previous paragraph [34].

Second, the weak input case ($C_\mu = 2.0 \times 10^{-5}$) is described in Fig.4.3(b) and (d). In this case, the $F^+ = 1.0$ case (blue solid line) cannot suppress the separation, where the C_p distribution shows almost the same result with the baseline case (black solid line). On the other hand, the case with $F^+ > 1.0$ clearly shows the strong suction peak at the leading edge and pressure plateau region at $x/c_h \simeq 0.1$, which indicates the attached flow with the small separation bubble near the leading edge. Compared with the strong input case (Fig.4.3(a) and (c)), the difference between $F^+ = 6.0$ and $F^+ = 10$ cases is more clearly observed: the suction peak at the leading edge is stronger in $F^+ = 10$ case than $F^+ = 6.0$ case due to the smaller separation bubble. This would contribute to the drag reduction but lift reduction in $F^+ = 10$, which results in the better capability as discussed in Fig.4.2 for the weak input case. Note that the comparison between $F^+ = 6.0$ and 10 cases for the strong input shows that the better capability is attained in the $F^+ = 6.0$ case although the suction peak is slightly stronger and the size of separation bubble is smaller in $F^+ = 10$ than $F^+ = 6.0$. This is explained by the contribution of a lift enhancement due to larger separation bubble in $F^+ = 6.0$. In this way, the discussion on the capabilities of SJ in the present flow condition should be carefully conducted considering the trade-off relationship between the drag reduction and lift enhancement based on the separation bubble size.

Fig.4.4 shows the skin friction C_f on the airfoil surface. The C_f value is often adopted

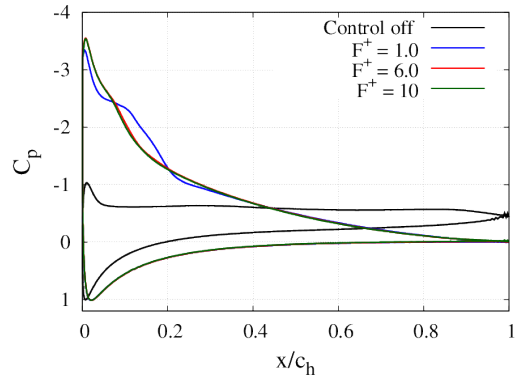

(a) $C_\mu = 2.0 \times 10^{-3}$

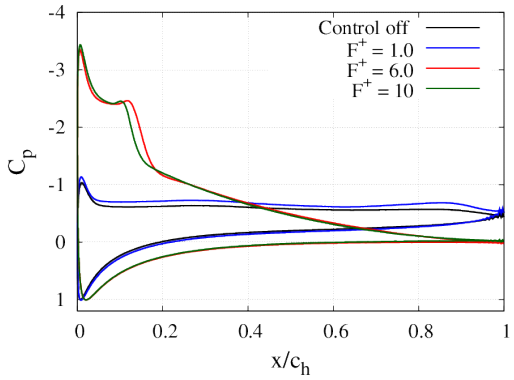

(b) $C_\mu = 2.0 \times 10^{-5}$

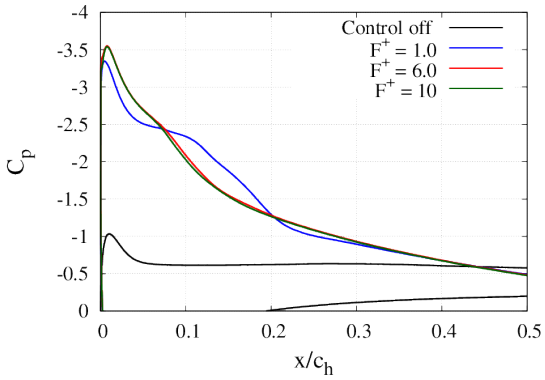

(c) $C_\mu = 2.0 \times 10^{-3}$

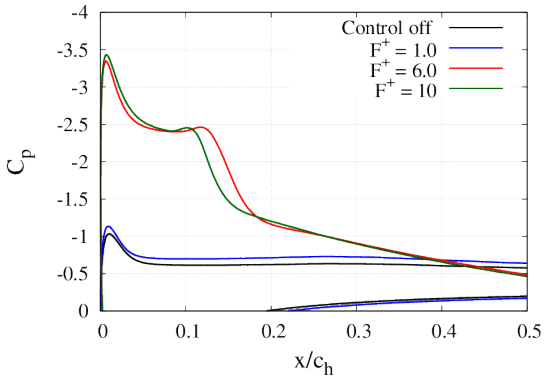

(d) $C_\mu = 2.0 \times 10^{-5}$

Fig. 4.3: Pressure coefficient C_p on the airfoil surface: (a)$C_\mu = 2.0 \times 10^{-3}$ and (b)$C_\mu = 2.0 \times 10^{-5}$.

for the criteria of attached/separated flow on the airfoil surface since the negative value of C_f indicates the reversed flow near the airfoil surface. The attached/separated region is visualized in Fig.4.5 based on this criteria, where horizontal axis shows the chordwise coordinate (x/c_h) and vertical axis shows the actuation frequency F^+; red and blue colored region correspond to the attached and separated region, respectively. The strong input cases ($C_\mu = 2.0 \times 10^{-3}$; Fig.4.4(a) and Fig.4.5(a)) show the attached flow almost all the airfoil surface with $F^+ = 1.0, 6.0$, and 10. The flow is reattached at $x/c_h \simeq 0.2$ with $F^+ = 1.0$ case, and $x/c_h \simeq 0.1$ with $F^+ = 6.0$ and 10 cases. This indicates that the separation bubble size is smaller in $F^+ = 1.0$ than $F^+ > 1.0$ cases as is discussed in Fig.4.3 for the C_p distribution. The other interesting feature is that near the trailing edge in Fig.4.5(a), the flow is attached more downstream in the $F^+ = 1.0$ case than $F^+ > 1.0$ cases. This indicates that the larger separation bubble would result in the larger attached region on the airfoil surface. The attached flow near the trailing edge contribute to the lift increase and drag increase because the wall-normal direction is almost vertical in the present flow conditions. Similar trend regarding the separation bubble size and separated region near the trailing edge is observed in the weak input cases ($C_\mu = 2.0 \times 10^{-5}$:Fig.4.5(b)) with $F^+ = 6.0$ and 10.

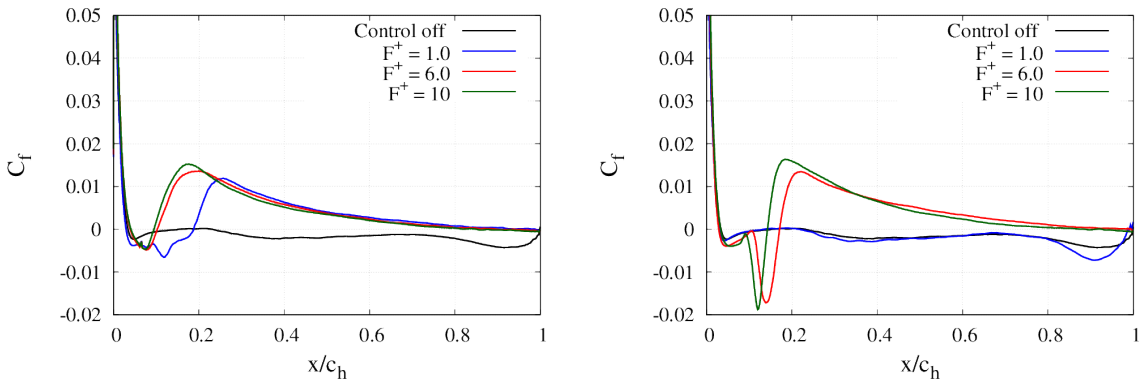

(a) $C_\mu = 2.0 \times 10^{-3}$ (b) $C_\mu = 2.0 \times 10^{-5}$

Fig. 4.4: Skin friction C_f on the airfoil surface: (a)$C_\mu = 2.0\times10^{-3}$ and (b)$C_\mu = 2.0\times10^{-5}$.

The effects of actuation frequency F^+ on time-averaged aerodynamic coefficients are summarized as follows:

1 Leading edge separation bubble size =¿affect CD¿ CL

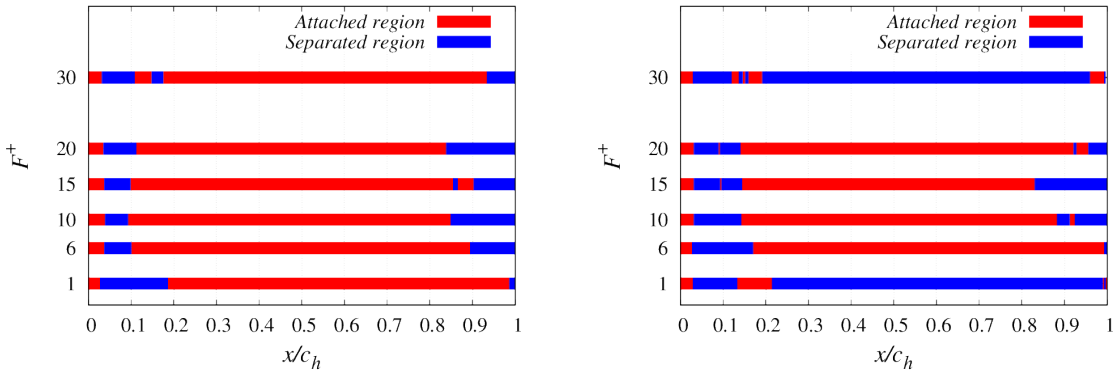

(a) $C_\mu = 2.0 \times 10^{-3}$ (b) $C_\mu = 2.0 \times 10^{-5}$

Fig. 4.5: Separated flow region on the airfoil surface: (a)$C_\mu = 2.0 \times 10^{-3}$ and (b)$C_\mu = 2.0 \times 10^{-5}$.

2 trailing edge separated region =¿affect CL¿ CD

which is dominant? relationship 1 & 2? In the

4.4 Flow fields

In this section, the relationship between the flow fields and two items summarized in the previous section is discussed. The following discussion is mainly based on the time- and spanwise-averaged fields.

4.4.1 Separated region and separation bubble near the leading edge

Figure 4.6 and 4.7 show the time- and spanwise-averaged chordwise velocity fields u/u_∞ and its zoom views. In the strong input cases ($C_\mu = 2.0 \times 10^{-3}$:Fig.4.6(a), (c), and (e)), the flow is attached on almost all the airfoil surface. The reversed flow region appears near the leading edge in each cases, which correspond to the separation bubbles. The size of the separation bubble is more quantitatively visualized in Fig.4.8(a) and (b), where the velocity profiles of a wall-tangential component are visualized on each x/c_h planes; and the reversed flow region is also plotted. The size of reversed flow region is corresponding to that of the separation bubble. The size of the separation bubble is the largest in

$F^+ = 1.0$ (blue color), and $F^+ > 1.0$ cases show smaller ones. Such a trend for the size of the separation bubble is expected in Sec.**??** on the actuation frequency F^+. The significant result in Fig.4.8 is that the size of the separation bubble is further different between $F^+ = 1.0$ and $F^+ > 1.0$ cases as well as the length of the separated-flow region shown in Fig.4.5. This can be explained by the difference of a spatial growth rate of disturbances developing in the separated shear layer, which will be discussed in the next chapter in detail.

In the cases with a weak input ($C_\mu = 2.0 \times 10^{-5}$:Fig.4.6 and 4.7 (b), (d), and (f)), the case with $F^+ = 1.0$ cannot suppress the separation, and the flow is completely separated from the leading edge. The other $F^+ = 6.0$ and 10 cases attain the attached flow with a separation bubble near the leading edge. In addition, Fig.4.8(c) and (d) clearly shows the difference of the separation bubble size in $F^+ = 6.0$ and 10 (in $F^+ = 1.0$ case, the reversed flow region remains and develops along downstream).

Therefore, the results of both strong and weak input cases support the fact that the higher actuation frequency ($F^+ > 1.0$) is significant for generating the smaller separation bubbles. This trend supports the mechanism of (1) in the previous section, i.e., smaller separation bubble gives higher suction peak and drag reduction. Note that another interesting feature is in the comparison of $F^+ = 1$ with strong input case and $F^+ = 6$ with weak input cases as follows. These two controlled flows show almost the same size for the separation bubble (compare the blue line in Fig.4.8(b) with the red line in Fig.4.8(d)). Nevertheless, the C_p distributions are different in their separation bubbles (compare the blue line in Fig.4.3(b) with the red line in Fig.4.3(d)), where the weak input case (red line in Fig.4.3(d)) clearly shows pressure plateau region while the stong input case (blue line in Fig.4.3(b)) shows faster pressure recovery without clear plateau region. Such a difference would arise from that of a turbulent transition on the separation bubble, which is significantly affected by the property of disturbances from the SJ.

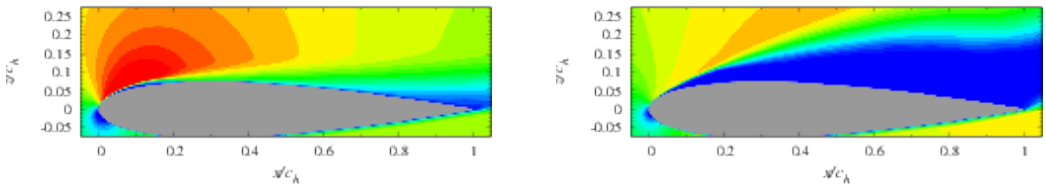

(a) $C_\mu = 2.00 \times 10^{-3}, F^+ = 1.0$ (b) $C_\mu = 2.00 \times 10^{-5}, F^+ = 1.0$

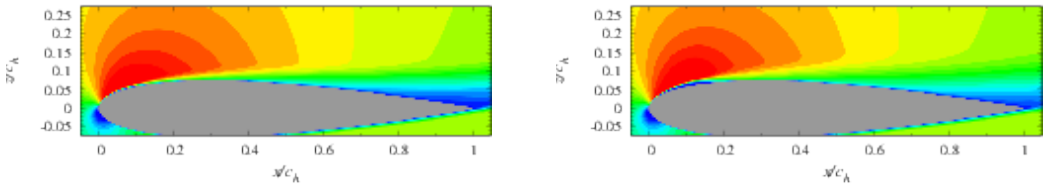

(c) $C_\mu = 2.00 \times 10^{-3}, F^+ = 6.0$ (d) $C_\mu = 2.00 \times 10^{-5}, F^+ = 6.0$

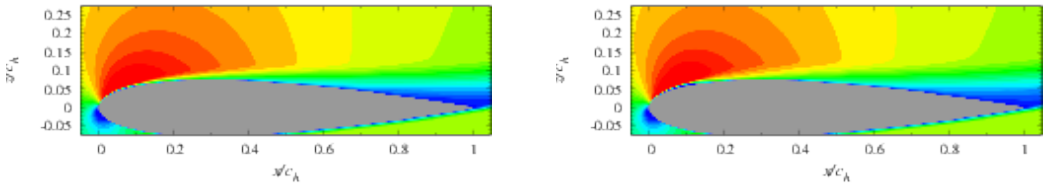

(e) $C_\mu = 2.00 \times 10^{-3}, F^+ = 10$ (f) $C_\mu = 2.00 \times 10^{-5}, F^+ = 10$

Fig. 4.6: Chordwise velocity field (u/u_∞): $0.0 \leq u/u_\infty \leq 1.5$

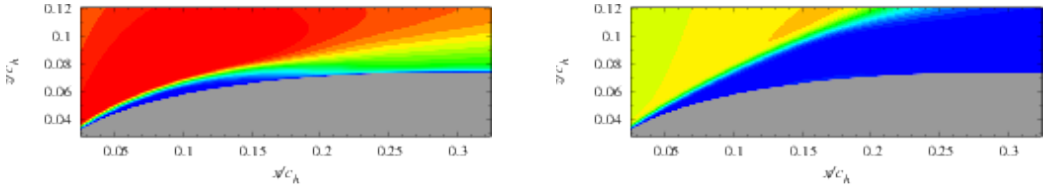

(a) $C_\mu = 2.00 \times 10^{-3}, F^+ = 1.0$ (b) $C_\mu = 2.00 \times 10^{-5}, F^+ = 1.0$

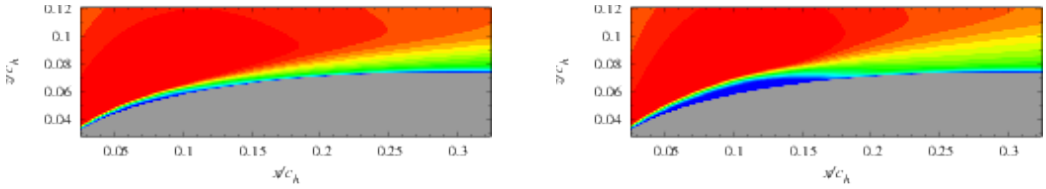

(c) $C_\mu = 2.00 \times 10^{-3}, F^+ = 6.0$ (d) $C_\mu = 2.00 \times 10^{-5}, F^+ = 6.0$

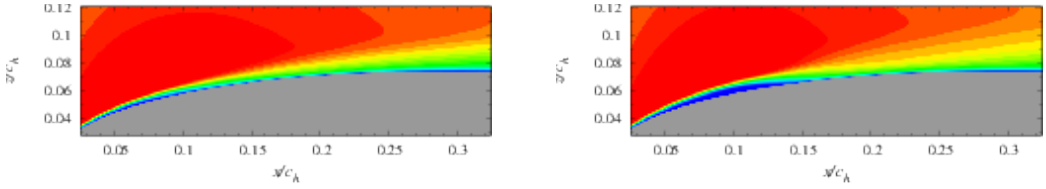

(e) $C_\mu = 2.00 \times 10^{-3}, F^+ = 10$ (f) $C_\mu = 2.00 \times 10^{-5}, F^+ = 10$

Fig. 4.7: Zoom view of chordwise velocity field (u/u_∞) near the leading edge: $0.0 \leq u/u_\infty \leq 1.5$

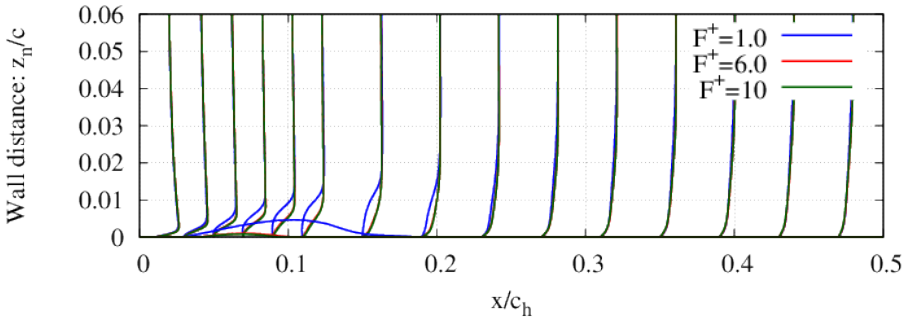

(a) $C_\mu = 2.0 \times 10^{-3}$

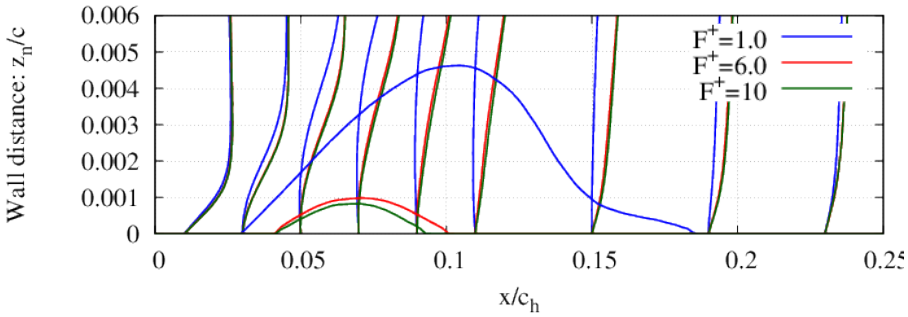

(b) Zoom view of $C_\mu = 2.0 \times 10^{-3}$

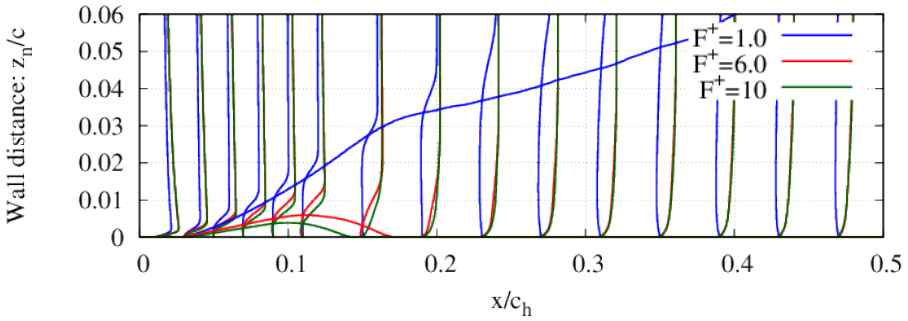

(c) $C_\mu = 2.0 \times 10^{-5}$

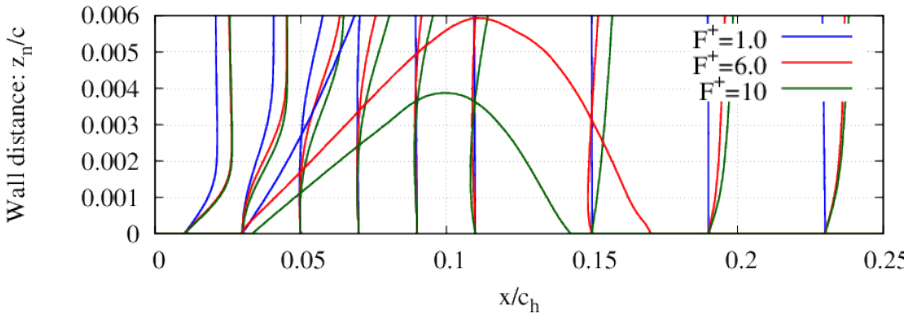

(d) Zoom view of $C_\mu = 2.0 \times 10^{-5}$

Fig. 4.8: Profiles of wall-tangential velocity component and reversed flow region.

4.4.2 Instantaneous flow fields near the separation bubble

The instantaneous flow fields are discussed in terms of turbulent structures on controlled cases. First, the general aspects of the controlled flows are overviewed using Fig.4.9. Figs.4.9 shows instantaneous flow fields of controlled cases with $F^+ = 1.0, 6.0$, and 10 at the beginning of a blowing phase (see Fig.4.10). The isosurface near the airfoil surface is a second invariant of the velocity gradient tensor and is colored by the vorticity in the chordwise direction (the isosurface is visualized on every two grid points in each direction hereinafter). The contour plane normal to the spanwise direction (y-axis) shows the chordwise component of the velocity u/u_∞. In both controlled cases, three-dimensional fine vortex structures are developed, and a turbulent boundary layer covers the airfoil surface when the flow is attached. On the other hand, a two-dimensional separated shear layer appears near the leading edge in both snapshots. Therefore, a laminer separation bubble would be developed near the leading edge when the flow is attached ($C_\mu = 2.0 \times 10^{-3}$ with $F^+ = 1.0, 6.0$, and 10; $C_\mu = 2.0 \times 10^{-3}$ with $F^+ = 6.0$ and 10), where laminer flow is separated near the leading edge and transient to turbulence. The turbulent transition in a laminer separation bubble is typically triggerd by a linear instability of two-dimensional (spanwise uniform) disturbances, i.e., Kelvin-Helmholtz (KH) instability, which will be discussed in detail later. Note that the C_p distribution with a plateau region on the separation bubble, which is discussed in Sec.**??**, is frequently observed in a laminer separation bubble[**?**].

Next, the oscillation of the separation bubble is discussed in Fig.4.11. Figure 4.11 shows the closed view of instantaneous flows at each phase angle ($\varphi/2\pi = 1/10, 3/10, 5/10, 7/10,$ and $9/10$). The phase angle is defined by the actuation frequency F^+ as illustrated in Fig.4.10. In strong input cases ($C_\mu = 2.00 \times 10^{-3}$:Fig.4.11(a)(b)(c)), three-dimensional vortex structure is generated inside the cavity (near the leading edge). In the $F^+ = 1.0$ case, the disturbance is introduced to the separated shear layer near the leading edge at $\varphi/2\pi = 3/10$ which is collapsed and divided into multiple small vortex structures (black dotted circle in Fig.4.11(a)). Interestinglly, although the three-dimensional (spanwise) disturbance from the SJ is clearly observed inside the shear layer, the vortex structures emitted from the shear layer keeps a little two-dimensional (spanwise uniform) shape at $\varphi/2\pi = 3/10$, which is gradually broken down into three-dimensional fine vortex structures. This implies that the two-dimensional disturbances are still dominant and

developing fast inside the shear layer although the three-dimensional fluctuation exists and would enhance a turbulent transition. Similarly, in Fig.4.11(b) and (c) with $F^+ = 6.0$ and 10 actuation, the separated shear layer is broken down into multiple two-dimensional vortex structures with spanwise disturbances from the SJ (black dotted circles). Note that the actuation period is different for each F^+ so that the phase angle when the shear layer is broken down by the disturbances from the SJ is different for each F^+ cases. In weak input cases ($C_\mu = 2.00 \times 10^{-3}$:Fig.4.11(d)(e)(f)), the vortex structure inside the SJ cavity is almost two-dimensional (spanwise uniform) such that no three-dimensional fluctuation appears inside the separated shear layer near the leading edge. In the controllable cases ($F^+ = 6.0$ and 10), the two-dimensional disturbances seem to develop primarily inside the shear layer, which breaks the shear layer together with smaller two-dimensional vortex structures (black dotted circles). The difference from the strong input case is that the small vortex structures emitted from the shear layer do not contain a three-dimensional fluctuation generated inside the SJ cavity but the one based on flow instability inside the shear layer (e.g., secondary instability). The instability related to the development of two-dimensional (spanwise uniform) disturbances will be discussed in the next chapter.

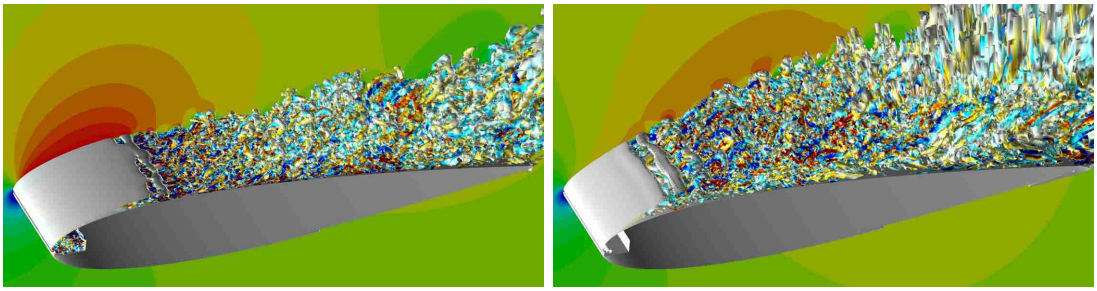

(a) $C_\mu = 2.00 \times 10^{-3}, F^+ = 1.0$ (b) $C_\mu = 2.00 \times 10^{-5}, F^+ = 1.0$

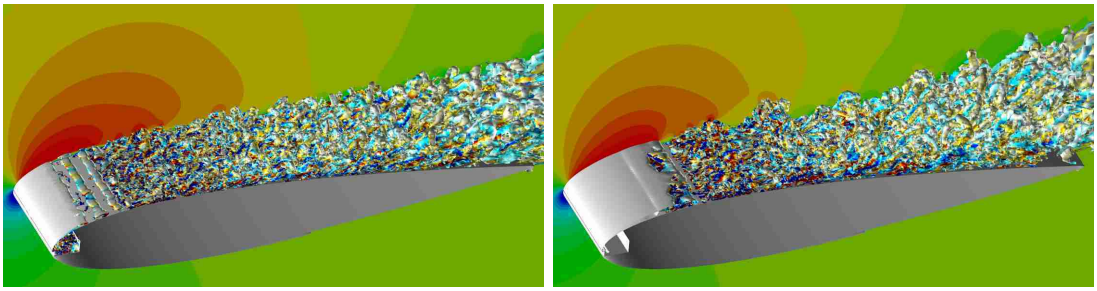

(c) $C_\mu = 2.00 \times 10^{-3}, F^+ = 6.0$ (d) $C_\mu = 2.00 \times 10^{-5}, F^+ = 6.0$

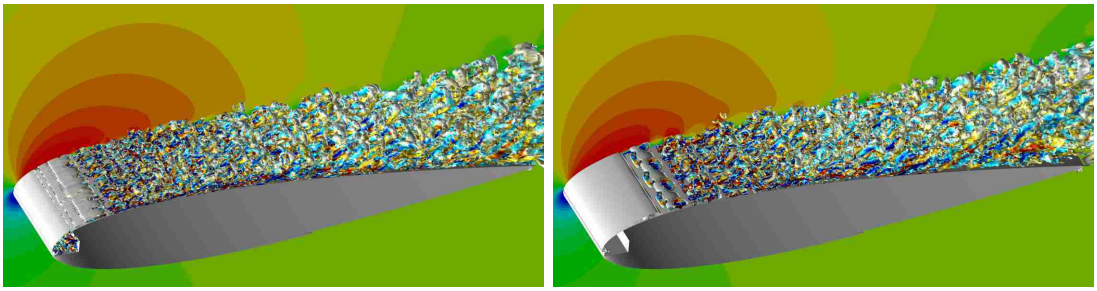

(e) $C_\mu = 2.00 \times 10^{-3}, F^+ = 10$ (f) $C_\mu = 2.00 \times 10^{-5}, F^+ = 10$

Fig. 4.9: Instantaneous flow fields (u/u_∞): $0.0 \leq u/u_\infty \leq 1.5$

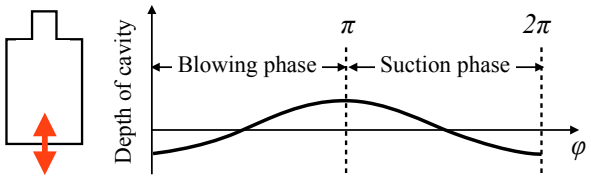

Fig. 4.10: Schematic diagram of phases for actuation

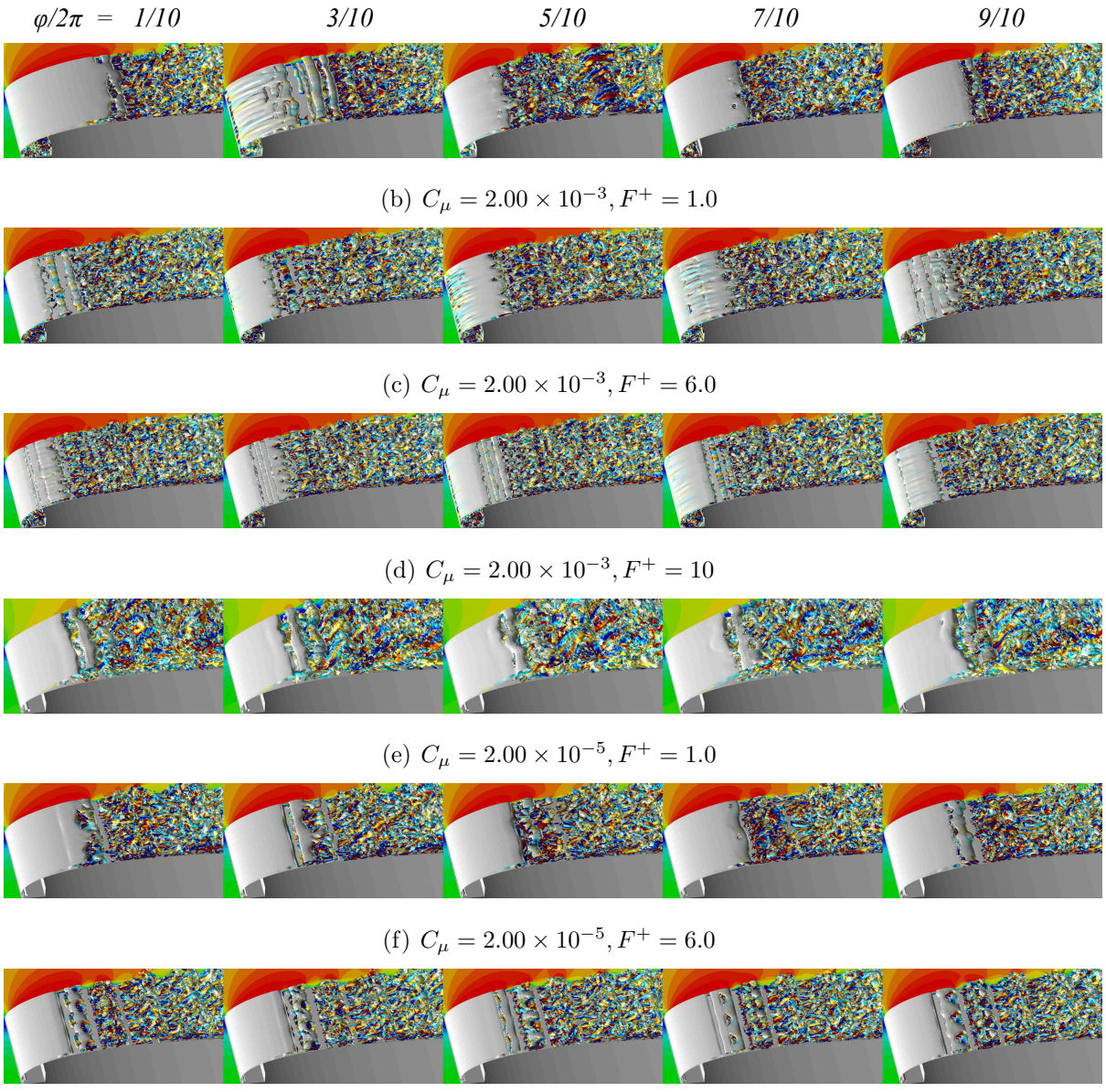

(b) $C_\mu = 2.00 \times 10^{-3}, F^+ = 1.0$

(c) $C_\mu = 2.00 \times 10^{-3}, F^+ = 6.0$

(d) $C_\mu = 2.00 \times 10^{-3}, F^+ = 10$

(e) $C_\mu = 2.00 \times 10^{-5}, F^+ = 1.0$

(f) $C_\mu = 2.00 \times 10^{-5}, F^+ = 6.0$

(g) $C_\mu = 2.00 \times 10^{-5}, F^+ = 10$

Fig. 4.11: Instantaneous flow fields (u/u_∞): $0.0 \leq u/u_\infty \leq 1.5$

4.4.3 PSD of velocity fluctution

In this section, the power spectra density (PSD: see Sec.**??**) of the wall-normal velocity component (u_w) is discussed. Figure 8.3 shows the PSD of u_w in $x/c_h = 0$ to 0.2, and the grey straight line indicates the Kolmogorov's 5/3 law. The sampling points are determined at each x/c_h so that the turbulent kinetic energy takes its maximum along each grid line from the airfoil surface (see Fig.**??**). Most of these sampling points would be located near the center line of the shear layer (Appendix **??**). In all cases, the PSD at high frequencies ($\simeq 100$) is close to the Kolmogorov's law at $x/c_h = 0.2$, where a turbulent boundary layer is well developed.

In strong input cases ($C_\mu = 2.0 \times 10^{-3}$: Fig.8.3(a), (c), and (e)), the peaks which correspond to the actuation frequency F^+ and its harmonic component remain even at 20% of the chord length. This indicates that some flow structure periodically appears inside the turbulent boundary layer, whose period is the same as F^+. Therefore, the phase averaging procedure based on the actuation frequency F^+ is expected to extract such flow structures (see next section). Since such periodic flow structure remains further downstream, the aerodynamic coefficients would be periodically fluctuated in F^+ (Fig.**??**). Finally, another remarkable characteristic is the rapid growth of PSD at $St \simeq 40$ from $x/c_h = 0.02$ (blue lines) to 0.05 (red lines) although its frequency is significantly different from the actuation frequency $F^+ = 1.0$ to 10. Such a spatial growth of high-frequency disturbances would be related to the KH instability, which will be discussed in the next chapter.

The weak input cases ($C_\mu = 2.0 \times 10^{-5}$: Fig.8.3(b), (d), and (f)) show similar trends to the strong input cases when the attached flow is achieved ($F^+ = 6.0$ and 10 cases). However, the PSD near the leading edge is much lower than that of strong input cases in $F^+ = 6.0$ and 10 cases, which indicates that the disturbances from the SJ is dominant in terms of the wall-normal fluctuation near the leading edge. In the uncontrollable case ($F^+ = 1.0$), the actuation frequency does not have a peak, but the PSD of $St \simeq 15$ selectively develops near the leading edge. This would be related to the two-dimensional vortex structures emitted from the shear layer (see Fig.4.11(d)), which will be validated in the next chapter in detail.

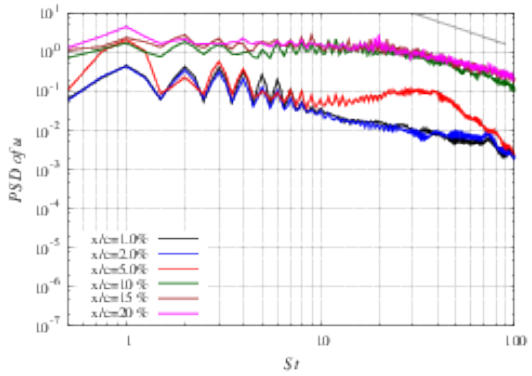

(a) $C_\mu = 2.00 \times 10^{-3}, F^+ = 1.0$

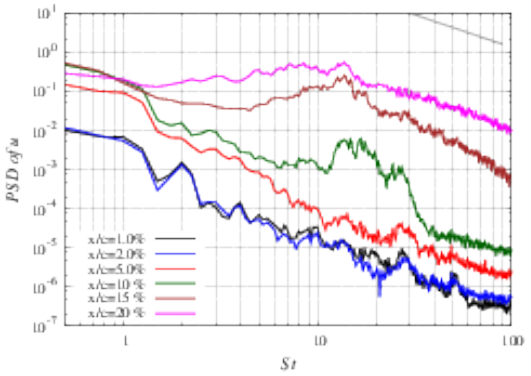

(b) $C_\mu = 2.00 \times 10^{-5}, F^+ = 1.0$

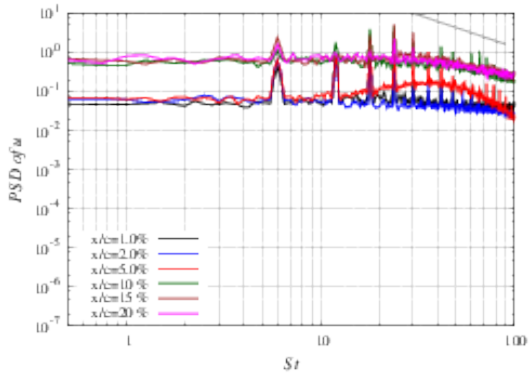

(c) $C_\mu = 2.00 \times 10^{-3}, F^+ = 6.0$

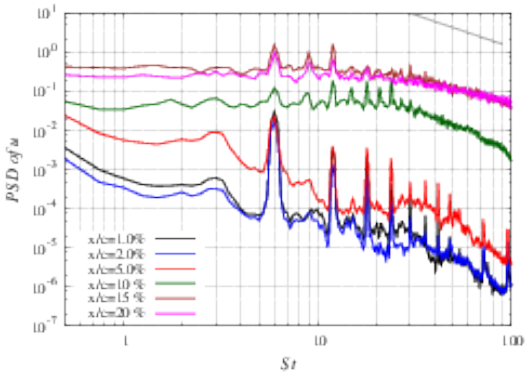

(d) $C_\mu = 2.00 \times 10^{-5}, F^+ = 6.0$

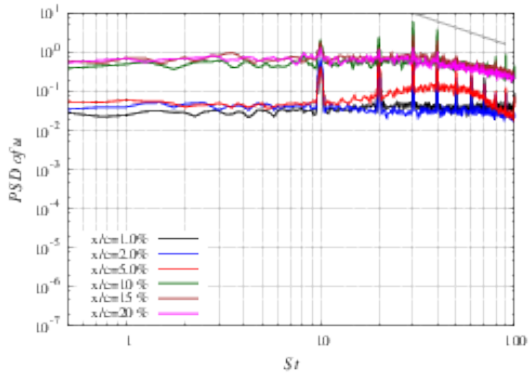

(e) $C_\mu = 2.00 \times 10^{-3}, F^+ = 10$

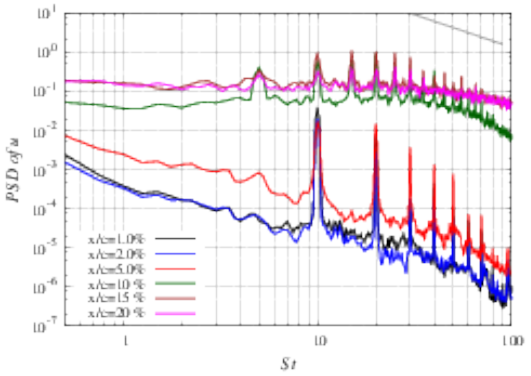

(f) $C_\mu = 2.00 \times 10^{-5}, F^+ = 10$

Fig. 4.12: Power spectra of wall-normal velocity component; the horizontal axis is a frequency normalized by freestream velocity and chord length. The straight line in grey color shows the Kolmogorov's 5/3 law.

4.5 Turbulent statistics including the evaluation of chordwise momentum exchange

In this section, the turbulent statistics are discussed from the viewpoint of turbulent transition and chordwise momentum exchange.

4.5.1 Turbulent transition point

Figure 4.13 shows the spatial distribution of a turbulent kinetic energy for controlled cases. When the flow is controlled to the attached one, the high TKE appears inside the turbulent boundary layer due to the three-dimensional turbulent vortex strucutures. On the other hand, when the separation is not suppressed ($C_\mu = 2.0 \times 10^{-5}$ with $F^+ = 1.0$), the TKE becomes high for the wide region over an airfoil where the turbulent vortex structures are generated. The other important issue is the location where TKE takes a maximum value. In the controllable cases (Fig.4.13(a), (c), (d), (e), and (f)), the higher TKE value appears near the leading edge, which is on the separation bubble. As the separation bubble size become smaller (higher F^+ generates smaller separation bubble discussed in Sec.**??**), the higher TKE region (red colored region) becomes smaller. For example, the higher TKE region in $F^+ = 6.0$ or 10 cases (Fig.4.13(c) and (e)) is smaller than that of $F^+ = 1.0$ (Fig.4.13(a)).

Figure 4.14 shows the wall-normal profiles of TKE values for $0 \leq x/c_h \leq 0.5$ more quantitatively. Compared with the reversed flow region of Fig.4.8 and instantaneous flow fields Fig.4.11, the following two points are summarized for controllable cases. First, the z_n/c_h location (wall-normal distance from the airfoil surface) wher TKE takes maximum value is approximately at the outer edge of the separation bubble, where the shear layer exists. Second, the x/c_h location where TKE takes maximum value is at the latter half of the separation bubble, where the smaller vortex strcutures are emitted from the separated shear layer along with a three-dimensional fluctuation. These two characteristics suggest that the TKE value would become higer where small vortex structures are emitted from the shear layer and transient to turbulence. Similar trend is observed in the uncontrollable case ($C_\mu = 2.0 \times 10^{-5}$ with $F^+ = 1.0$). The details of the relationship between unsteady vortex motion and flow disturbances will be discussed in Sec.**??**.

The peak values of TKE are different for each F^+ cases, which is clearly visualized in Fig.**??**. Figure **??** visualize the spatial distribution of maximum value of TKE for $0 \leq x/c_h \leq 1.0$, where the peak values of TKE at each x/c_h are plotted (hereinafter, called TKE-max plot). As mentioned in the previous paragraph, the peak of the TKE value is almost corrsponding to the turbulent transition point []. First, the black lines in Fig.**??** show the cases without control. In this case, the small vortex structures are emitted from the separated shear layer, where the two-dimensional structures are gradually broken down with a three-dimesnional fluctuation (see Fig.4.11). This suggests that the turbulent transition would occur slowly, thus the profile of TKE-max is more widely spread (e.g., the half width of the TKE-max plot shows larger value) than controlled (with separation bubbles) cases. In strong input cases ($C_\mu = 2.0 \times 10^{-3}$: blue, red, and green lines in Fig.**??**(a)), the $F^+ = 6.0$ and $F^+ = 10$ cases show its maximum value at more upstream position than $F^+ = 1.0$ case. It is the same trend with the separation bubble size (Sec.**??**), and the turbulent transition would occur smoothly at more upstream position in $F^+ = 6.0$ and 10 than $F^+ = 1.0$ case. In weak input and controllable cases ($C_\mu = 2.0 \times 10^{-5}$ with $F^+ = 6.0$ and 10: red and green lines in Fig.**??**(b)), the $F^+ = 10$ case clearly show its maximum value at more upstream position than $F^+ = 6.0$ case. This is the same reason as in the strong input cases, where the turbulent transition occurs smoothly at more upstream position in $F^+ = 10$ than $F^+ = 6.0$ case. Therefore, the better control based on the small separation bubbles (in terms of minimizing the drag) is achieved by the enhancement of the turbulent transition at more upstream position. Note that even in the uncontrollable case ($C_\mu = 2.0 \times 10^{-5}$ with $F^+ = 1.0$: blue line in Fig.**??**(b)), the maxmium point is slightly upstream compared to the baseline case (control off: black solid line). Such a enhancement of turbulent transition is caused by small disturbances from the SJ although it cannot attain the suppression of the seprated flows.

The previous criteria of the turbulent transition point was based on turbulent kinetic energy, which includes fluctuations in all the velocity component. In terms of the extraction of three-dimensional structures, the similar plots for spanwise fluctuation are also helpful. Figures 4.16 and 4.17 show the spanwise fluctuation v' for controlled cases. The trend of maximum spanwise fluctuation (v'-max) point for F^+ is almost the same with that of TKE-max in Fig.4.17 and 4.15. That is, the turbulent transition occurs smoothly

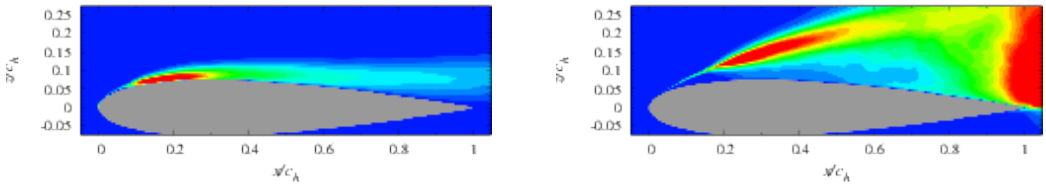

(a) $C_\mu = 2.00 \times 10^{-3}, F^+ = 1.0$

(b) $C_\mu = 2.00 \times 10^{-5}, F^+ = 1.0$

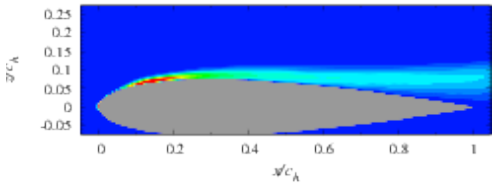

(c) $C_\mu = 2.00 \times 10^{-3}, F^+ = 6.0$

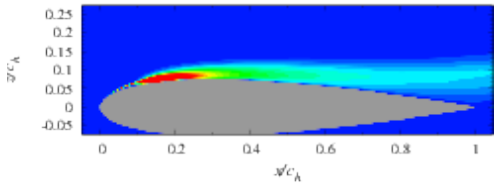

(d) $C_\mu = 2.00 \times 10^{-5}, F^+ = 6.0$

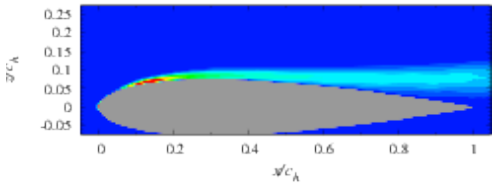

(e) $C_\mu = 2.00 \times 10^{-3}, F^+ = 10$

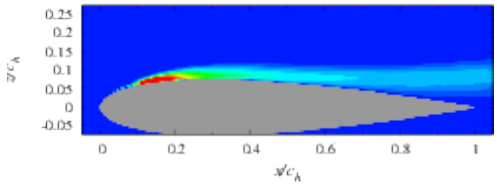

(f) $C_\mu = 2.00 \times 10^{-5}, F^+ = 10$

Fig. 4.13: Turbulent kinetic energy

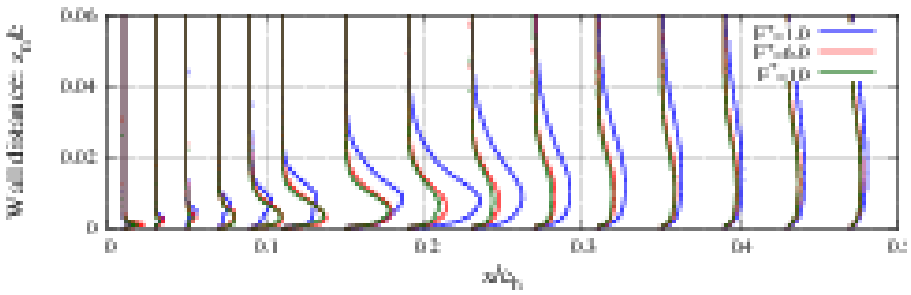

(a) $C_\mu = 2.0 \times 10^{-3}$

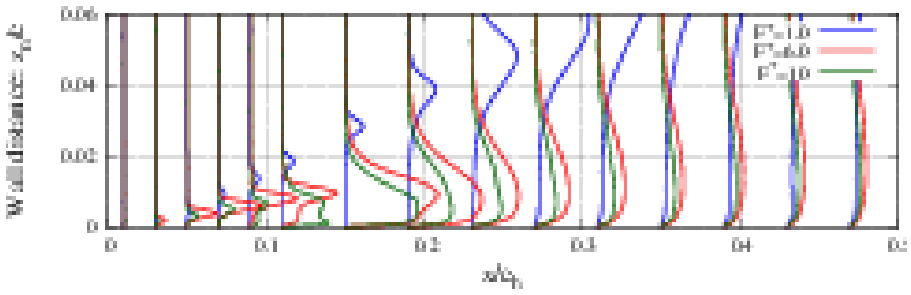

(b) $C_\mu = 2.0 \times 10^{-5}$

Fig. 4.14: Profiles of TKE near the leading edge ($0 \leq x/c_h \leq 0.5$)

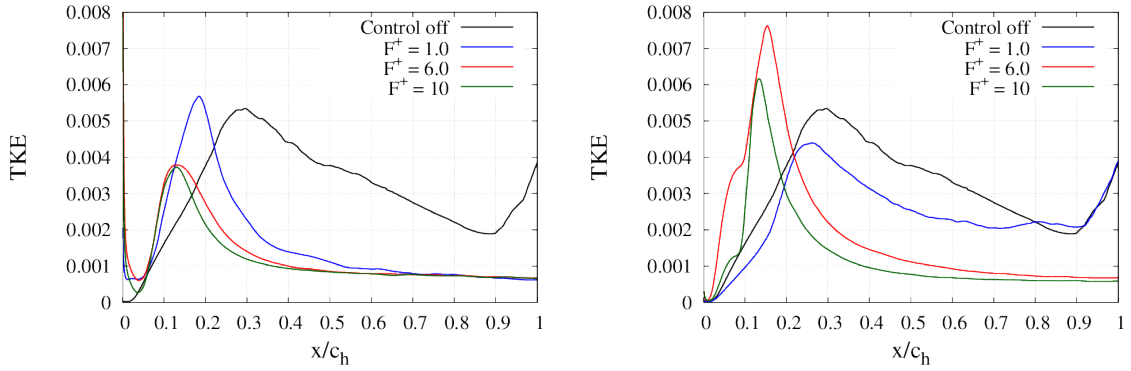

(a) $C_\mu = 2.0 \times 10^{-3}$ (b) $C_\mu = 2.0 \times 10^{-5}$

Fig. 4.15: Profiles of maximum TKE near the leading edge ($0 \leq x/c_h \leq 0.5$)

at more upstream position in the higher F^+ cases. Therefore, the criteria of TKE-max is sufficient for the evaluation of turbulent transition point, and the TKE-max position at each x/c_h will be frequently adopted as a sampling point for unsteady flow properties in this thesis.

4.5.2 Decomposition of turbulent statistics by the phase-averaging procedure

As discussed in the previous section, the PSD of wall-normal velocity component suggests the existence of periodic flow structures in the turbulent boundary layer, whose period is corresponding to the actuation frequency F^+. Therefore, the phase averaging procedure is conducted for the unsteady flow fields to extract these structures, and the turbulent statistics, e.g., turbulent kinetic energy, are decomposed into periodic and turbulent (non-periodic) components. Hereinafter, the instantaneous physical quantity $f = f(t, x, y, z)$ is decomposed into overall average, $\overline{f}$; phase fluctuation, $\tilde{f}$; and turbulent fluctuation, f''. The phase average is denoted by $\langle f \rangle$. The detail of the decomposition was explained in Sec.**??**. Note that in this chapter, all the quantities are averaged in the spanwise direction, of which symbol is omitted for the brevity.

The separation control mechanism is frequently discussed with a chordwise momentum exchange near the airfoil surface. In terms of the momentum exchange in the chordwise direction, it is essential to evaluate the Reynolds shear stress because the present

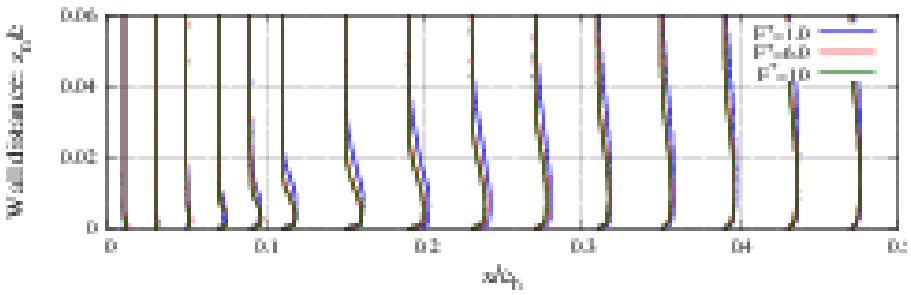

(a) $C_\mu = 2.0 \times 10^{-3}$

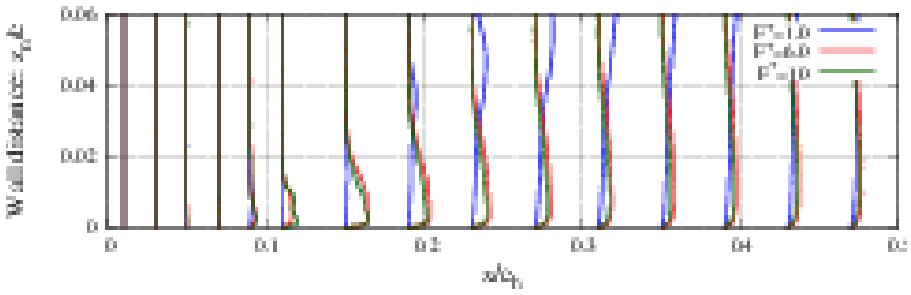

(b) $C_\mu = 2.0 \times 10^{-5}$

Fig. 4.16: Profiles of spanwise fluctuation (v') near the leading edge ($0 \leq x/c_h \leq 0.5$)

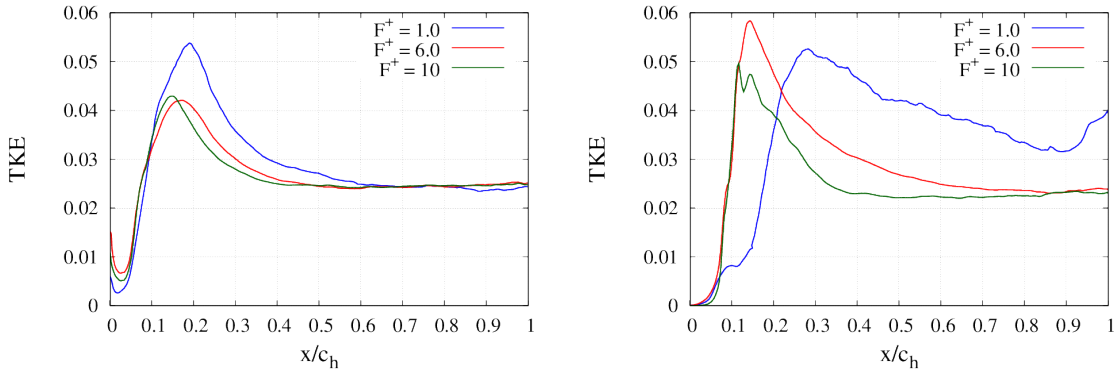

(a) $C_\mu = 2.0 \times 10^{-3}$ (b) $C_\mu = 2.0 \times 10^{-5}$

Fig. 4.17: Profiles of the maximum spanwise fluctuation v' near the leading edge ($0 \leq x/c_h \leq 0.5$)

controlled flow exhibits the turbulent boundary layer almost all over the airfoil surface. Based on the phase decomposition above, three types of Reynolds shear stress can be defined in the present study. The first one is the overall component of the fluctuation: $\overline{u'w'}$, which is defined by the overall flucutaion from the time-averaged flows. The second and third ones are the phase and turbulent component, respectively: $\overline{\tilde{u}\tilde{w}}$ and $\overline{u''w''}$, which are based on the phase and turbulent component of the fluctuation, respectively. These three types of Reynolds shear stress are related as follows:

$$\overline{u'w'} = \overline{\tilde{u}\tilde{w}} + \overline{u''w''}. \tag{4.7}$$

Note that in the present section, the Reynolds shear stress comprise x and z components of fluctuation (u' and w') because the entrainment of chordwise momentum (u') by vertical flow motion ($-w'$) is focused.

Figure 4.18 shows the phase decomposition of the Reynolds shear stress in controlled flows. The left column show the overall component of $\overline{u'w'}$, middle and right column show the phase and turbulent components of $\overline{\tilde{u}\tilde{w}}$ and $\overline{u''w''}$. The result indicates that in all the controlled cases, the turbulent component $\overline{u''w''}$ is dominant for almost all the region. In other words, the chordwise momentum exchange is chiefly achived by the turbulent fluctuation, which is generated by three-dimensional turbulent vortex strucutures. The first important issue is that such an unsteady motion of turbulent vortex structures is not strongly related to F^+ and are not spanwise-uniformly distrubuted, thus the turbulent component becomes dominant in terms of the decomposed Reynolds shear stress. It is interesting that such a feature, i.e., turbulent component being dominant, is commonly observed regardless of F^+ and C_μ when the separation is suppressed. In this way, the turbulent structure is one of the important mechanism for momentum exchange in sepration control in the present flow/actuator conditions, thus the enhancement of turbulent transition would be a significant issue as is expected in the previous section.

Figure **??** more precisely shows the profiles of Reynolds shear stress in wall-normal direction. In each controlled cases, the turbulent component is dominant for almost all the airfoil surface as discussed in the previous paragraph and Fig.4.18. The periodic component, on the other hand, is locally enhanced near the leading edge (at the latter half of the separation bubble) for each controlled cases (red, blue, and green lines in Fig.**??**(a); blue and green lines in Fig.**??**(b)). Therefore, some periodic flow motion

based on F^+ is expected at this location. The small vortex structures emitted from the separated shear layer would be related to this unsteady motion from the discussion on instantaneous flow fields near the separation bubble, which will be verified in detail using phase averaged flow fields in the next section.

4.6 Mechanism of chordwise momentum exchange by unsteady flow motion

In the previsous section, the effect of chordwise momentum exchange is decomposed into periodic and turbulent components, and the turbulent component is shown to be dominant for each controlled cases. On the other hand, periodic component is locally enhanced near the separation bubble, which indicates that some periodic flow motion appears at the downstream of the separation bubbles. In this section, the phase averaged flow fields are discussed at each phase angle from the viewpoint of coherent (spanwise uniform) vortex strucutre and Reynolds shear stress.

For this purpose, the following decomposition is conducted for the Reynolds shear stress at each phase angle (the phase angle was illustrated in Fig.4.10):

$$\langle u'w' \rangle_\varphi = \langle \tilde{u}\tilde{w} \rangle_\varphi + \langle u''w'' \rangle_\varphi. \tag{4.8}$$

Note that spanwise averaging procedure is also conducted but the symbol for this operation is omitted for the brevity. The detail of the computation of each Reynolds stress is explained in Sec.**??**.

4.6.1 Coherent vortex structures and chordwise momentum exchange in phase-averaged flow fields

In Figs.**??**–**??**, the decomposition of the Reynolds shear stress is shown. The black contour lines indicate the second invariant of the velocity gradient tensor, which corresponds to vortex structures with its axis along the spanwise (y) direction. In this section, the following three points are summarized: 1) coherent vortex structure; 2) periodic component of Reynolds shear stress; 3) turbulent component of Reynolds shear stress.

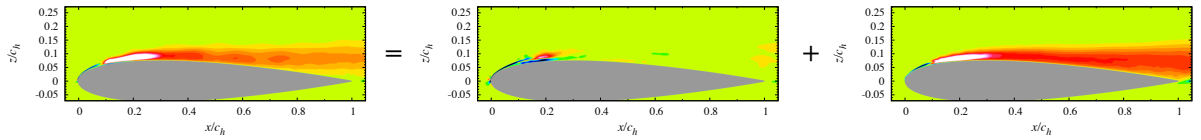

(a) $C_\mu = 2.00 \times 10^{-3}, F^+ = 1.0$

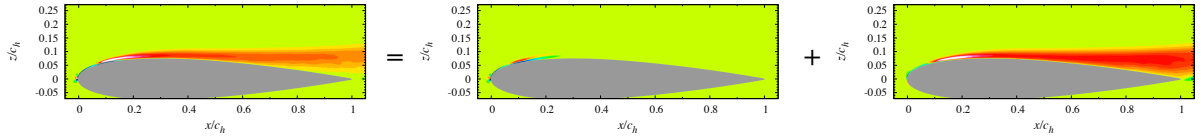

(b) $C_\mu = 2.00 \times 10^{-3}, F^+ = 6.0$

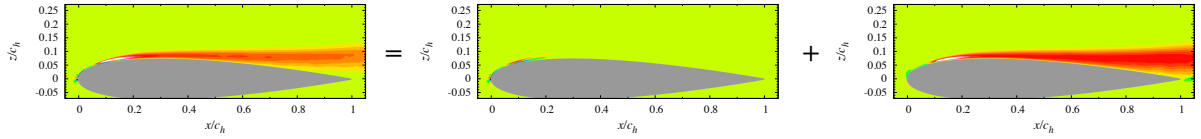

(c) $C_\mu = 2.00 \times 10^{-3}, F^+ = 10$

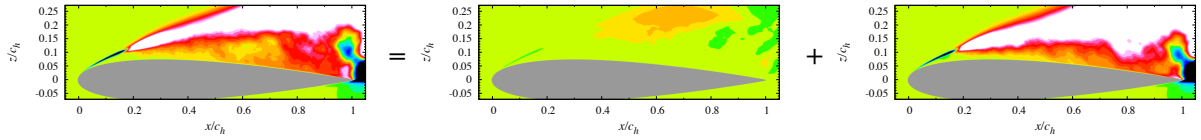

(d) $C_\mu = 2.00 \times 10^{-5}, F^+ = 1.0$

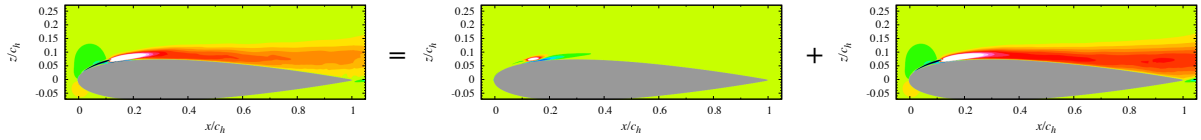

(e) $C_\mu = 2.00 \times 10^{-5}, F^+ = 6.0$

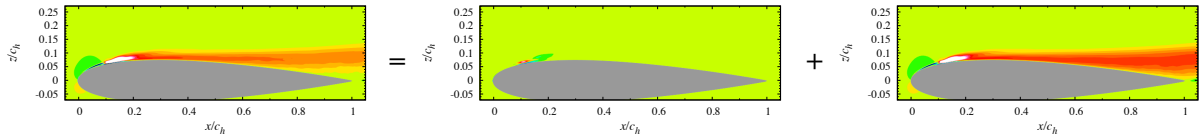

(f) $C_\mu = 2.00 \times 10^{-5}, F^+ = 10$

Fig. 4.18: Decomposition of the Reynolds shear stress: left column shows the overall component of $\overline{u'w'}$, middle and right column show the phase and turbulent components of $\overline{\tilde{u}\tilde{w}}$ and $\overline{u''w''}$.

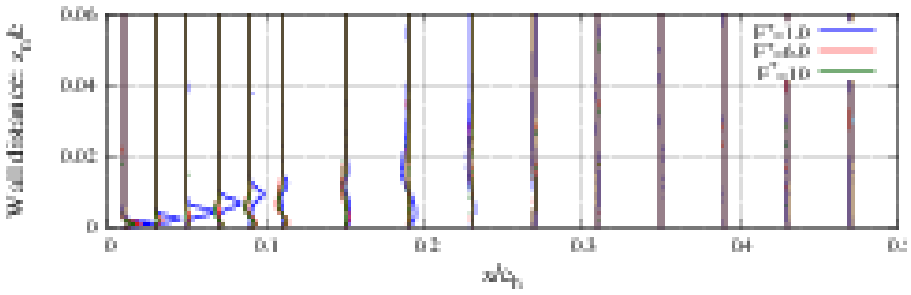

(a) Periodic

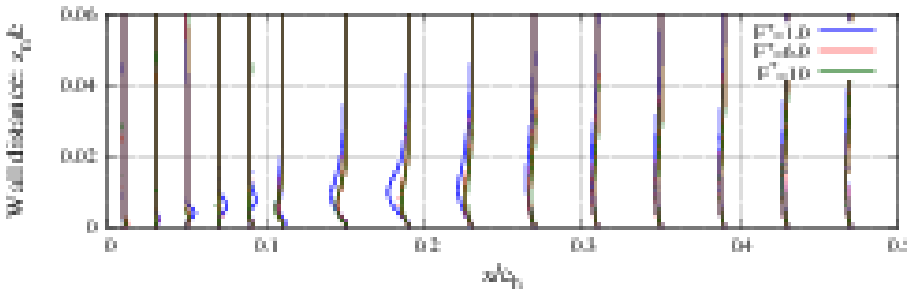

(b) Turbulent

Fig. 4.19: $C_\mu = 2.0 \times 10^{-3}$ cases. Decomposition of the Reynolds shear stress: the phase and turbulent components of (a)$\widetilde{\tilde{u}\tilde{w}}$ and (b)$\overline{u''w''}$.

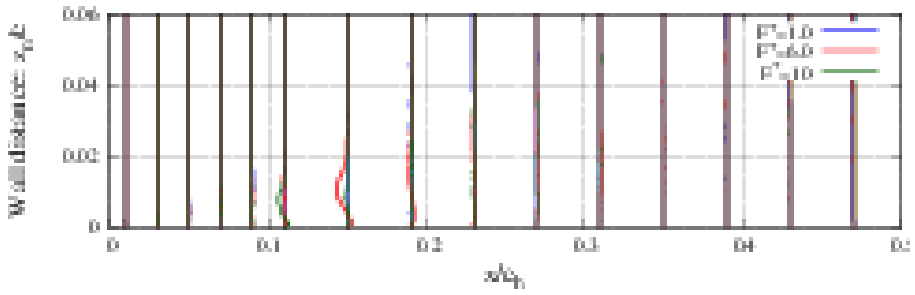

(a) Periodic

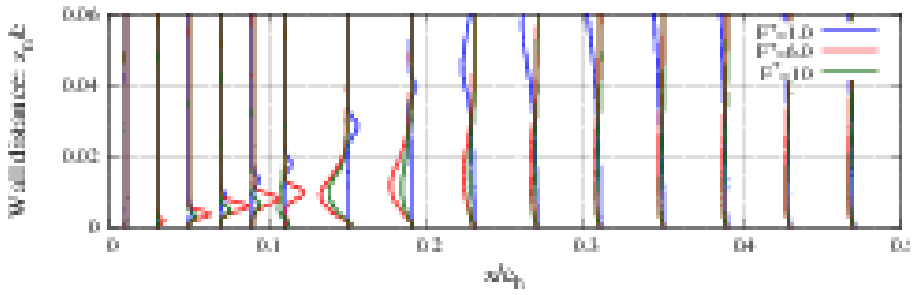

(b) Turbulent

Fig. 4.20: $C_\mu = 2.0 \times 10^{-5}$ cases. Decomposition of the Reynolds shear stress: the phase and turbulent components of (a)$\overline{\tilde{u}\tilde{w}}$ and (b)$\overline{u''w''}$.

Coherent vortex with the period of F^+

In each controlled cases, the coherent vortex structures are detected by black contour lines. In the strong input case $C_\mu = 2.0 \times 10^{-3}$ with $F^+ = 1.0$ (Fig.4.21(a) and (b)), the separated shear layer is visualized near the leading edge at $\varphi/2\pi = 1/10$. At $\varphi/2\pi = 2/10$, the shear layer is divided into small vortex strucutures. These vortex structures are shedding downstream, and one of them remains strong further downstream as a coherent vortex inside the turbulent boundary layer. The generation of single coherent vortex would be caused by both of small vortex merging and diffusion (see next subsection). In this way, these phase averaged shots illustrate that the separation bubble is oscillated with its period being F^+, and the multiple coherent vortex structures are generated from the separation bubble, one of which strongly remains further downstream. Such a resultant single coherent vortex goes through an airfoil surface and is emitted from the trailing edge periodically (the same period as F^+). The fluctuation of aerodynamic coefficients shown in Fig.4.1 would be strongly related to this coherent vortex structure. The similar trend is observed in the strong input case $C_\mu = 2.0 \times 10^{-3}$ with $F^+ = 6.0$ and 10 (Fig.4.21(a) and (b)). In $F^+ = 6.0$ and 10 cases, the number of coherent vortices is much more than that in $F^+ = 1.0$, which is almost corresponding to the F^+. Another different feature is that the strength of the coherent vortex, which remains more strongly (clearly in the visuallization) further downstream in the $F^+ = 1.0$ case than the 6.0 and 10 cases. Since the $F^+ = 1.0$ case attains larger attached region than the $F^+ = 6.0$ and 10 cases, the strong coherent vortex can suppress the separation near the trailing edge which is achived by the lower ($F^+ = 1.0$) actuation frequency. Note that the coherent vortex tends to strongly remain near the trailing edge when it is generated more downstream. Similar trend has been reported in the previous study for "MF" and "HF" (middle and high frequencies) cases in Zhang et al. [34].

In the weak input cases $C_\mu = 2.0 \times 10^{-5}$ with $F^+ = 6.0$ and 10 (controllable cases: Fig.4.24), similar trend is observed where the coherent vortices are generated periodically on the airfoil surface and emitted from the trailing edge based on F^+. On the other hand, the location where small vortex structures are emitted from the separated shear layer is more downstream than the strong input cases with $F^+ = 6.0$ and 10, which indicates that the separation bubble is larger than the strong input cases (as discussed in Sec. **??**). Therefore, the coherent vortex is generated by small vortices merging and diffusion more

downstream than the strong input cases. This would contribute to the strong coherent vortex near the trailing edge as discussed in the previous paragraph, but the energy of disturbances input from the SJ is smaller than the strong input cases so that the resultant coherent vortex remains weaker downstream than strong input cases. The difference in the energy of the disturbances input from the SJ and its spatial growth will be discussed in detail in the next chapter. In the case of $C_\mu = 2.0 \times 10^{-5}$ with $F^+ = 1.0$, the separated flow cannot be suppressed. In this case, the coherent vortex cannot be clearly observed as in the controllable cases although the periodic oscillation based on $F^+ = 1.0$ slightly appears at the edge of separated shear layer near the leading edge.

Periodic component of the Reynolds shear stress

In the present decomposition, the periodic component of the Reynolds shear stress strongly appears where the unsteady flow motion is periodic with its period corresponding to F^+. Such periodic flow motion is typically observed at the oscillated separation bubble and on the coherent vortex structures.

In the strong input case with $F^+ = 1.0$ (Fig.4.21(a) and (c)), the periodic component is strongly enhanced at the edge of the separation bubble at $\varphi/2\pi = 1/10$ first, then it surrounds the small vortex structures at $\varphi/2\pi = 3/10$ and also the coherent vortex at $\varphi/2\pi = 5/10$ to $9/10$. Such a quadrupole distribution of the Reynolds shear stress $-\langle\tilde{u}\tilde{w}\rangle_\varphi$ frequently appears around the strong two-dimensional (spanwise uniform) vortex structures, which are rotating in the clockwise direction. Therefore, the periodic component of the Renolds shear stress is more enhanced around two-dimensional strong vortex structures such as single coherent vortex remaining further downstream. In the cases with $F^+ = 6.0$ and 10, the similar quadrupole distributions appear around the small and coherent vortices at $\varphi/2\pi = 5/10$ to $9/10$. However, the strength of the periodic component is weaker than the case with $F^+ = 1.0$, which indicates that in the $F^+ = 6.0$ and 10 cases, the coherent vortex does not contribute to the chordwise momentum exchange by periodic component compared to the $F^+ = 1.0$ case. This would strongly related to the trailing edge separated region as discussed in the characteristics of the coherent vortex previously. In the cases with weak input of $C_\mu = 2.0 \times 10^{-5}$ (Figs.4.25 and 4.26), the similar trend is observed for the periodic component of the Reynolds shear stress, which is, however, weaker than the cases of strong input because the energy of the disturbances

input from the SJ is smaller.

To summarize, the most important characteristic here is that the periodic component of the Reynolds shear stress is localized only around the coherent vortices, which is not dominant over an airfoil since its strength is quickly decreased downstream.

Turbulent component of the Reynolds shear stress

The turbulent component of the Reynolds shear stress strongly appears where the unsteady flow motion is nonperiodic (not related to the period of F^+). In the present flow field, such unsteady flow motion is frequently appears together with the three-dimensional turbulent vortex structures over an airfoil.

In the cases with a strong input with $F^+ = 1.0$ (Fig.4.21(b) and (d)), the strong turbulent component covers almost all the airfoil surface for each phases, which supports the discussion on the decomposition of the total component of Reynolds shear stress in Sec.**??**. In particular, the turbulent component is locally enhenced inside the small vortex structures emitted from the separation bubble at $\varphi/2\pi = 1/10$ and $3/10$. This is because the strong three-dimensional fluctuation appears in the turbulent transition as discussed in Sec.**??** and **??**. The important point is that such a locally-enhanced turbulent component of Reynolds shear stress convects downstream together with the coherent vortex. This indicates that the strong turbulent component (therefore the three-dimensional turbulent vortex structure) is entrained by coherent vortex convecting downstream. Therefore, the coherent vortex periodically generated and convecting downstream shows significance not only for the chordwise momentum exchange by a periodic component of the Reynolds shear stress but also for its turbulent (nonperiodic) component. Such a turbulent component is dominant and further stronger than periodic component.

In the strong input cases with $F^+ = 6.0$ and 10, the similar trend is observed: the turbulent component is locally enhanced inside the small vortex structures emitted from the separation bubble at $\varphi/2\pi = 1/10$ and $3/10$, and the strong component is entrained by the coherent vortex convecting downstream. Resultantly, the turbulent component of the Reynolds shear stress covers almost all over the airfoil surface, which becomes dominant for the chordwise momentum exchange in these cases. The similar trend appears in the weak input cases with $F^+ = 6.0$ and 10.

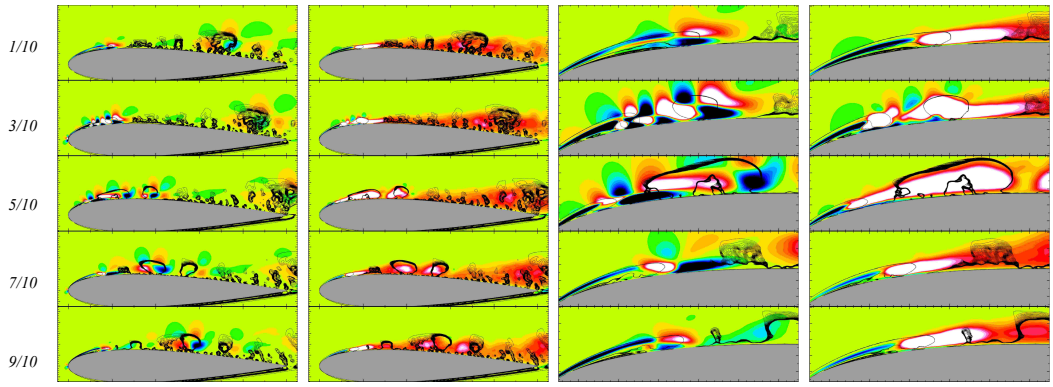

(b) Periodic (c) Turbulent (d) Periodic (e) Turbulent

Fig. 4.21: Coherent vortex structures and Reynolds shear stress: $C_\mu = 2.0 \times 10^{-3}, F^+ = 1.0$ case

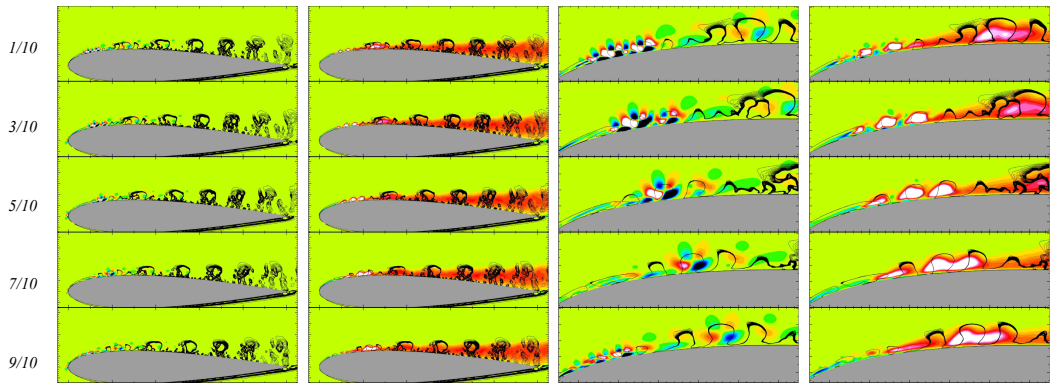

(b) Periodic (c) Turbulent (d) Periodic (e) Turbulent

Fig. 4.22: Coherent vortex structures and Reynolds shear stress: $C_\mu = 2.0 \times 10^{-3}, F^+ = 6.0$ case

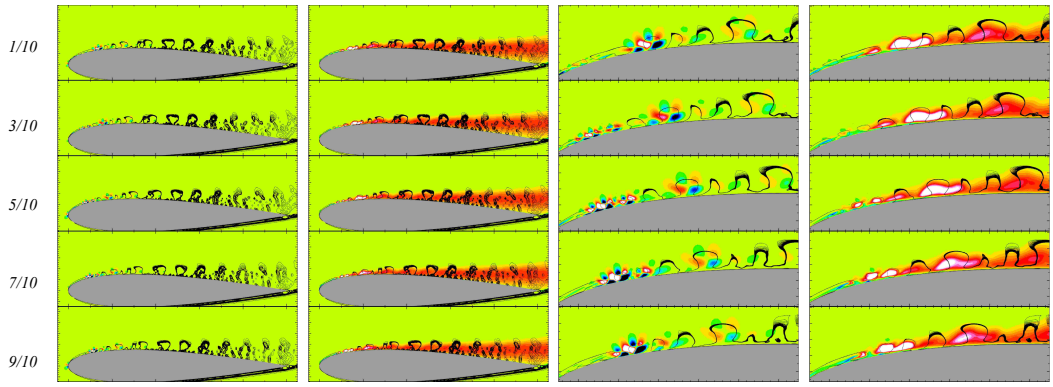

(b) Periodic (c) Turbulent (d) Periodic (e) Turbulent

Fig. 4.23: Coherent vortex structures and Reynolds shear stress: $C_\mu = 2.0 \times 10^{-3}, F^+ = 10$ case

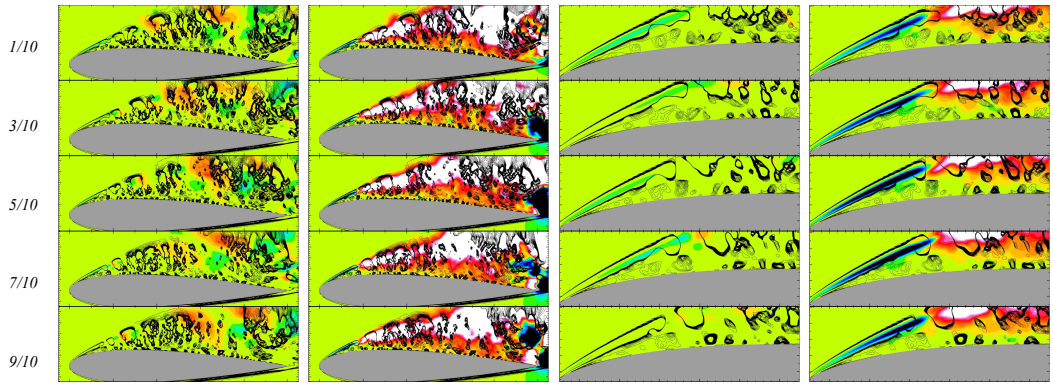

(b) Periodic (c) Turbulent (d) Periodic (e) Turbulent

Fig. 4.24: Coherent vortex structures and Reynolds shear stress: $C_\mu = 2.0 \times 10^{-5}, F^+ = 1.0$ case

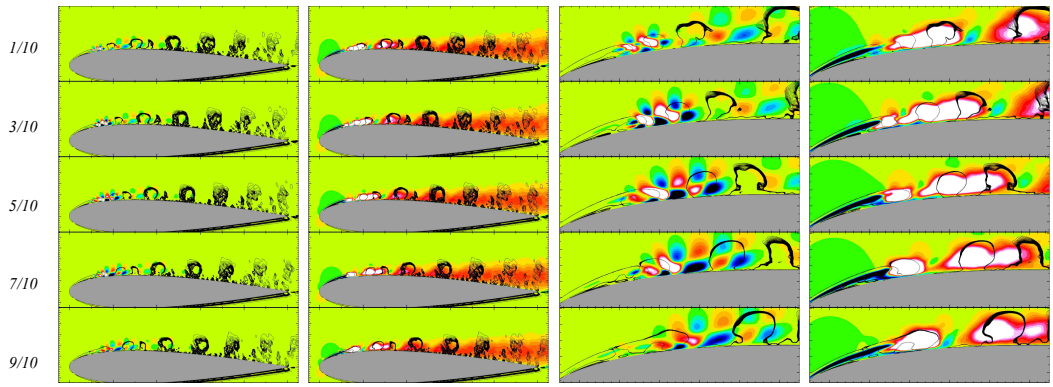

(b) Periodic (c) Turbulent (d) Periodic (e) Turbulent

Fig. 4.25: Coherent vortex structures and Reynolds shear stress: $C_\mu = 2.0 \times 10^{-5}, F^+ = 6.0$ case

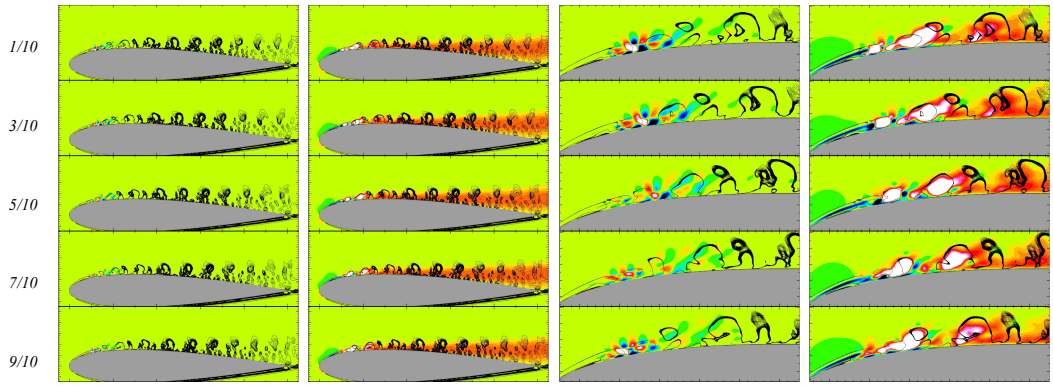

(b) Periodic (c) Turbulent (d) Periodic (e) Turbulent

Fig. 4.26: Coherent vortex structures and Reynolds shear stress: $C_\mu = 2.0 \times 10^{-5}, F^+ = 10$ case

4.6.2 Generation of the coherent vortex

In this subsection, the generation of the coherent vortex is discussed for the strong input case with $F^+ = 6.0$. Figure 4.27 shows the space-time combined system for a visualization of coherent vortex motion and turbulent component of the Reynolds shear stress. The φ-axis indicates the phase angle based on $F^+ = 6.0$ for $0 \leq \varphi \leq 8\pi$ (4 period), and the x/c_h-axis indicates the spatial chordwise direction. At each phase, the phase- and span-averaged flow fields are visualized, where the isosurface shows the second invariant of the velocity gradient tensor. Therefore, the isosurface in Fig. 4.27 shows the convection of vortex structures which are illustrated by black contours at each phase in Fig.4.22. The isosurface is colored by the turbulent component of the Reynolds shear stress, $-\langle u''w'' \rangle_\varphi$.

In Fig 4.27(a), the separation bubble expands during $\varphi = \pi$ to 2π, from which the small vortex structures are emitted at $\varphi = 2\pi$ to 3π. Each small vortex structures are convecting downstream, and two of them are merging at $x/c_h \simeq 0.25$ and $\varphi \simeq 4\pi$, which generates the strong coherent vortex. The resultant coherent vortex remains strong further downstream, which is emitted periodically from the trailing edge. The other small vortex structures are gradually diffused as convecting downstream.

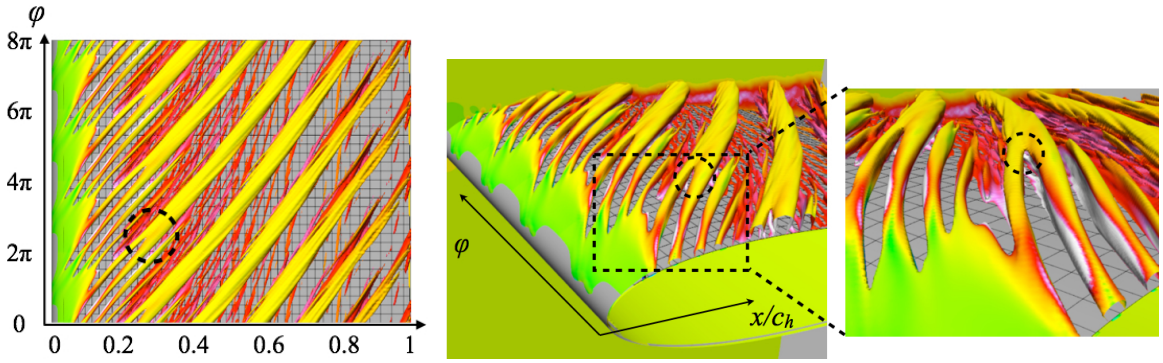

(a) Vertical view (b) Perspective view

Fig. 4.27: Coherent vortex structures and Reynolds shear stress: $C_\mu = 2.0 \times 10^{-3}, F^+ = 6.0$ case

4.7 Summary

The effect of the actuation frequency on the capabilities of separation control is discussed, and the mechanism of the separation control is investigated mainly from the viewpoint of a chordwise momentum exchange by the Reynolds shear stress.

Chapter 5

Spatial development of the disturbances from the synthetic jet

5.1 Outline

5.2 Case description

In this chapter, the mechanism of spatial development of disturbances from the SJ is investigated in the separation controlled flows. In particular, the case with an optimal frequencies for the SJ capability is discussed. The cases shown in this chapter are as follows:

Table 5.1: Computational cases. The synthetic jet is installed at the leading edge of the airfoil.

case name	input momentum (C_μ)	F^+
Off controlled/separated (AoA=12[deg.])	—	—
Off controlled/attached (AoA=10[deg.])	—	—
strong input (AoA=12[deg.])	2.0×10^{-3}	1.0, 6.0, 10
weak input (AoA=12[deg.])	2.0×10^{-5}	1.0, 6.0, 10

In this chapter, the noncontrolled case of $AoA = 10$ [deg.] is additionally discussed based on the following reasons: the flow at $AoA = 10$ [deg.] is attached with a laminar

separation bubble near the leading edge; the spatial development of disturbances on the separation bubble is an important issue for the separation control mechanism in the present flow/actuator conditions.

The wall-normal fluctuation in the separated shear layer is focused for the discussion on the spatial development of disturbances.

5.3 Noncontrolled cases

In this section, the spatial development of disturbances in the noncontrolled cases of $AoA = 12°$ and $10°$ is discussed. The case of $AoA = 12°$ exhibits the flow separation at 2.5% of the chord length, which is the baseline case for the separation control in this study. In the case of $AoA = 10°$, the flow is separated at 2.5% of the chord length and reattached at 2.5% with a laminer separation bubble. The details of noncontrolled cases are described in Sec.**??**.

5.3.1 Spatial growth rate

According to Sec.**??**, the spatial growth rate of wall-normal fluctuation is compared between LST and LES results. Here again, the notation of LST indicates "linear stability theory", and the spatial growth rate α_i is estimated from the eigen value problem in Eq.**??**, where the time-averaged wall-tangential velocity profiles are used. The LES indicates the α_i based on the PSD of wall-normal fluctuation in Eq.**??**, where FFT is conducted on the unsteady data of the LES data.

Separated flow case ($AoA = 12°$)

Figure 5.1 shows the comparison of sptial growth rate α_i for LST and LES results. In each cases, the top contour figure shows the chordwise velocity of time-averaged fields, and the bottom three figures show the α_i distribution for St at different x/c_h position. The black dots in α_i distributions show the FFT results of LES data at three different grid points near each x/c_h position on the TKE-max line (see Sec.**??**); on the other hand, the red solid lines show the LST results based on the time-averaged wall-tangential velocity profile. In each α_i plots, the smaller α_i (i.e., the larger $-\alpha_i$) corresponds to more unstable fluctuation

so that the St number indicating the smallest α_i is the most unstable frequency. Note that if the fluctuation follows the linear stability theory, the most unstable mode (or the frequency) can be estimated by solving the eigen value problem, where, the profile of α_i by LST (red solid line) is corresponding to that by LES data (black dots). The most unstable frequency estimated by LST is called "linear instability frequency" hereinafter.

In the case of $AoA = 12°$ (Fig.5.1(a)), the α_i profiles of LST and LES data show good agreement at $x/c_h = 8\%$ in terms of the most unstable frequency. Therefore, the fluctuation in the separated shear layer at $x/c_h = 8\%$ linearly develops as has been reported in many previous studies for the flow instability in a shear layer[][][]. In this linear growth regime, the linear instability frequency is $St \simeq 20$. At $x/c_h = 11\%$, the α_i profiles of LST and LES data are different in terms of the most unstable frequency, where the linear instability frequency is $St \simeq 15$ (red solid line), but the most unstable frequency estimated by LES data (black dots) is $St \simeq 30$ of harmonics of the linear instability frequency. In this region, the fluctuation has sufficiently developed in the upstream of $x/c_h = 11\%$ such that the linearlized approximation cannot be adopted in Eq.(**??**), and it is transient to the nonlinear growth regime. The flucutation at $x/c_h = 13\%$ is also in the nonlinear growth regime, where the linear instability frequency $St \simeq 10$ is not the most unstable frequency, but the modes in higher frequencies ($St \simeq 50$) show larger spatial growth rate $-\alpha_i$. Such larger growth rate in the higher frequency modes indicates that a turbulent transition is promoted by fine vortex structures developping downstream.

In this way, the spatial development of the fluctuation in a shear layer can be typically explained by the sequential two regimes: the first one is a linear growth regime, where the spatial development of the fluctuation can be approximated by the linearized equation, and the most unstable mode is estimated by LST; the second one is a nonlinear growth regime, where the amplitude of the fluctuation has been already saturated in more upstream region such that the most unstable mode cannot be determined by the linearlized approximation, but higher frequency modes show larger growth rate than linear instability mode. Note that the coherent vortex shedding frequency described in Sec.**??** is estimated as $St = 12$, based on which the emission of the large and coherent vortex from the separated shear layer is clearly captured in the phase-averaged flow fields (Fig.**??**(a) and Fig.**??**(a)). The frequency of $St = 12$ is slightly different from that of the linear instability mode in a linear growth regime ($St \simeq 20$ at $x/c_h = 8\%$), but is

much more close to the instability mode in the nonlinear growth regime ($St \simeq 10$ at $x/c_h = 13\%$). This is because although the $St = 12$ mode (linear instability mode) is not the most unstable at $x/c_h = 13\%$ in terms of the spatial growth rate, the amplitude of $St = 12$ mode would be further larger than that of $St \simeq 50$ (nonlinear instability modes). Therefore, the frequency of coherent vortex emission from the separated shear layer should be carefully discussed in the plot of the spatial growth rate α_i, where the linear instability frequency in the nonlinear growth regime would be corresponding to that of the coherent vortex emission if the amplitude of the linear instability mode has been sufficiently developed in the upstream region.

Laminar separation bubble case ($AoA = 10°$)

In the case of $AoA = 10°$ (Fig.5.1(b)), the α_i profiles of LST and LES data show good agreement at $x/c_h = 8\%$, where $St \simeq 20$ is the linear instability frequency. The higher frequency modes such as $St \simeq 40$ show comparable growth rate at $x/c_h = 14\%$, where the nonlinear growth regime begins. At $x/c_h = 18\%$, the linear instability frequency is $St \simeq 15$, but the higher frequency modes $St \geq 40$ show much larger growth rate. In this way, the trend of sequential transient from the linear to nonlinear growth regime of the fluctuation is similar to that of $AoA = 12°$ (separated flow) case. Similarly, the frequency of coherent vortex emission is estimated as $St \simeq 12$ from the phase-averaged flows, which is close to that of linear instability frequency in nonlinear growth regime ($x/c_h = 18$, 19, and 20%: see Sec.**??**). However, at $x/c_h = 18\%$, the α_i profiles of LST and LES results do not show a good agreement, but the LES data shows lower unstable frequency than the linear instability frequency $St \simeq 15$, i.e., the unstable frequency of LES data is $St \simeq 10$ and lower (this is more clearly observed in $x/c_h = 19$ and 20% in Sec.**??**). This would be caused by the merging procedure of coherent vortex emitted from the separated shear layer, which results in larger coherent vortex convecting downstream. Such a larger growth rate in the lower frequency mode than the linear instability mode could specifically appear in the flow with a laminer separation bubble, which is one of the distinctive characteristics in the present attached flow. Based on these investigation, hereinafter, the scenario for the spatial development of fluctuation is re-categolized into following three regime: linear growth regime, higher-nonlinear growth regime, and lower-nonlinear growth regime. The linear growth regime exhibits spatial development of the

fluctuation based on the linear instability theory; the higher-nonlinear growth regime indicates the larger growth rate in higher frequency modes than the linear instability frequency (i.e., observed in both of the $AoA = 12$ and 10° cases); the higher-nonlinear growth regime indicates the larger growth rate in lower frequency modes than the linear instability frequency (i.e., appearing only in the $AoA = 10^\circ$ case).

Figure 5.2 shows the spatial growth rate α_i on a St-x plane for $0.0 \leq x/c_h \leq 0.2$. The red lines shows the contour of α_i estimated by LST, and the black-to-white contour shows the α_i distribution evaluated by LES data.

The St-x visualization for the $AoA = 12^\circ$ case (Fig.5.2(a)) more clearly shows the linear instability regime in $2\% \leq x/c_h \leq 8\%$ where the red lines and black-to-white contours are corresponding with each other. In $8\% \leq x/c_h$, the larger growth rate α_i appears in higher frequencies, which is called higher-nonlinear instability regime in this thesis. The linear instability frequency gradually decreases due to the development of the separated shear layer as going to the downstream (the inflection point in the wall-tangential flow profile becomes farther from the airfoil surface), which is still observed even in the higher-nonlinear regime. The interesting feature is that such a linear instability frequency clearly remains further downstream ($x/c_h \simeq 20\%$) although it is not the most unstable frequency. The spatial growth rate in higher frequencies than linear instability frequency becomes large at $8\% \leq x/c_h$, where it rapidlly spreads from $St \simeq 30$ to 100 for $8\% \leq x/c_h \leq 15\%$. This indicates that the nonlinear interaction between fluctuations of multiple frequencies occurs rapidlly so that the spatial growth of higher frequency modes are promoted faster than the linear instability modes.

Figure 5.2(b) shows the case of $AoA = 10^\circ$. Similar to the case of $AoA = 12^\circ$, the linear instability regime and higher-nonlinear instability regime clearly appear at $5\% \leq x/c_h \leq 13\%$ and $13\% \leq x/c_h$, respectively. On the other hand, the spatial growth rate in lower frequencies ($St \leq 10$) becomes larger than linear instability frequency at $15\% \leq x/c_h$, which is called lower-nonlinear instability regime. Note that the large growth rate near the leading edge at $St \simeq 10$ would be related to the linear instability mode based on a visousity effect (eigen mode of the Orr-sommerfelt equation), which cannot be validated here and would not be a dominant effect in the separation control viewpoint.

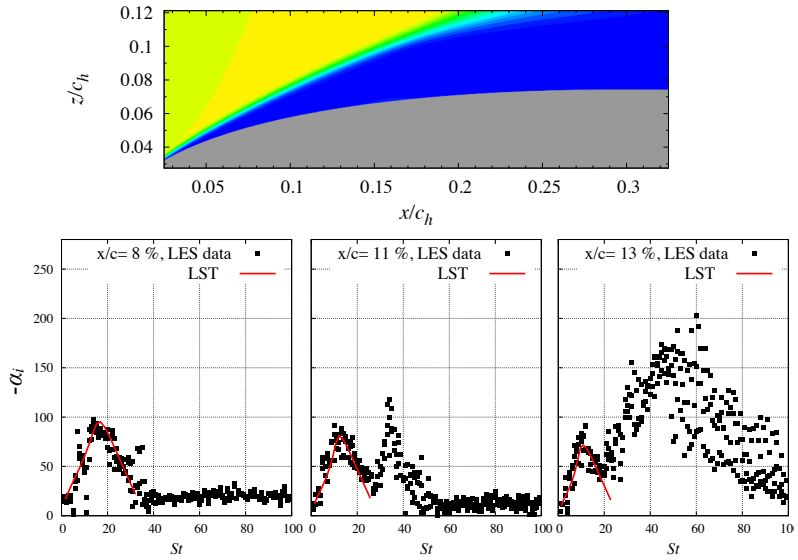

(a) $AoA = 12°$

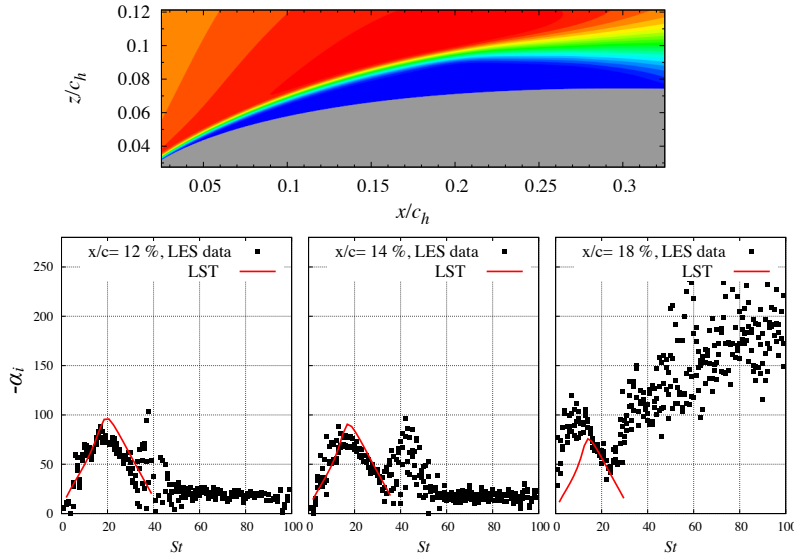

(b) $AoA = 10°$

Fig. 5.1: Control off cases: top figure shows time-averaged u/u_∞; bottom figures show the spatial growth rate α_i estimated by LST and FFT analysis for LES data.

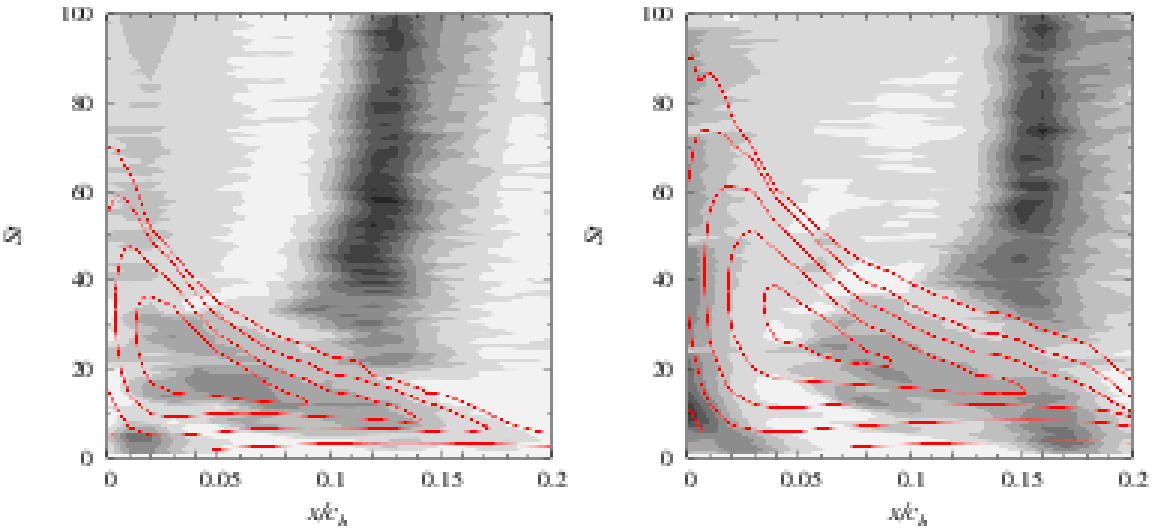

(a) $AoA = 12°$ (b) $AoA = 10°$

Fig. 5.2: Control off cases: spatial distributions of α_i; black-to-white contour and red contour lines show LES and LST results, respectively ($0 \leq -\alpha_i \leq 100$).

5.3.2 Spatial development of the PSD of wall-normal fluctuation

Figure 5.3 shows the spatial development of the PSD of wall-normal fluctuation for each cases. In the case of $AoA = 12°$, the low frequency $St = O(1)$ is larger near the leading edge, but the higher frequency mode $St \simeq 15$ is more rapidlly developing at $2\% \leq x/c_h \leq 10\%$. The spatial distribution of each freqency modes are more clearly observed in Fig.5.4(a) in St-x plane. This is a linear growth regime, where the sptial growth rate of linear unstable frequency mode ($St \simeq 15$) is the largest. After the linear growth regime, the higher-nonlinear growth regime begins at $x/c_h \simeq 11\%$, which promotes generation of fine vortex structures and a turbulent transition. Although the higher frequency mode begins developing faster than the linear instability mode, the amplitude (energy) of linear instability mode ($St \simeq 15$) is already larger than those of higher frequency modes so that the coherent vortex structure is emitted from the separated shear layer with its frequency $St \simeq 15$ as pointed out in the previous section.

On the other hand, the laminer separation bubble case ($AoA = 10°$) shows a rapid growth of linear instability mode $St \simeq 15$ at $5\% \leq x/c_h \leq 15$, which can be regarded as a linear growth regime (see Fig.5.3(b) and Fig.5.4(b)). After this regime, the nonlin-

ear growth regime begins, and higher freqeuncy modes develops faster than the liniear instability frequency mode. As pointed out in the previous paragraph, the amplitude of the linear instability mode is much larger than the higher frequency mode even in this higher-nonlinear growth regime so that the linear instability frequency is corresponding to that of coherent vortex emission from the separation bubble. The other characteristic of this laminer separation bubble case is that the lower freqeuncy mode shows rapid growth in the nonlinear growth regime, which indicates that the vortex merging occurs and larger coherent vortex would be generated in the downstream direction. Such three growth regimes (i.e., linear, higher-nonlinear and lower-nonlinear regimes) of fluctuation are the characteristic of laminer separation bubble case.

Note that the strong PSD is observed discretely at $St = 24, 48, 72$, and 96 in Fig.5.4(b) near the leading edge ($0\% \leq x/c_h \leq 15$). This is caused by the trailing edge tone, which would maintain a feedback loop between the generation of acoustic waves from the trailing edge and the oscilation of the separation bubble (see Sec.**??**). Similar discrete peak of PSD is slightly observed also in the case of $AoA = 12°$ (Fig.5.4(a)). Although the PSD of such trailing edge tone is much stronger than the disturbances of another frequency near the leading edge, the present study does not precisely discuss the mechanism because the input frequency of the SJ (F^+) is much more dominant in the controlled cases.

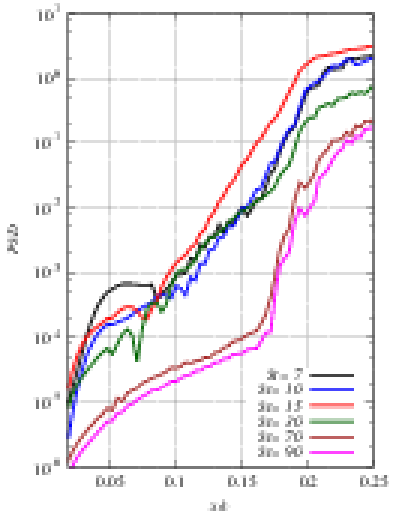

(a) $AoA = 10°$

Fig. 5.3: Control off cases: spatial distributions of α_i; black-to-white contour and red contour lines show LES and LST results, respectively ($0 \leq -\alpha_i \leq 100$).

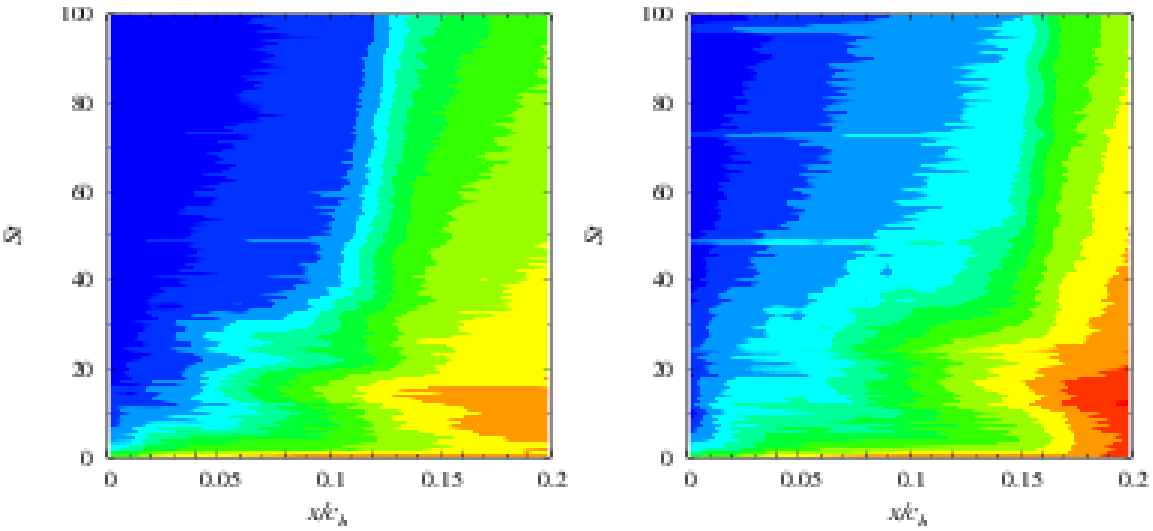

(a) $AoA = 12°$ (b) $AoA = 10°$

Fig. 5.4: Control off cases: spatial distributions of α_i; black-to-white contour and red contour lines show LES and LST results, respectively ($0 \leq -\alpha_i \leq 100$).

5.4 Separation controlled cases

In this section, the spatial development of disturbances in the separation controlled cases are discussed. The spatial growth rate and development of the PSD of wall-normal fluctuation is compared with noncontrolled cases.

5.4.1 Spatial growth rate

The spatial growth rate of wall-normal fluctuation is compared between LST and LES results. In the case of a strong input case with $F^+ = 1.0$ (Fig.5.5(a)), the α_i profiles of LST and LES data show good agreement at $x/c_h = 3\%$ in terms of the most unstable frequency $St \simeq 35$. Therefore, the fluctuation in this region linearly develops, which is called the linear instability regime. At $x/c_h = 6\%$, the linear instability frequency is $St \simeq 30$ (red solid line), but the most unstable frequency estimated by LES data (black dots) is $St \geq 60$. In this region, the spatial development of fluctuation is in the higher-nonlinear instability regime. At $x/c_h = 7\%$, the growth rate of lower frequencies is larger than that of the linear instability frequency, which is the lower-nonlinear growth regime as well as the higher-nonlinear one. Similar trend is observed in the case with $F^+ = 6.0$ and 10 (Figs.5.5), where the linear growth, lower- and higher-nonlinear growth regimes appear. These regimes from linear to nonlinear development of fluctuation are observed in a laminer separation bubble case without contorl (Figs.**??** and **??** for $AOA = 10^\circ$ case). One of the important point here is that the linear instability frequency clearly appears near the leading edge even when the periodic fluctuation is introduced from the SJ for separation control. The linear instability frequency in the linear growth regime ($x/c_h \simeq 3\%$) is $St = 30$ to 40 for $F^+ = 1.0, 6.0$, and 10 cases (see bottom left figure in Fig.5.7), which are different from that of input frequency by SJ.

In the case of a weak input case with $F^+ = 1.0$ (Fig.5.6(a)), the attached flow is not obtained, where the α_i profiles of LST and LES data show good agreement at $x/c_h = 8\%$. The growth rate in higher frequencies than linear instability frequency is larger in $x/c_h = 11$ and 13%, which are similarly observed in the noncontrolled case at $AoA = 12^\circ$ in Fig.5.1(a). The other controlled cases with $F^+ = 6.0$ and 10 show good agreement for LST and LES data near the leading edge. In the downstream region, the growth rate of higher and lower frequencies become larger than that of linear instability

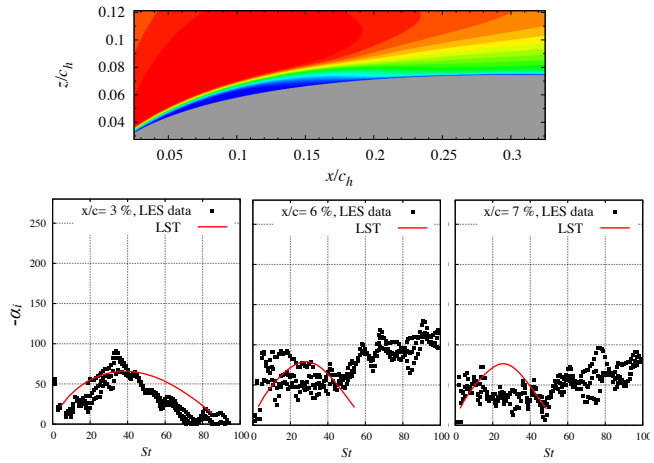

(a) $C_\mu = 2.0 \times 10^{-3}, F^+ = 1.0$

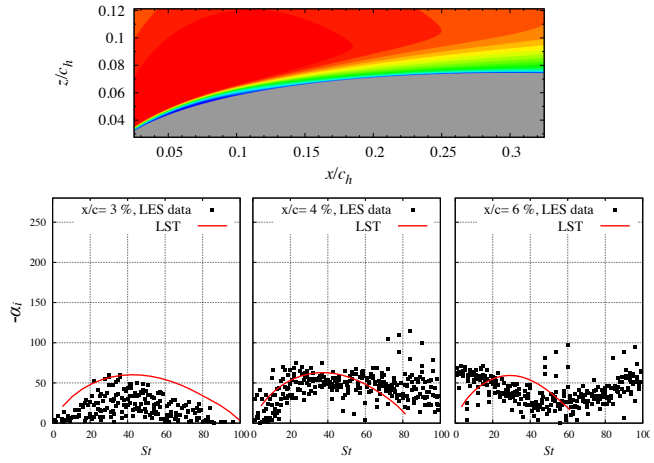

(b) $C_\mu = 2.0 \times 10^{-3}, F^+ = 6.0$

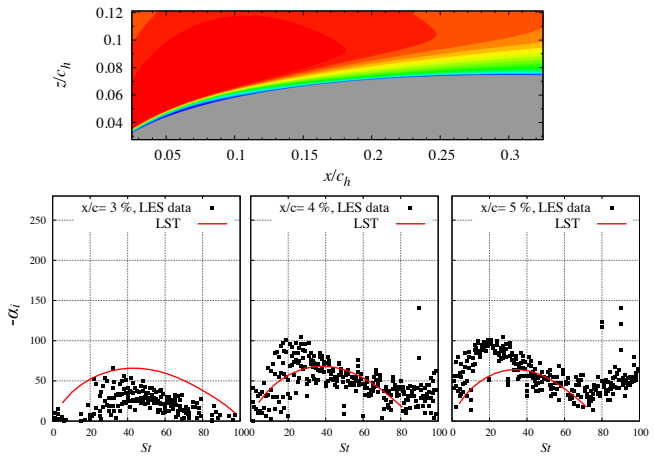

(c) $C_\mu = 2.0 \times 10^{-3}, F^+ = 6.0$

Fig. 5.5: Control off cases: top figure shows time-averaged u/u_∞; bottom figures show the spatial growth rate α_i estimated by LST and FFT analysis for LES data.

frequency. This trend is observed in noncontrolled case with a laminer separation bubble and the controlled cases with a strong input, where the linear growth, higher- and lower-nonlinear growth regime appear.

Figures 5.7 and 5.8 show the spatial growth rate α_i on a St-x plane for $0.0 \leq x/c_h \leq 0.2$. The St-x visualization for the $AoA = 12^\circ$ case (Fig.5.7) more clearly shows the linear instability regime in $2\% \leq x/c_h \leq 5\%$ where the red lines and black-to-white contours are corresponding with each other. The spatial growth rate in higher frequencies than linear instability frequency becomes large at $x/c_h \simeq 5\%$, where the mode at $St \geq 50$ rapidlly spreads. At the same position, the growth rate of lower frequencies is larger as discussed in the previous paragraph. This would be related to the vortex merging, which generates the large coherent vortex with its period F^+. The similar feature is observed in the case with $F^+ = 6.0$ and 10 in Figs.5.7(b) and (c). The another important point is that in the case with $F^+ = 6.0$ and 10, the growth rate of the actuation frequency and its harmonics (Fig.5.7(b) and (c)) is smaller than other frequencies, i.e., white horizontal stripes appear in each figures. This indicates that the flucutuations with the actuation frequency and its harmonics are strongly introduced by the SJ so that their amplitudes are almost saturated to develop in the downstream. The controllable cases with a weak input ($C_\mu = 2.0 \times 10^{-5}$: Fig.5.8(b) and (c)) show the growth rate similar to the strong input cases, where the linear, higher-nonlinear, and lower-nonlinear growth regimes appear although their values are almost twice the larger than those of strong input cases because of weaker the input fluctuation. The discrete weak growth ratio in the actuation frequency and its harmonics (appearing as white horizontal stripes in each figures) are similarly observed.

5.4.2 Validation of the linear growth regime in the controlled flows

In this part, the spatial developing mode (eigen mode) is compared in LST and LES data in order to validate the linear growth regime in controlled cases. First, the spatial developing mode $\tilde{u}'_n(x_w, z_w)$ is estimated by LST result for a certain St number (called St_{target} hereinafter):

$$\tilde{u}'_n(x_w, z_w) = \hat{u}'_n(z_w) \exp\left[i \int_0^{x_w} \alpha(x'_w) dx'_w \right]. \tag{5.1}$$

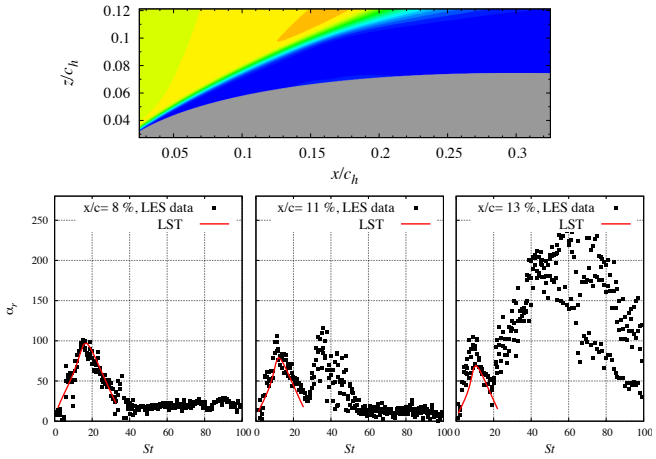

(a) $C_\mu = 2.0 \times 10^{-5}, F^+ = 1.0$

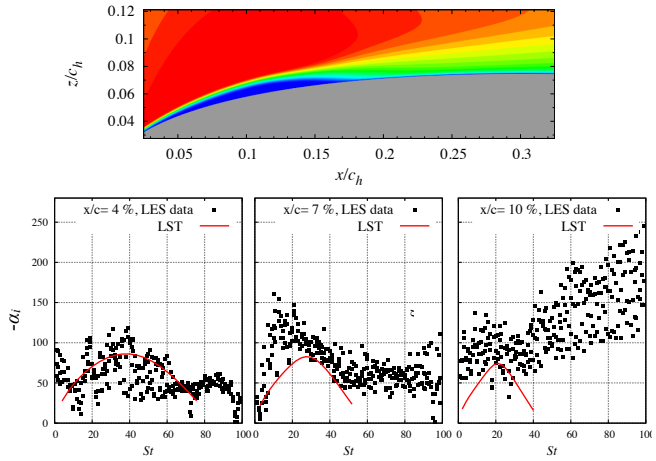

(b) $C_\mu = 2.0 \times 10^{-5}, F^+ = 6.0$

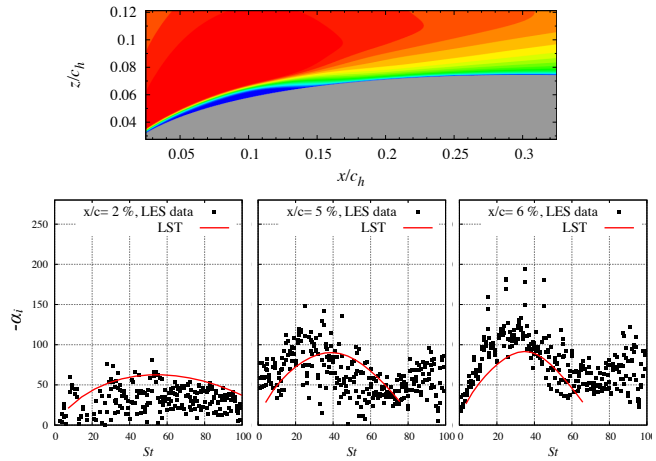

(c) $C_\mu = 2.0 \times 10^{-5}, F^+ = 6.0$

Fig. 5.6: Control off cases: top figure shows time-averaged u/u_∞; bottom figures show the spatial growth rate α_i estimated by LST and FFT analysis for LES data.

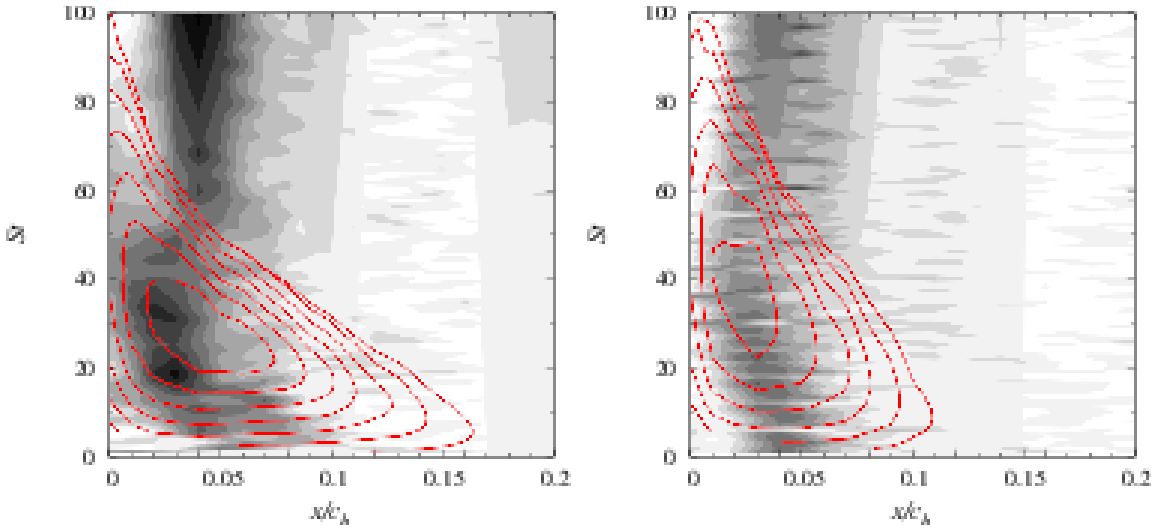

(a) $C_\mu = 2.0 \times 10^{-3}, F^+ = 1.0$ (b) $C_\mu = 2.0 \times 10^{-3}, F^+ = 6.0$

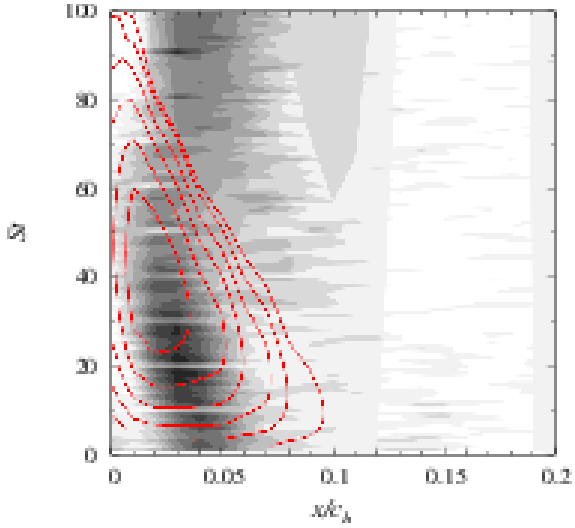

(c) $C_\mu = 2.0 \times 10^{-3}, F^+ = 10$

Fig. 5.7: $C_\mu = 2.0 \times 10^{-3}$ cases: spatial distributions of α_i; black-to-white contour and red contour lines show LES and LST results, respectively ($0 \leq -\alpha_i \leq 50$).

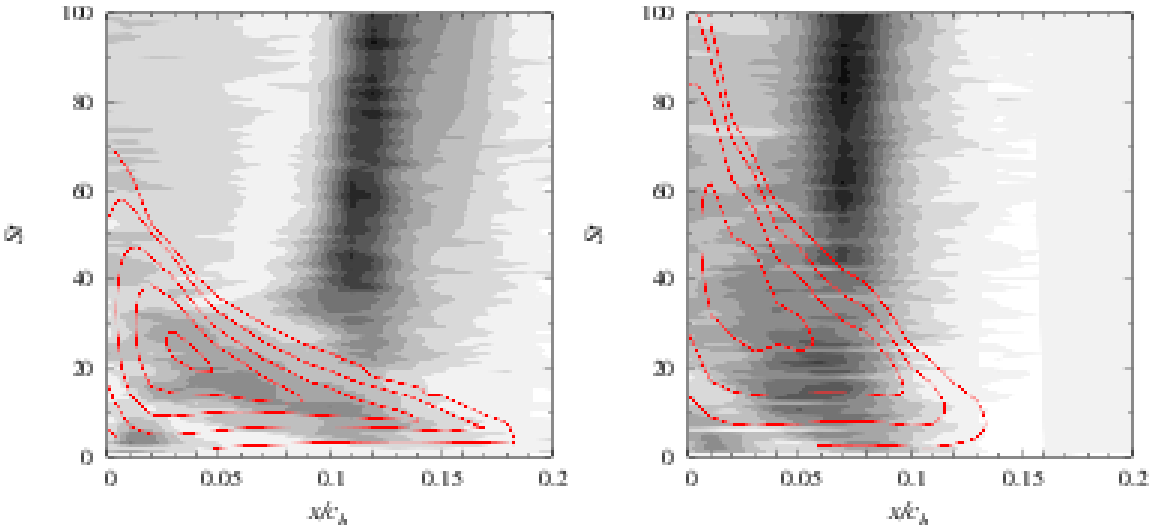

(a) $C_\mu = 2.0 \times 10^{-5}, F^+ = 1.0$ (b) $C_\mu = 2.0 \times 10^{-5}, F^+ = 6.0$

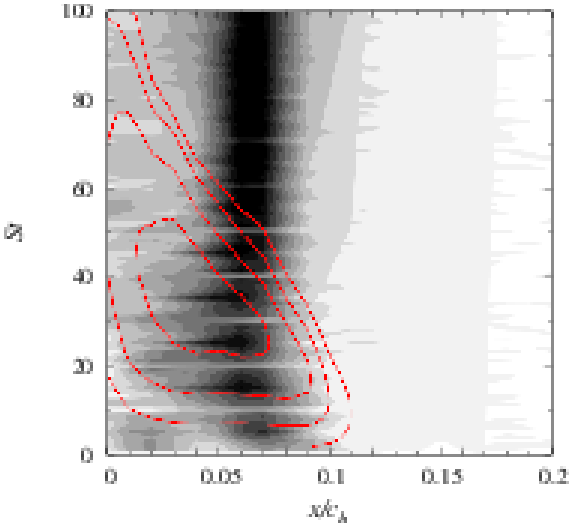

(c) $C_\mu = 2.0 \times 10^{-5}, F^+ = 10$

Fig. 5.8: $C_\mu = 2.0 \times 10^{-3}$ cases: spatial distributions of α_i; black-to-white contour and red contour lines show LES and LST results, respectively ($0 \leq -\alpha_i \leq 50$).

The unstable mode $\hat{u}'_n$ is normalized by its maximum value. The line integral for x_w in Eq.(5.1) is conducted along the airfoil surface. On the other hand, the DFT is conducted for wall-normal fluctuation to extract the spatial developing mode from the LES data. For the DFT analysis, four period of F^+ is taken from the beginning of each phases, where the flow is assumed to be periodic for F^+. The phase average of a real part is $\tilde{u}'_n$ obtained from the LES data. Figure 5.9 shows the spatial developping mode in the four controlled cases discussed in the previous part. Each modes are illustrated by white-to-black contour, and the red contour lines show the instantaneous shear layer (isosurface of a second invariant of the velocity gradient tensor). Note that in the strong input cases ($C_\mu = 2.0 \times 10^{-3}$), the St_{target} is selected as $St_{\text{target}} = 40$ for $F^+ = 1.0$ and $St_{\text{target}} = 36.92$ for $F^+ = 10$; and in the weak input cases ($C_\mu = 2.0 \times 10^{-5}$), the St_{target} is selected as $St_{\text{target}} = 33.85$ for $F^+ = 6.0$ and $St_{\text{target}} = 43.08$ for $F^+ = 10$. These are the linear instability frequencies in linear growth regime. The results of LST and DFT show qualitatively good agreement, which validate the linear growth regime near the leading edge. However, the spatial wave number is slightly higher in LST than DFT result (the wave length is smaller), which would be caused by the approximation of parallel flow and neglegting the curvature and pressure gradient in the streamwise direction in the LST.

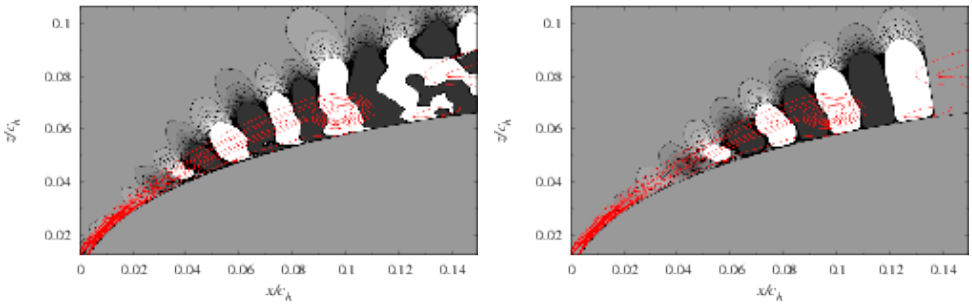

(a) DFT (CASE1) (b) LST (CASE1)

Fig. 5.9: Comparison of mode shapes (real part) for wall-normal velocity fluctuation (the range is arbitrarily set). (a) and (b) show the CASE1: $St = 40.00$ in $C_\mu = 0.2\%$ with $F^+ = 1.0$ case; (c) and (d) show the CASE2: $St = 36.92$ in $C_\mu = 0.2\%$ with $F^+ = 10$ case; (e) and (f) show the CASE3: $St = 33.85$ in $C_\mu = 0.002\%$ with $F^+ = 6.0$ case; (g) and (h) show the CASE4: $St = 43.08$ in $C_\mu = 0.002\%$ with $F^+ = 10$ case. Red contour lines show the instantaneous Q-invariant values.

5.4.3 Spatial development of the PSD of wall-normal fluctuation

Figure **??**(a) shows the spatial development of the PSD of a strong input case with $F^+ = 1.0$. The modes at linear instability frequency $St \simeq 40$ is smaller than input frequency mode ($St = 1.0$), nevertheless it is rapidlly developping in the downstream direction up to $x/c_h \leq 5\%$ and its PSD almost overcomes the other modes. This is corresponding to the linear growth regime. On the other hand, the higer frequency modes such as $St = 70$ and 80 show smaller PSD than another frequency modes at the leading edge, which begin developping after the sufficient growth of the linear instability modes ($5\% \leq x/c_h$). The PSD of $St = 1.0$, which is the actuation frequency $F^+ = 1.0$, is the largest at the leading edge since its fluctuation is directly introduced by the SJ. The PSD of $St = 1.0$ develops rapidly at $0\% \leq x/c_h \leq 5\%$, and it maintains strong further downstream. This promotes lower frequency modes than linear instability frequency at the downstream position, i.e., lower-nonllinear growth regime, which contribute to generating the coherent vortex with its period corresponding to the actuation frequency. For example, the lower frequency mode such as $St = 5.0$ is weaker near the leading edge, which the linear instability modes overcomes at $x/c_h \simeq 5\%$ although the initial PSD of $St = 5.0$ is stronger due to the harmonics of the input frequency. Then, after the linear instability modes sufficiently developping, i.e., after the linear growth regime, the lower frequency mode $St = 5.0$ rapidlly develops. The sequence of spatial growth regime is more clearly seen in the St-x visualization in Fig.5.11(a). In addition, this is seen in the case without control for a laminer separation bubble (Fig.5.3(b) and Fig.5.4(b)), but the input frequency $F^+ = 1.0$ would promote the spatial development of this lower frequency mode. In this way, the important point is that even in the controlled case, the fluctuation with a linear instability frequency is developping initially, then the other higher-nonlinear and lower-nonlinear instability modes are enhanced, which are related to the promotion of turbulent transition and generation of large coherent vortex structures, respectively. Specifically, the lower-nonlinear instability modes would be promoted by the input frequency (which is generally much lower than the linear instability frequency), i.e., $St = 1.0$ in the case of this paragraph. The better seprartion control would be realized by the smooth and quick transition from linear to higher- and lower-nonlinear growth

regime, which causes the difference of capabilities for separation control with $F^+ = 1.0$ and 6.0 or higher frequencies as discussed below.

The cases of strong input $C_\mu = 2.0 \times 10^{-3}$ with higher actuation frequencies such as $F^+ = 6.0$ and 10 are shown in Figs.**??**(b) and (c). In these cases, the trangient sequence of a spatial growth ratio is almost similar to that of the case with $F^+ = 1.0$ in the previous paragraph. However, the gap of the initial PSD (at the leading edge: $x/c_h = 0\%$) between the linear instability frequency and input frequency is much smaller than the $F^+ = 1.0$ case: in other words, the initial PSD of linear instability frequency is further larger. For example in the case with $F^+ = 6.0$ (Fig.5.11(b)), the initial PSD of $St = 40$ of Fig.5.11(b) is much larger than $St = 27$ of Fig.5.11(a) (this is close to the linear instability frequency in the case with $F^+ = 1.0$) at the leading edge. This is caused by the smaller gap of frequencies between input and linear instability modes in the $F^+ = 6.0$ case than the $F^+ = 1.0$ case. The smaller gap between the actuation frequency and linear instability frequency results in the higher PSD of linear instability modes because the SJ introduces not only the fluctuation with the actuation frequency F^+ but also its harmonic modes. For this reason, the initial PSD of linear instability frequency is much larger than the case with $F^+ = 1.0$, which contributes to the quick and smooth transition to the higher- and lower-nonlinear growth regime. Therefore, the turbulent transition occurs in more upstream position in the case with $F^+ = 6.0$ and 10 than the $F^+ = 1.0$ case, and the size of a separation bubble becomes smaller. The other important fact is that the enhancement of lower frequency mode would be enhanced by the actuation frequency mode, i.e., $F^+ = 6.0$ and 10, which promote the generation of large coherent vortex structures in the downstream direction. Such coherent vortex structure is significant in terms of chordwise momentum exchange as well as the turbulent vortex structure as discussed in Sec.**??**. Therefore, the case without promotion of such lower frequency mode cannot effectively suppress the separation, e.g., the $F^+ = 40$ case of strong and weak inputs although it directly introduces higher PSD of the linear instability frequency. The St-x visualization in Fig.5.11(b) and (c) supports the present discussion more clearly, where the higher PSD of the linear instability frequency appears at $0\% \leq x/c_h \leq 5\%$ and the discrete higher PSD region appears at the actuation frequency F^+ and its harmonics.

In the controllable cases with a weak input: $C_\mu = 2.0 \times 10^{-5}, F^+ = 6.0$ and 10 (Figs.5.12(b) and (c)), the similar trend appears. In each cases, the fluctuation at linear

instability frequencies $St = 36$ and 42 develops first, then the higher frequency ($St = 70$ and 80) and lower frequency ($St = 6$ and 10) begins developping in the downstream direction. On the other hand, the amplitude of the fluctuation from the SJ is smaller in these weak input cases than strong input cases. Therefore, the end of a linear growth regime is located at more downstream position, where the longer distance is required for the linear instability mode to sufficiently develop. This follows that the position of a turbulent transition is located at more downstream and the size of a separation bubble becomes larger than strong input cases. However, for example in the case with $F^+ = 1.0$, the fluctuation cannot develop suffciently so that the separated flow is not suppressed.

To summarize, the important points for the effective separation control are the smooth and quick growth of higher and lower frequency modes, which contribute to the turbulent transition and generating the coherent vortex structures. In order to enhance these higher and lower nonlinear growth, the linear instability mode should be effectively developped first. Therefore, when the fluctuation of linear instability frequency ($St = 30$ to 40) is strongly introduced as a harmonics of actuation frequency, the turbulent transition more quickly occurs and the size of a separation bubble becomes smaller. In the present cases, it is more clearly observed in the case with $F^+ = 6.0$ and 10 than $F^+ = 1.0$; and the case with a strong input $C_\mu = 2.0 \times 10^{-3}$ than the weak input cases $C_\mu = 2.0 \times 10^{-5}$. Note that when the fluctuation of a linear instability frequency is directly introduced from the SJ (e.g., the case with $F^+ = 40$), the better capability cannot be achieved than lower input frequency (e.g., $F^+ = 6.0$ and 10) cases because of the lack of promoting lower frequency mode.

5.5 Summary

In sumamry, the following three items are important for the better separation control:

a

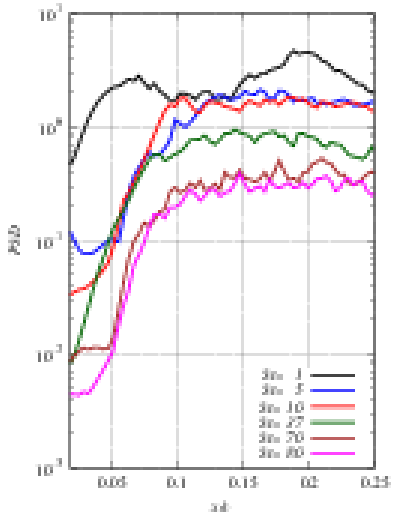

(a) $C_\mu = 2.0 \times 10^{-3}, F^+ = 1.0$

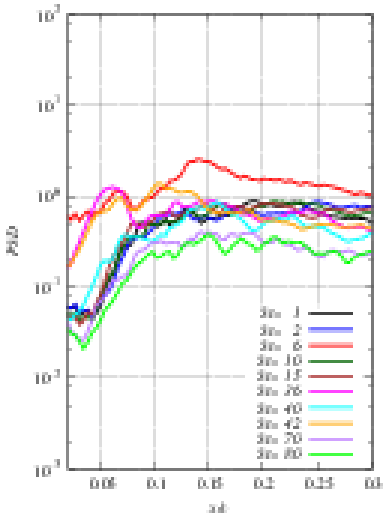

(b) $C_\mu = 2.0 \times 10^{-3}, F^+ = 6.0$

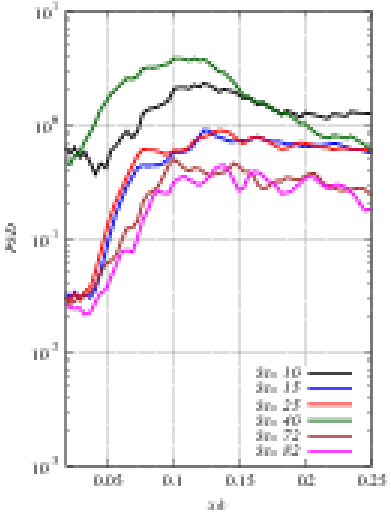

(c) $C_\mu = 2.0 \times 10^{-3}, F^+ = 10$

Fig. 5.10: Control off cases: spatial distributions of α_i; black-to-white contour and red contour lines show LES and LST results, respectively ($0 \leq -\alpha_i \leq 100$).

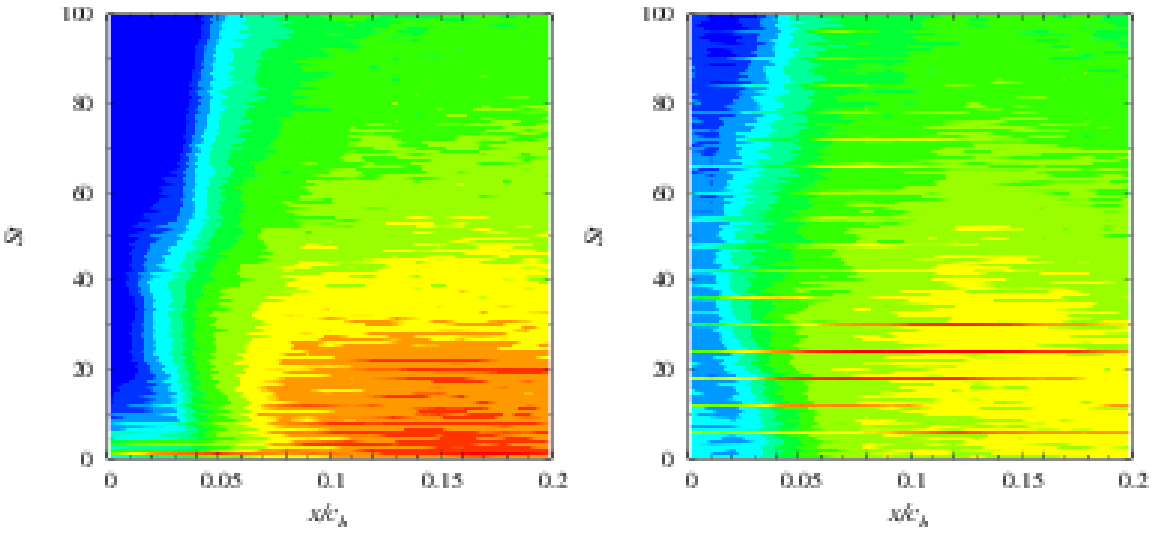

(a) $C_\mu = 2.0 \times 10^{-3}, F^+ = 1.0$ (b) $C_\mu = 2.0 \times 10^{-3}, F^+ = 6.0$

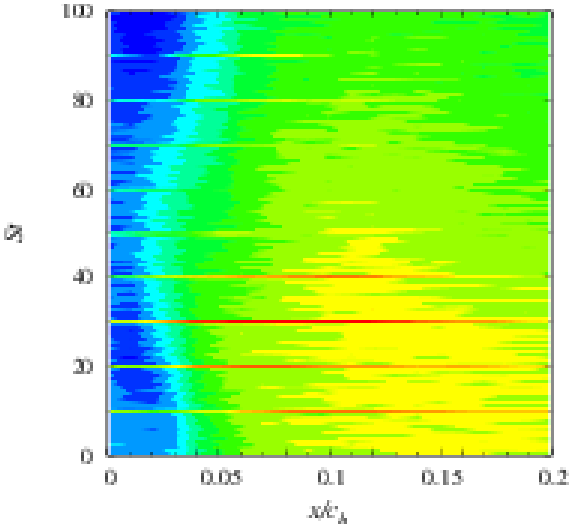

(c) $C_\mu = 2.0 \times 10^{-3}, F^+ = 10$

Fig. 5.11: Control off cases: spatial distributions of α_i; black-to-white contour and red contour lines show LES and LST results, respectively ($0 \leq -\alpha_i \leq 100$).

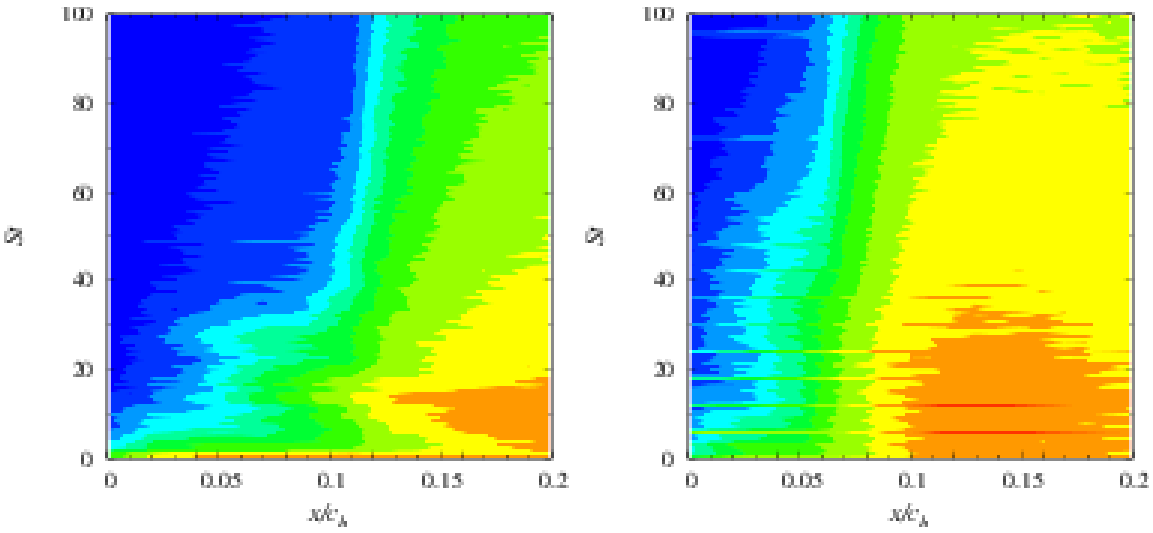

(a) $C_\mu = 2.0 \times 10^{-5}, F^+ = 1.0$ (b) $C_\mu = 2.0 \times 10^{-5}, F^+ = 6.0$

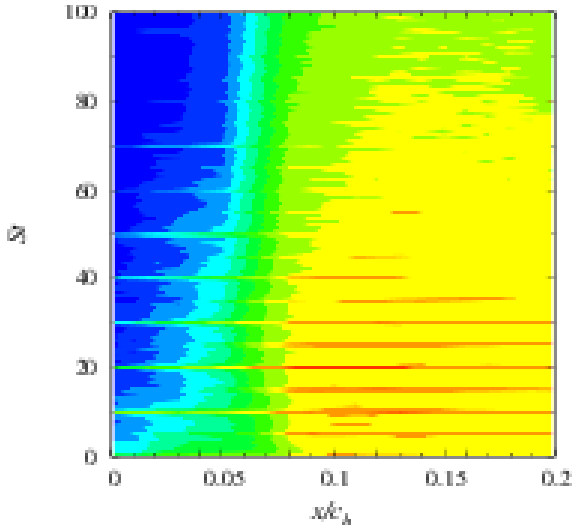

(c) $C_\mu = 2.0 \times 10^{-5}, F^+ = 10$

Fig. 5.12: Control off cases: spatial distributions of α_i; black-to-white contour and red contour lines show LES and LST results, respectively ($0 \leq -\alpha_i \leq 100$).

Chapter 6

Effects of spanwise fluctuations in the induced flow

6.1 Outline

Recently, three-dimensional unsteady analyses are getting more and more significant with regards to the physics of the separation control, focusing on turbulent structures. For example, Okada et al. performed a large-eddy simulation (LES) on the separation control over a backward facing step using a synthetic jet with a three-dimensional cavity [24] . You and Moin also conducted LES [33] on the separation control around an airfoil; the aerodynamic coefficients from the simulation corresponded well to those obtained experimentally. They also reported that the key mechanisms of separation control include not only the modification of two-dimensional boundary layer profile by adding or removing momentum in the freestream direction, but also three-dimensional turbulent mixing. More quantitatively, our recent study has shown that the turbulent structure is significant in terms of the momentum exchange based on Reynolds shear stress, and the large vortex structure appearing in phase- and spanwise-averaged flow fields specifically entrains the turbulent component of Reynolds shear stress [2] . Considering these results, we have investigated the significance of three-dimensional turbulent structures induced from the synthetic jet [3], where the synthetic jet was modeled by the deforming cavity (Cavity model) and two-dimensional jet profile of the boundary condition (Bc model), and the controlled flows were compared. The instantaneous and time-averaged flow fields

of the Bc model are significantly different from those of the Cavity model, where the turbulent transition occurs near the leading edge in the Cavity model, but near the trailing edge in the Bc model. In this way, three-dimensional turbulent structures inside the cavity is found important in terms of the turbulent transition in the controlled flow, which contributes to an enhancement of turbulent mixing and improvement in aerodynamic coefficients. Similar trend has been reported in the separation control using the dielectric barrier discharge (DBD) plasma actuator where the body force is distributed in a spanwise intermittent layout [15] . However, the key three-dimensional structure (spanwise disturbance) in the induced flow and its spatial development interacting with the turbulent boundary layer was not discussed in details.

In this study, the spatial growth of the spanwise disturbance induced by a synthetic jet is investigated on separated-flow control around NACA0015 (Re=$63,000$ and $AOA = 12.0°$) using LES. The synthetic jet is installed at a leading edge which is numerically modeled by a three-dimensional deforming cavity: "Cavity model"; and an artificial jet profile for a boundary condition: "Bc model". The jet profile of the Bc model is sinusoidally oscillated in a spanwise direction with a wave number from $k_{y\mathrm{in}}/2\pi = 0$ to 95. Using these models, the following three topics are focused: 1) using the Cavity model, the spanwise Fourier modes of the induced jet and their spatial growth in the controlled flow field are investigated; 2) the aerodynamic performances are compared among the Bc models with $k_{y\mathrm{in}}/2\pi = 0$ to 95; 3) the turbulent transition and the spatial growth of spanwise Fourier modes are discussed when the spanwise disturbance of the Bc model is based on the most amplified mode in the Cavity model.

6.2 Case description

The computational cases are arranged in Table 6.1. In this study, the momentum coefficient C_μ is set to 0.2% which is smaller than that used in the previous study [33] ; the actuation frequency is set to $F^+ = 6.0$; the synthetic jet is installed to the leading edge. The actuation frequency $F^+ = 6.0$ shows the better aerodynamic performances compared to the other frequencies [3],[2] . The spanwise wave number $k_{y\mathrm{in}}/2\pi$ is varied for $0 \leq k_{y\mathrm{in}}/2\pi \leq 95$.

Table 6.1: Computational cases

Spanwise wave number ($k_{y\mathrm{in}}/2\pi$)	Synthetic jet is modeled by
—	deforming cavity
0	boundary condition
10	boundary condition
30	boundary condition
95	boundary condition

† C_μ is set to 2.0×10^{-3}; synthetic jet is installed at the leading edge; actuation frequency is set to $F^+ = 6.0$.

6.3 Aerodynamic performances

Table 6.2 and Fig. 6.1 show the time-averaged aerodynamic coefficients for $20 \leq tu_\infty/c_h \leq 28$. In Fig. 6.1, the black broken line shows the coefficients of Cavity model, and the red one shows those of Bc model with spanwise wave number from $k_{y\mathrm{in}}/2\pi = 0$ to 95. All the controlled cases attain the lift enhancement and drag reduction which indicate a stall recovery. The two-dimensional Bc model ($k_{y\mathrm{in}}/2\pi = 0$) shows less C_L and higher C_D than the Cavity model, and the resultant lift-drag ratio is worse than the Cavity model. Similar trend has been reported in our previous study [3] although its two-dimensional jet profile was assumed to be parabolic shape unlike the present study. Therefore, the difference between parabolic and prescribed (using phase- and span-averaged jet profile of the Cavity model) jet profile for Bc model without three-dimensional disturbances would not significantly affect the qualitative trend in the aerodynamic performances in the present flow conditions. On the other hand, all the cases with a three-dimensional jet profile for Bc model ($k_{y\mathrm{in}}/2\pi = 10, 30$, and 95) show higher C_L and lower C_D than the case with the two-dimensional jet profile, which indicates that the three-dimensional (spanwise) disturbance enhances the aerodynamic performance as suggested in our previous study [3] . However, the trend of C_L and C_D variance is not monotonic with respect to $k_{y\mathrm{in}}$ in the Bc models; e.g., C_D is most reduced at $k_{y\mathrm{in}}/2\pi = 30$, and C_L is most recovered at $k_{y\mathrm{in}}/2\pi = 10$. These results indicate that some optimal $k_{y\mathrm{in}}$ would exist in terms of higher C_L and lower C_D in the present flow condition and parameters of the synthetic jet, which will be discussed in Sec.6.4.2 and 6.5.1 in detail.

Table 6.2: Time averaged C_L and C_D values in $20 \leq tu_\infty/c_h \leq 28$. C_{Dp} and C_{Df} indicate the pressure and frictional drag, respectively.

CASE	C_L	C_D	C_L/C_D	C_{Dp}	C_{Df}
Off control	0.427	0.151	2.82	0.1435	0.007644
Cavity model	1.10	0.0669	16.4	0.05417	0.01272
Bc model ($k_{yin}/2\pi = 0$)	1.03	0.0712	14.5	0.06039	0.01032
Bc model ($k_{yin}/2\pi = 10$)	1.14	0.0674	17.1	0.05300	0.01375
Bc model ($k_{yin}/2\pi = 30$)	1.06	0.0656	16.1	0.05334	0.01231
Bc model ($k_{yin}/2\pi = 95$)	1.14	0.0680	16.8	0.05636	0.01162

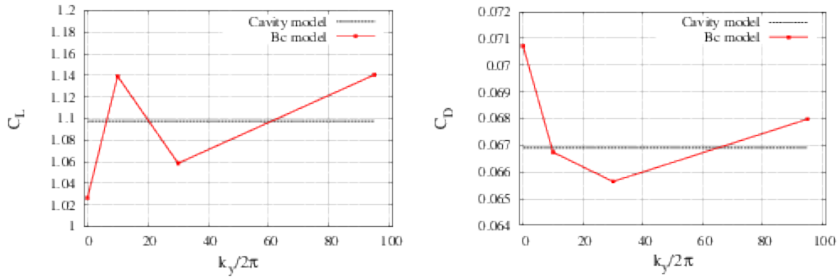

(a) Lift coefficient C_L (b) Drag coefficient C_D

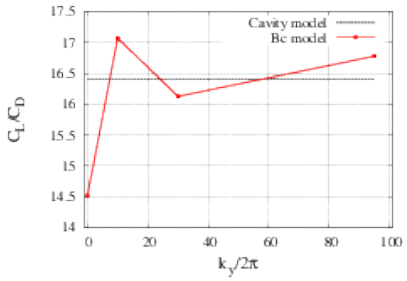

(c) Lift-drag ratio C_L/C_D

Fig. 6.1: Time average of aerodynamic coefficients.

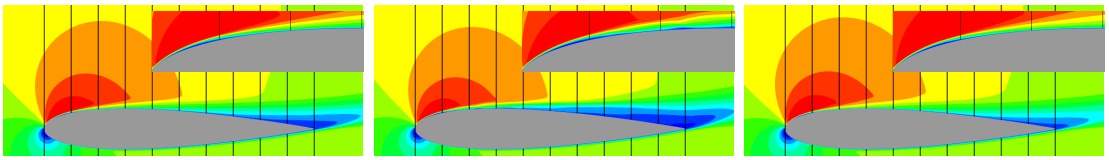

(a) Cavity model (b) $k_{yin}/2\pi = 0$ (c) $k_{yin}/2\pi = 10$

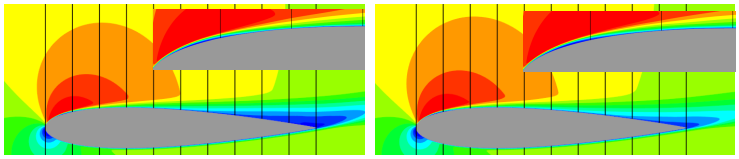

(d) $k_{yin}/2\pi = 30$ (e) $k_{yin}/2\pi = 95$

Fig. 6.2: Time-averaged chordwise velocity u/u_∞ is shown for each model; the black lines indicates the position of $x/c = 0.0, 0.1, 0.2, \ldots, 1.0$.

6.4 Flow fields and mechanism of separation control

6.4.1 Instantaneous flow fields

Figure 6.3 shows the instantaneous flow fields of controlled cases with the Cavity and Bc models. The isosurface is the second invariant of the velocity gradient tensor and is colored by the vorticity in the chord direction. The contour plane normal to the span direction shows the chordwise velocity u/u_∞. In the Cavity model case and Bc model cases with $k_{yin}/2\pi \geq 10$, a turbulent boundary layer with three-dimensional fine vortex structures is developed over the airfoil. On the other hand, the two-dimensional Bc model case ($k_{yin}/2\pi = 0$) shows two-dimensional spanwise vortex structures near the leading edge, where the turbulent transition is significantly delayed compared to other cases. Additionally, in the case with $k_{yin}/2\pi = 30$ (Fig. 6.3(d)), the coherent structures with spanwise-oscillating structure strongly remains further downstream, where the turbulent transition occurs more quickly than the other cases as will be shown in Figs. 6.5(b) and (c).

6.4.2 Time-averaged flow fields

Figure 6.2 shows time-averaged chordwise velocity fields u/u_∞, where the attached flows are observed in all the controlled cases. Each figure includes a zoom view near the leading edge, and a reversed region is observed in each case, which are more quantitatively

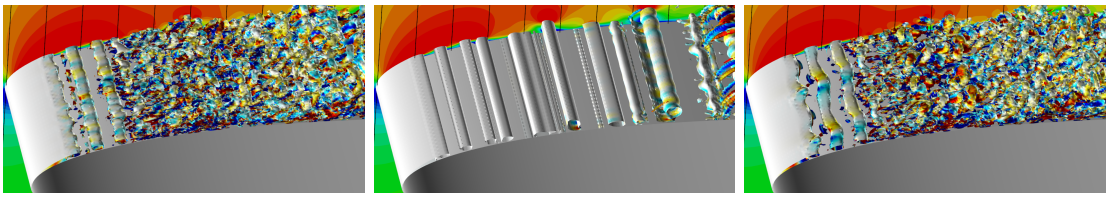

(a) Cavity model (b) $k_{yin}/2\pi = 0$ (c) $k_{yin}/2\pi = 10$

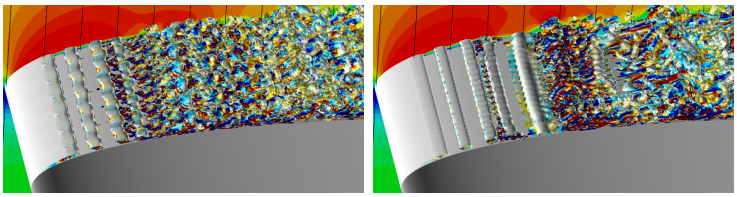

(d) $k_{yin}/2\pi = 30$ (e) $k_{yin}/2\pi = 95$

Fig. 6.3: Instantaneous flow field: x-direction velocity contour; isosurfaces of second invariant of velocity gradient tensor (colored by x vorticity).

illustrated in Fig.6.5(a). Figure 6.5(a) shows the reversed flow region where the vertical axis indicates the wall-normal distance of its edge. The small separation bubble is formed and turbulent transition occurs near the leading edge in the Cavity and Bc model cases with three-dimensional disturbances $k_{yin}/2\pi = 10, 30$, and 95 which are not observed in two-dimensional input case: $k_{yin}/2\pi = 0$. In three-dimensional input cases, such smaller separation bubble would contribute to the reduction of the drag as seen in Table 6.2. On the other hand, Figs. 6.5(b) and (c) show the spatial distribution of a turbulent kinetic energy (TKE) and spanwise velocity fluctuation $\overline{v'}$, respectively. Note that the vertical axis of Figs.6.5(b) and (c) show the maximum value of TKE and $\overline{v'}$, respectively, along a grid line extended from the airfoil surface at certain x/c (horizontal axis value) position. We call these plots TKE-max and $\overline{v'}$-max lines, respectively. A turbulent transition occurs most quickly and smoothly in the Bc model with $k_{yin}/2\pi = 30$ in Figs. 6.5(b) and (c), which results in the smallest separation bubble observed in Fig.6.5(a). Therefore, the quick and smooth turbulent transition near the leading edge resultantly contribute to the reduction of the drag coefficient. However, the flow is separated near the trailing edge earlier in the Bc model case with $k_{yin}/2\pi = 30$ than the other cases: $k_{yin}/2\pi = 10$ and 95 as shown in Figs.6.5(a) and 6.2. This result indicates that although the three-dimensional turbulent boundary layer (i.e., momentum exchange by a turbulent mixing [2],[3]) is important to maintain the flow close to the airfoil surface, the case

with a quick and smooth turbulent transition could not keep a strong mixing further downstream, which would result in the earlier flow separation near the trailing edge. The trend of the lift coefficient C_L between each three-dimensional Bc model case corresponds to that of the flow separation point near the trailing edge in Fig.6.5(a), where the C_L becomes the worst in $k_{yin}/2\pi = 30$ case. Note that the turbulent mixing is quantitatively evaluated by the $-\overline{u'w'}$ component of a Reynolds shear stress in Fig.6.4, which contribute to inducing a chordwise momentum from the freestream. According to Eq.(**??**), the Reynolds shear stress, $\overline{u'w'}$, can be decomposed [2] into overall phase component, $\overline{\tilde{u}\tilde{w}}$, and overall turbulent component, $\overline{u''w''}$: $\overline{u'w'} = \overline{\tilde{u}\tilde{w}} + \overline{u''w''}$.

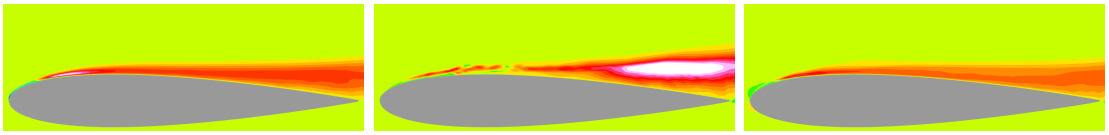

(a) Cavity model (b) $k_{yin}/2\pi = 0$ (c) $k_{yin}/2\pi = 10$

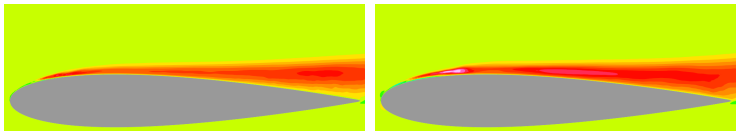

(d) $k_{yin}/2\pi = 30$ (e) $k_{yin}/2\pi = 95$

Fig. 6.4: The turbulent component of the Reynolds shear stress $-\overline{u''w''}/u_\infty^2$.

Overall, although the quick and smooth turbulent transition would contribute to the reduction of the pressure drag owing to minimize the separation bubble near the leading edge, the lift coefficient would be deteriorated due to the flow separation near the trailing edge. Therefore, the Bc model case with $k_{yin}/2\pi = 30$ does not show the best performance in terms of the lift-to-drag ratio although it shows the smallest C_D among all the computational cases in Table 6.2. This indicates that the quick and smooth turbulent transition would not always contribute to an enhancement of aerodynamic coefficient in the present flow conditions and the synthetic jet parameters. Note that the present results are all based on the controlled cases where the aerodynamic coefficients between each model is not significantly different; accordingly more various synthetic jet parameters, e.g., smaller input C_μ, should be examined to verify the present result on the aerodynamic performances. Dispite this, the differences between each Bc model are apparent concerning a turbulent transition and the size of the separation bubble

resultantly; therefore, some optimal parameter would be expected to exist in the spanwise wave-number input from a viewpoint of quick and smooth turbulent transition, which may enhance the aerodynamic performances in more efficiently controlled cases, e.g., using smaller C_μ input. In the next section, we will investigate the spatial development of spanwise disturbances in the controlled flows, which yields three-dimensional mixing and directly contribute to the turbulent transition in three-dimensional Bc model case.

6.5 Spanwise disturbance

6.5.1 Spatial growth of a spanwise disturbance

The spanwise disturbance of the controlled flow field is investigated using a spanwise Fourier transform of the turbulent fluctuation of the velocity: $\hat{u''}_{\rm n}$, where $u_{\rm n}$ is the wall-normal component of the velocity, and the hat indicates the spanwise Fourier mode in the rest of this paper. Note that the value $\hat{u''}_{\rm n}$ corresponds to the amplitude of complex Fourier mode: the energy of spanwise mode in $u''_{\rm n}$.

6.5.1.1 Overall spanwise Fourier modes

Figure 6.6 shows the overall (i.e., time-averaged) spanwise Fourier modes $\overline{\hat{u''}_{\rm n}}$. In Fig.6.6, the spanwise (y-) axis indicates the spanwise wave number $k_y/2\pi$; and the other axes (x and z) show the physical coordinates defined in Fig.**??**. The filled contour visualizes the PSD of the overall spanwise Fourier modes $\overline{\hat{u''}_{\rm n}}$ on $\overline{w'}$-max line, where the definition of the $\overline{w'}$-max line is similar to that of Figs.6.5(b) and (c).

In the Cavity model case (Fig.6.6(a)), a wide range of the wave number $k_y/2\pi$ is introduced from the synthetic jet at the leading edge, but the modes of $k_y/2\pi = 20$ to 30 are selectively amplified at $x/c \simeq 5\%$, which is close to the edge of the separation bubble in the time-averaged flow field shown in Fig.6.5(b). This implies that although the higher wave number such as $k_y/2\pi \geq 30$ is introduced from the synthetic jet, they are shortly damped as convecting in the separated shear layer near the leading edge (approximately at $0.0\% \leq x/c \leq 10.0\%$); at $x \geq 10.0\%$, the modes of $k_y/2\pi = 20$ to 30 are immediately amplified and it remains a peak value further downstream.

In each Bc model case (Figs.6.6(c)–(e)) except for the case with $k_{y\rm in}/2\pi = 0$, the

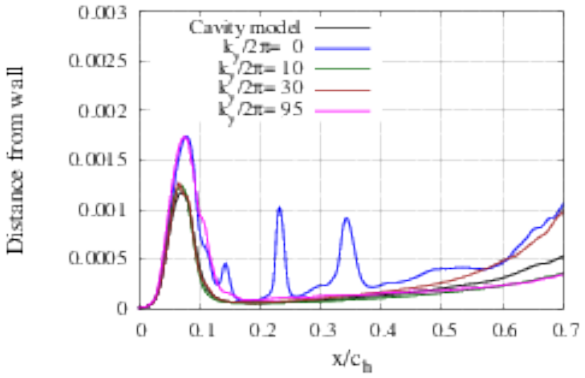

(a) Reversed flow region

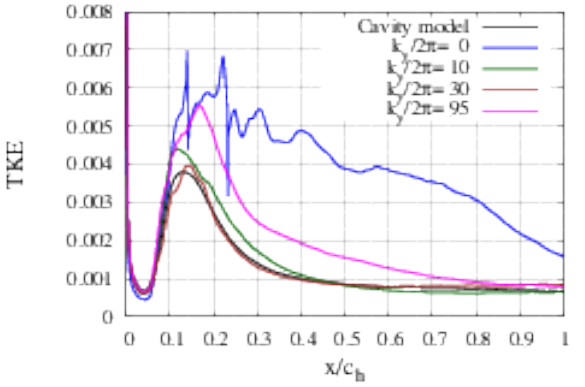

(b) Turbulent kinetic energy

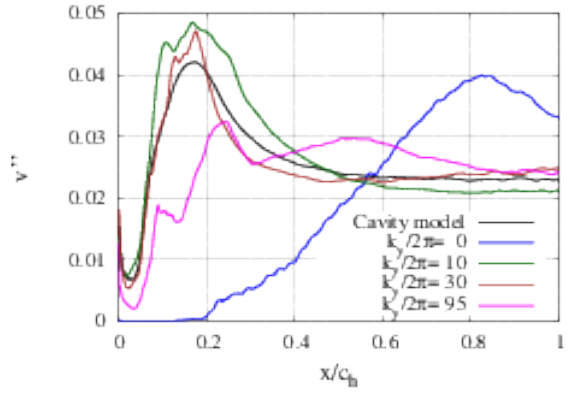

(c) Spanwise velocity fluctuation $\overline{v'}$

Fig. 6.5: Time-averaged flow fields: (a) shows the wall-normal distance of an inflection point from the airfoil surface; (b) shows the turbulent kinetic energy; (c) shows the spanwise velocity fluctuation $\overline{v'}$.

input wave number modes remains strong for $0\% \leq x/c \leq 20\%$. In the Bc model case with $k_{y\mathrm{in}}/2\pi = 95$ in Fig.6.6(e), the higher wave number modes $k_y/2\pi \geq 90$ are shortly damped at $20\% \leq x/c$ although they are close to the input mode. On the other hand, the lower modes ($k_y/2\pi \simeq 10$) appears independently from the higher mode input, which are gradually extended to higher modes and develop the similar distribution of the Cavity model at $50\% \leq x/c$, where the higher mode input is no longer dominant. Concerning that the Bc model case with $k_{y\mathrm{in}}/2\pi = 95$ shows neither the quick nor smooth turbulent transition (Sec.6.4.2) compared to the Cavity and other Bc models, such a higher wave-number mode input does not amplify the spanwise disturbance encouraging the turbulent transition in the present flow condition.

In the lower input-mode cases such as $k_{y\mathrm{in}}/2\pi = 10$ and 30, the strong input-mode is maintained further downstream, i.e., even at $x/c \simeq 40\%$ in Figs.6.6(c) and (d). These input modes would effectively enhance the modes around $k_y/2\pi = 20$ to 30 at $50\% \leq x/c$, which is close to the primary mode observed in the Cavity model case. This implies that the lower modes such as $k_y/2\pi = 10$ and 30 can effectively enhance the spanwise disturbances, which would contribute to the quick and smooth turbulent transition in the present flow condition. In addition, characteristic harmonics of the input wave number mode are strongly enhanced at $x/c \simeq 20\%$ in the Bc model case with $k_{y\mathrm{in}}/2\pi = 30$ in Fig.6.6(c). Such harmonic modes support the existence of coherent structures observed in the instantaneous flow field (Fig.6.3(c)), which cannot be clearly observed in other Bc model cases.

6.5.2 Phase-averaged spanwise Fourier modes

Figure 6.7 shows the phase-averaged spanwise Fourier modes $\langle \hat{u''}_{\mathrm{n}} \rangle$ on $\overline{w'}$-max line. The $\langle \bullet \rangle$ indicates the phase averaged value as introduced in Eq.(**??**). The phases $\phi/2\pi = 2/10$, 4/10, and 6/10 correspond to the blowing phases; and $\phi/2\pi = 8/10$ and 10/10 correspond to the suction phases.

The Cavity model case (Fig.6.7(a)) introduces a wide range of wave number modes at the blowing phase (blue dotted circle in Fig.6.7(a):$\phi/2\pi = 6/10$) as was discussed on the overall Fourier modes in Sec.6.5.1.1. The modes around $k_y/2\pi = 20$ to 30 are selectively amplified during convection and remain strong further downstream (blue dotted circle in Fig.6.7(a):$\phi/2\pi = 10/10$), where the turbulent boundary layer is developed. Note

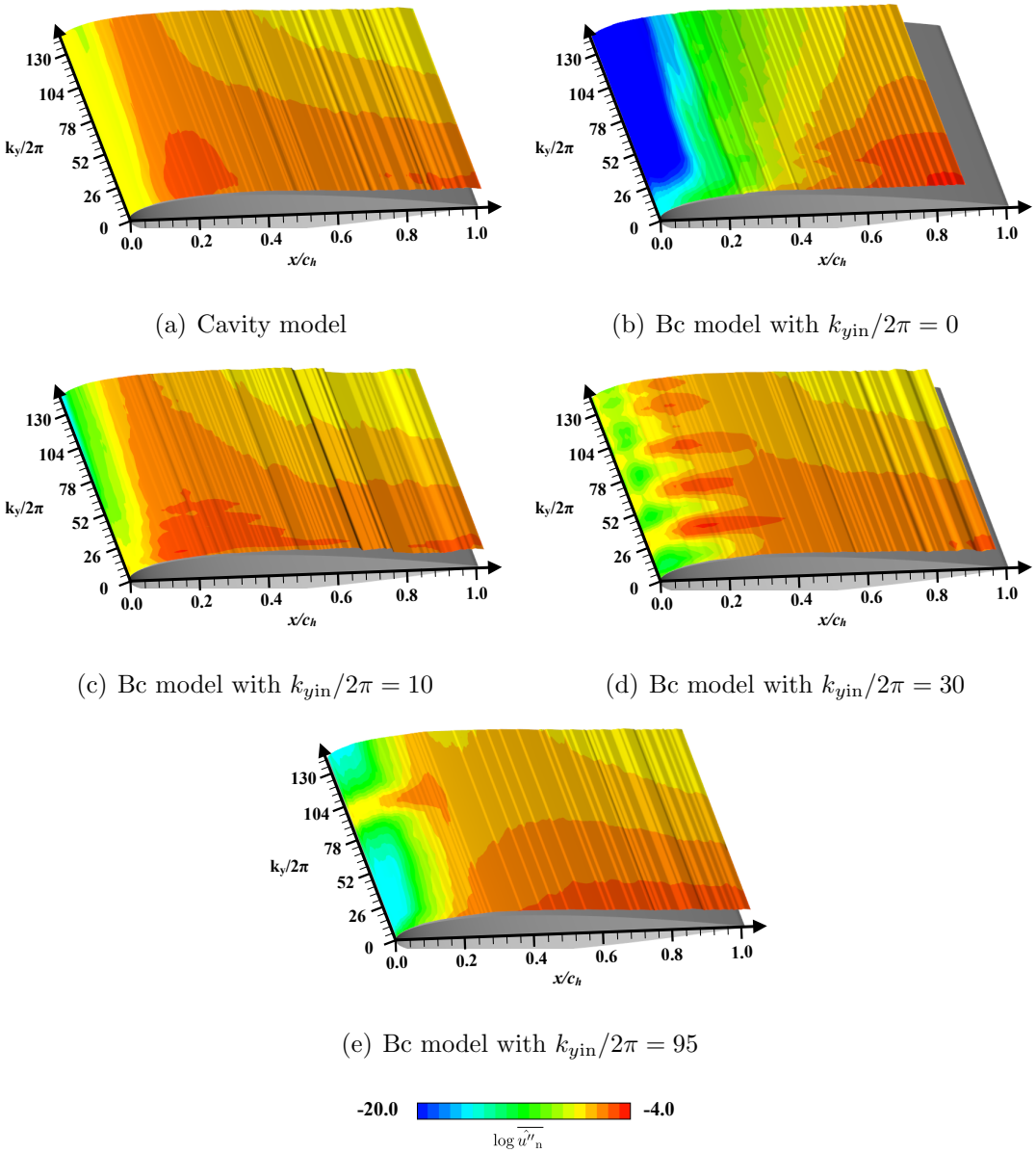

(a) Cavity model

(b) Bc model with $k_{yin}/2\pi = 0$

(c) Bc model with $k_{yin}/2\pi = 10$

(d) Bc model with $k_{yin}/2\pi = 30$

(e) Bc model with $k_{yin}/2\pi = 95$

Fig. 6.6: The overall (time-averaged) spanwise Fourier modes of the wall-normal velocity fluctuation $\overline{\hat{u}''_n}$ are visualized.. (a) Cavity model; (b) Bc model (input mode is $k_{yin}/2\pi = 0$); (c) Bc model (input mode is $k_{yin}/2\pi = 10$); (d) Bc model (input mode is $k_{yin}/2\pi = 30$); (e) Bc model (input mode is $k_{yin}/2\pi = 95$).

that these modes are most amplified at $x/c \simeq 10\%$, where the spanwise small vortex structures are merged to generate a large vortex structure in phase- and span-averaged fields, and turbulent transition takes place [2] .

In the Bc model cases with a three-dimensional spanwise disturbances (Figs.6.7(c)–(e)), the input modes strongly appears during the blowing phases at $\phi/2\pi = 2/10$, $4/10$, and $6/10$. However, the input mode $k_y/2\pi = 95$ in Fig.6.7(e) is damped at $x/c \simeq 20\%$, and another lower modes of $k_y/2\pi = 20$ to 30 become dominant as discussed in Sec.6.4.2. Similarly, in the Bc model cases with $k_{y\mathrm{in}}/2\pi = 10$ and 30, the dominant modes are $k_y/2\pi = 20$ to 30 in Fig.6.7(c) (shown in the blue dotted circle); moreover, these dominant modes are specifically amplified and entrained by the spanwise large vortex structures. This trend is similar to that of the turbulent component of the Reynolds shear stress $-\langle u''w''\rangle$ corresponding to the momentum mixing by turbulent structures, which is considered to be one of the key mechanisms for separation control regarding the momentum induction from the freestream as discussed in our previous work [2]. Therefore, the spatial growth of the spanwise disturbances on coherent spanwise vortex structures would be important from the viepoint of both of turbulent transition and turbulent mixing yielding a chordwise momentum exchange, which will be discussed in the next subsection (Figs.6.8–6.11). Finally, the modes around $k_y/2\pi = 30$ and its harmonics are maintained strong in the Bc model case with $k_{y\mathrm{in}}/2\pi = 30$ (Figs. 6.7(b)) as discussed in Sec.6.4.2 on overall Fourier modes, which turns out to be convected by spanwise vortex structures.

6.5.2.1 Convective growth of phase-averaged spanwise Fourier modes

Figures 6.8–6.11 show the convective growth of phase-averaged spanwise Fourier modes $\langle \hat{u''}_{\mathrm{n}} \rangle$ in the spanwise vortex structures (*Vortex 1, 2* and *3*) detected in the phase- and spanwise-averaged field at $\phi/2\pi = 1/10$ in Figs 6.8(a)–6.11(a). These small spanwise vortex structures are generated from the separated shear layer near the leading edge, which is observed in the phase- and spanwise-averaged flow fields (discussed in the previous studies [2]·[3] in detail). These vortex structures are convecting downstream, and merged to generate larger vortex structures whose period corresponds to the actuation frequency ($St = 6.0(= F^+)$ in the present the condition). The convective growth of phase-averaged spanwise Fourier modes is observed by plotting $\langle \hat{u''}_{\mathrm{n}} \rangle$ on each vortex

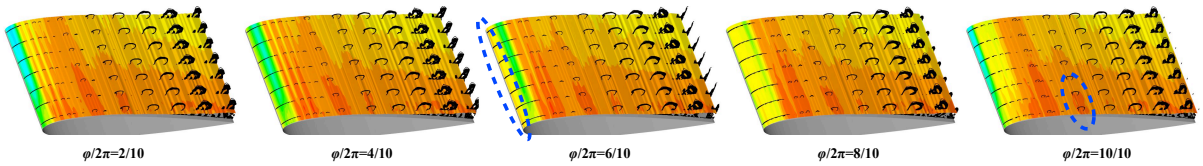

(a) Cavity model

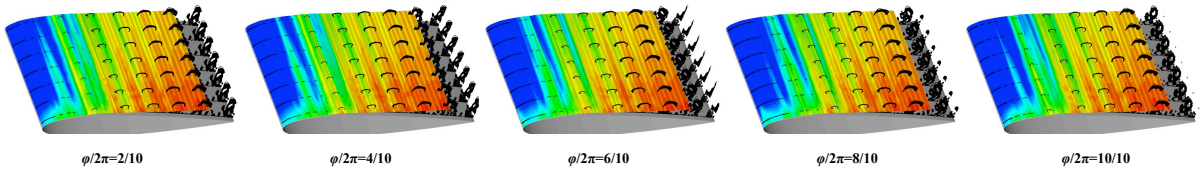

(b) Bc model (input mode is $k_{yin}/2\pi = 0$)

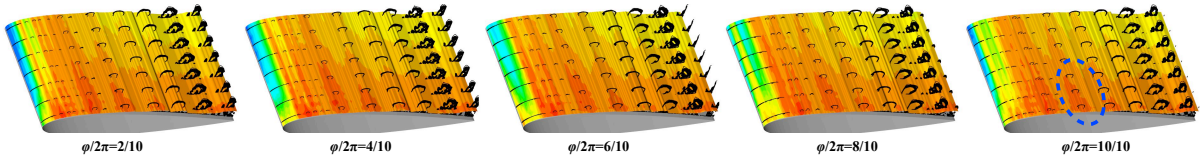

(c) Bc model (input mode is $k_{yin}/2\pi = 10$)

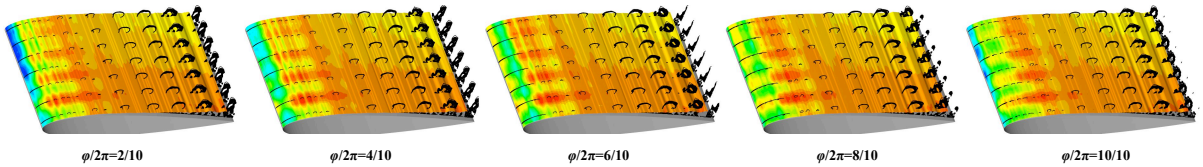

(d) Bc model (input mode is $k_{yin}/2\pi = 30$)

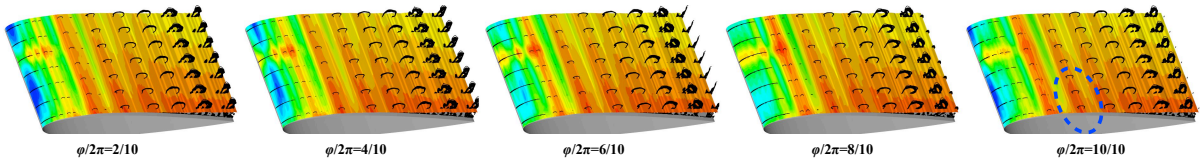

(e) Bc model (input mode is $k_{yin}/2\pi = 95$)

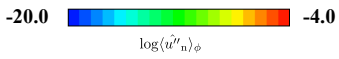

Fig. 6.7: Phase-averaged spanwise Fourier modes of the wall-normal velocity fluctuation $\langle \hat{u''}_n \rangle$ are visualized for $\phi/2\pi = 1/10, 2/10, \ldots, 10/10$; The black contour line shows the second invariant of the velocity gradient tensor at each phase. (a) Cavity model; (b) Bc model (input mode is $k_{yin}/2\pi = 0$); (b) Bc model (input mode is $k_{yin}/2\pi = 10$); (c) Bc model (input mode is $k_{yin}/2\pi = 30$); (d) Bc model (input mode is $k_{yin}/2\pi = 95$).

structures in Figs.6.8–6.11. The points in each plot correspond to the $\langle \hat{u''}_{\rm n} \rangle$ on spanwise vortex structures (*Vortex 1, 2*, and *3*) at each phase. The location of each vortex is first detected by a local maximum of the second invariant of velocity gradient tensor, and the pathline of each vortex centroid is computed using the phase- and span- averaged flow fields for $1/20 \leq \phi/2\pi \leq 60/20$, i.e., 3 cycles. In terms of the linear stability theory [**?**][**?**] , secondary instability mode based on the spanwise vortex structure is expected to yield the optimal growth of spanwise distubance modes which would result in quick and smooth turbulent transition.

In the Cavity model, the spatial distribution does not show significant difference between each mode (shown in Fig.6.8(b)–(d)), where both of $k_y/2\pi$ = 10, 20, 30, and 90 modes show qualitatively similar profiles. The growth rates ($\beta := D_\phi \log[\langle \hat{u''}_{\rm n} \rangle$) also show qualitatively similar results for $k_y/2\pi$ = 10 to 90 (shown in Fig.6.8(b)–(d)). This implies that the selectively amplified mode cannot be clarified assuming the exponential growth along the vortex convection in the framework of linear stability theory in the present flow condition. The reason is that a wide range of strong spanwise disturbances are introduced from the synthetic jet using the present parameters, where the nonlinear effect cannot be neglected during the convection. The mode of $k_y/2\pi$ = 30 strongly remains further downstream compared to the other modes on both of the *Vortex 1* and *2* (Fig.6.8(b) and (c)) as discussed in Sec. 6.5.1.1 and 6.5.2. In the Bc model case with $k_{y\rm in}/2\pi = 10$ in Fig.6.9(b)–(d), the input mode of $k_y/2\pi = 10$ is dominant at $x/c \leq 10\%$ in all vortices, but the mode of $k_y/2\pi$ = 20 exceed $k_y/2\pi$ = 10 at $x/c \leq 15\%$ on the *Vortex 3*. Similarly, in the Bc model case with $k_{y\rm in}/2\pi = 95$ in Fig.6.11(b)–(d), the lower modes such as $k_y/2\pi$ = 10–30 exceed the input mode $k_y/2\pi \simeq 90$ at $x/c \simeq 20\%$. On the other hand, in Fig.6.10(b)–(d), the case with $k_{y\rm in}/2\pi = 30$ shows that the input mode of $k_y/2\pi$ = 30 remains strong further downstream although its growth rate shows the similar profiles to other modes $k_y/2\pi = 10, 20$, and 90 in Fig.6.10(e)–(g).

6.6 Summary

The spatial growth of the spanwise disturbance induced by a synthetic jet is investigated on separated-flow control around NACA0015 (Re=63,000 and $AOA = 12.0^\circ$) using LES. The synthetic jet is installed at the leading edge and actuated with nondimensional fre-

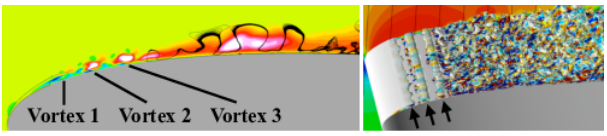

(a) *Vortex 1, 2,* and *3* on phase-averaged field (left) and instantaneous field (right) at $\phi/2\pi = 1/10$

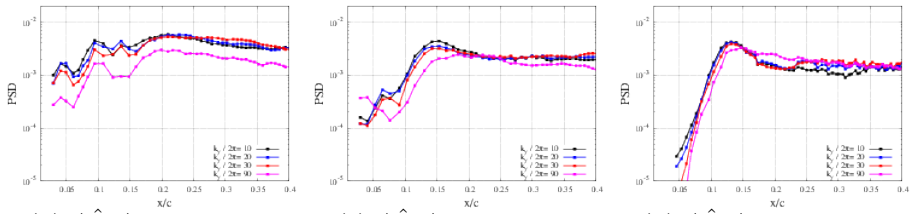

(b) $\langle \hat{u''}_n \rangle$ on *Vortex 1* (c) $\langle \hat{u''}_n \rangle$ on *Vortex 2* (d) $\langle \hat{u''}_n \rangle$ on *Vortex 3*

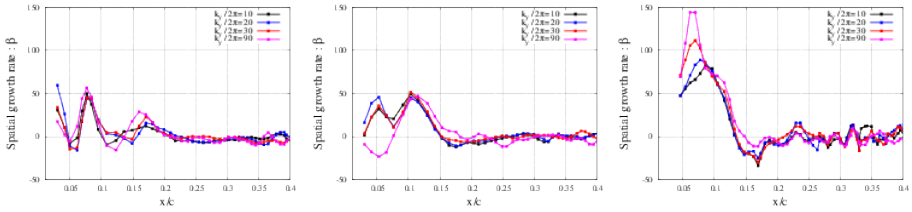

(e) β on *Vortex 1* (f) β on *Vortex 2* (g) β on *Vortex 3*

Fig. 6.8: The convective growth of $\langle \hat{u''}_n \rangle$ on the *Vortex 1,2* and *3* in Cavity model. The spatial growth rate $\beta := D_\phi \log[\langle \hat{u''}_n \rangle]$ is also shown for each spanwise wave number.

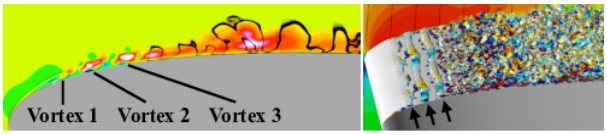

(a) *Vortex 1, 2,* and *3* on phase-averaged field (left) and instantaneous field (right) at $\phi/2\pi = 1/10$

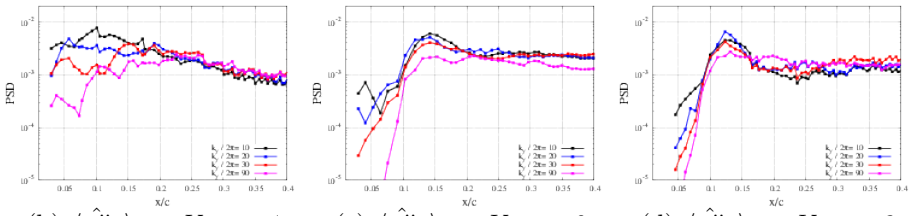

(b) $\langle \hat{u''}_{\mathrm{n}} \rangle$ on *Vortex 1* (c) $\langle \hat{u''}_{\mathrm{n}} \rangle$ on *Vortex 2* (d) $\langle \hat{u''}_{\mathrm{n}} \rangle$ on *Vortex 3*

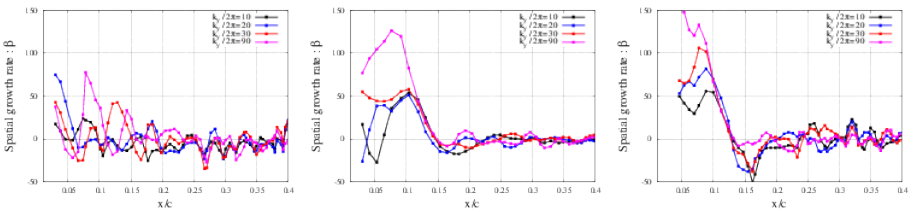

(e) β on *Vortex 1* (f) β on *Vortex 2* (g) β on *Vortex 3*

Fig. 6.9: The convective growth of $\langle \hat{u''}_{\mathrm{n}} \rangle$ on the *Vortex 1,2* and *3* in the Bc model with $k_{y\mathrm{in}}/2\pi = 10$. The spatial growth rate $\beta := D_\phi \log[\langle \hat{u''}_{\mathrm{n}} \rangle]$ is also shown for each spanwise wave number.

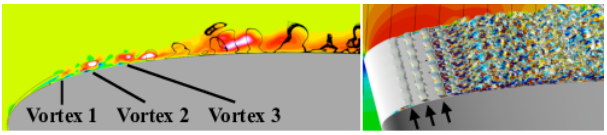

(a) *Vortex 1, 2,* and *3* on phase-averaged field (left) and instantaneous field (right) at $\phi/2\pi = 1/10$

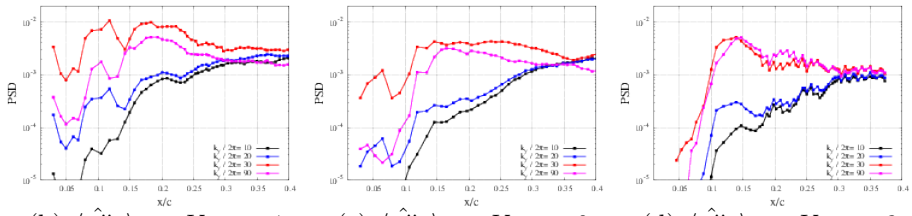

(b) $\langle \hat{u''}_{\mathrm{n}} \rangle$ on *Vortex 1* (c) $\langle \hat{u''}_{\mathrm{n}} \rangle$ on *Vortex 2* (d) $\langle \hat{u''}_{\mathrm{n}} \rangle$ on *Vortex 3*

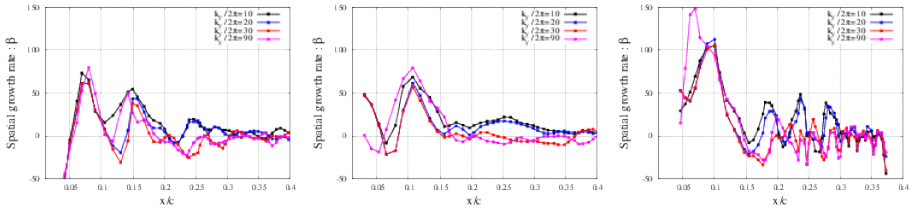

(e) β on *Vortex 1* (f) β on *Vortex 2* (g) β on *Vortex 3*

Fig. 6.10: The convective growth of $\langle \hat{u''}_{\mathrm{n}} \rangle$ on the *Vortex 1,2* and *3* in the Bc model with $k_{y\mathrm{in}}/2\pi = 30$. The spatial growth rate $\beta := D_\phi \log[\langle \hat{u''}_{\mathrm{n}} \rangle]$ is also shown for each spanwise wave number.

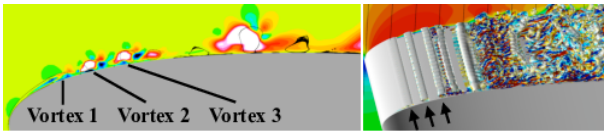

(a) *Vortex 1, 2,* and *3* on phase-averaged field (left) and instantaneous field (right) at $\phi/2\pi = 1/10$

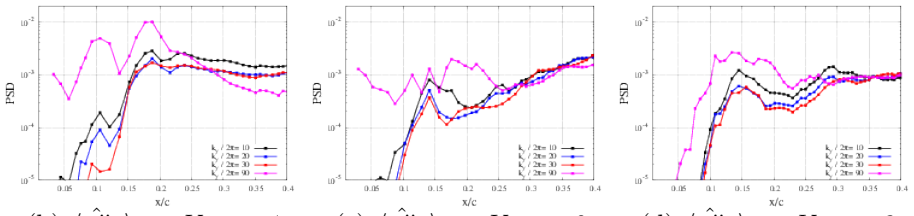

(b) $\langle \hat{u''}_{\mathrm{n}} \rangle$ on *Vortex 1* (c) $\langle \hat{u''}_{\mathrm{n}} \rangle$ on *Vortex 2* (d) $\langle \hat{u''}_{\mathrm{n}} \rangle$ on *Vortex 3*

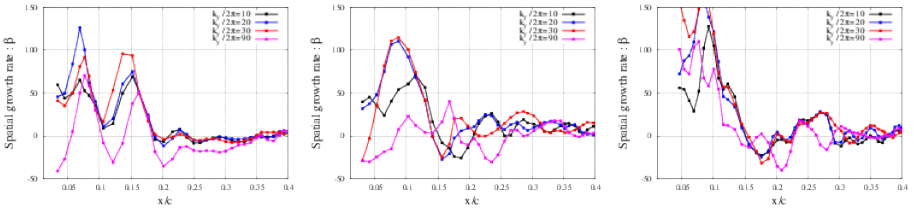

(e) β on *Vortex 1* (f) β on *Vortex 2* (g) β on *Vortex 3*

Fig. 6.11: The convective growth of $\langle \hat{u''}_{\mathrm{n}} \rangle$ on the *Vortex 1,2* and *3* in the Bc model with $k_{y\mathrm{in}}/2\pi = 95$. The spatial growth rate $\beta := D_\phi \log[\langle \hat{u''}_{\mathrm{n}} \rangle]$ is also shown for each spanwise wave number.

quency $F^+ = 6.0$, which has been revealed to be an optimal input frequency in terms of lift-to-drag ratio in the previous study [2] . The jet profile of the Bc model is constructed from the phase- and spanwise-averaged jet profile obtained by LES of the synthetic jet [2] (i.e., Cavity model) with its amplitude being sinusoidally oscillated in a spanwise direction: the artificial spanwise oscillation of the jet profile in the Bc model is chosen to be $k_{y\mathrm{in}} = 0, 10, 30$, and 95. LES of the airfoil-flow control was carried out using these Bc models, and the following items are found in this study: 1) in the Cavity model case, the spanwise disturbance modes around $k_y/2\pi = 30$ are selectively amplified near the synthetic jet, which remains strong in the turbulent boundary layer; 2) in the Bc model cases, the cases for $k_{y\mathrm{in}}/2\pi > 0$ (i.e., three-dimensional input cases) show higher aerodynamic performance than the two-dimensional input case (i.e., without artificial spanwise disturbances: $k_{y\mathrm{in}}/2\pi = 0$); 3) in the Bc model cases, the most quick and smooth turbulent transition is observed in the case with $k_{y\mathrm{in}}/2\pi = 30$, where the coherent spanwise structure strongly remains in the turbulent boundary layer although its aerodynamic performance is not the best, which indicates that in the present condition, the spanwise disturbance of the jet profile does not always contribute to the higher aerodynamic performance even if it provides quick and smooth turbulent transition. 4) the mechanism of the strongly remaining mode ($k_y/2\pi = 30$) in the Cavity model cannot be clarified assuming the exponential growth along the vortex convection based on the secondary instability mode, because strong nonlinear interaction of the spanwise disturbances would take place in the present flow condition and input parameters of the synthetic jet. The last item is expected to be verified by examining the smaller input parameters of the synthetic jet (i.e., smaller C_μ), where the difference of the aerodynamic performances would be clearly observed for Bc model cases with various spanwise disturbances.

Chapter 7

General mechanism on a separation control using micro devices

7.1 Outline

7.2 Case description

The computational cases for separation control using the SJ and PA are described in Table 7.1.

Table 7.1: Computational cases. SJ and PA are installed at the leading edge of the airfoil.

case name	input momentum (C_μ)	F^+					
strong input (SJ)	2.00×10^{-3}	1.0,	6.0,	10,	15,	20,	30
strong input (PA)	2.00×10^{-3}	1.0,	6.0,	10,	15,	20,	30
weak input (SJ)	2.00×10^{-5}	1.0,	6.0,	10,	15,	20,	30
weak input (PA)	5.15×10^{-5}	1.0,	6.0,	10,	15,	20,	30

The computational results of the SJ are the same with those discussed in Sec.**??**. In order to compare the capabilities of the SJ and PA, both of the strong and weak input momentum cases are taken. Note that the weak C_μ values are different for SJ and PA ($C_\mu = 2.00 \times 10^{-5}$ for SJ; and $C_\mu = 5.15 \times 10^{-5}$ for PA) because the case

with $C_\mu = 2.00 \times 10^{-5}$ cannot control the separation using the PA, and the case with $C_\mu = 5.15 \times 10^{-5}$ would be close to the minimum input controllable case. Such a difference in the PA and SJ would be caused by the definitions of C_μ, which is defined using the maximum velocity at the orifice exit for the SJ and spatial integral of the time-averaged body force for the PA. The detail of the differences of input fluctuations are discussed in the next section.

7.3 Differences of fluctuations input from the SJ and PA

The time average of an induced flow by the PA is in the direction from the exposed to covered [5]. On the other hand, the time-averaged (net) input momentum from the SJ should be zero because the blowing and suction phases periodically occur. In this chapter, C_μ is adopted as the criteria for the strength of input momentum by each devices, which has conventionally used. Although the definitions of C_μ are not strictly the same for the SJ and PA, it would not affect the present discussion on the separation control mechanism. Another possibility of the criteria for the strength of an input is the net energy, which is not focused in this chapter. In this section, the following viewpoints are taken for the comparison of input fluctuation from the SJ and PA:

A. Existence of direct momentum addition (wall-tangential component) from the induced flow

B. Locality of the induced flow

C. Fluctuation in spanwise direction (three-dimensional structure in the induced flow)

D. Timewise fluctuation of the induced flow

A. Existence of direct momentum addition (wall-tangential component) from the induced flow

Figure 7.1 show the phase- and spanwise-averaged velocity component at the orifice exit, where u_{jet} is in the wall-normal (normal to the orifice exit) component and w_{jet} is in

the wall-tangential (along the orifice exit) component. The notations of u and w follow those used for the flows around the airfoil so that the negative value for the $u_{\rm jet}$ indicates the blowing phase. The horizontal axis $x_{\rm orifice}$ shows the coordinate along the orifice exit plane (see the red line in Fig.7.1(d)), which is on the orifice section at the half depth. The blowing phase ($\varphi = \pi/2$) is illustrated by solid lines, and the suction phase ($\varphi = 3\pi/2$) is by the broken lines, where the results of four types of the C_μ are shown. The actuation frequency F^+ is fixed to 6 (the other frequencies show the similar features explained below).

All the different input momentum cases show that $w_{\rm jet}$ (wall-tangential component) is approximately 10% so that $u_{\rm jet}$ (wall-normal component) is dominant in the input fluctuation. In these cases, the three cases ($C_\mu = 2.0 \times 10^{-3}, 2.0 \times 10^{-4}$, and 2.0×10^{-5}) can supress the separation. Note that $w_{\rm jet}$ and $u_{\rm jet}$ show asymmetric profiles with respect to the center of the orifice ($x_{\rm orifice} = 0$) at the suction phase. This is caused by the external flow passing across the orifice exit, where the internal flow is entrained in the downstream direction ($x_{\rm orifice} > 0$). When the SJ is located in the quisent flow, the profiles should be symmetric [24] and the wall-tangential flow component should be ideally zero, but in the present separation controlled case, the internal flow is slightly affected by the external flow.

On the other hand, the induced flow by PA has large component of wall-tangential flow so that the momentum in the freestream direction more directly introduced from PA than SJ, which is one of the important mechanism of the separation control using strong input fluctuation. The difference of the control capability caused by this difference would arise at the case with strong input momentum (large C_μ).

B. Locality of the induced flow

Figure 7.2 shows the PSD of the wall-normal fluctuation near the leading edge in the separation control using a weak input with $F^+ = 6.0$. The PSD is taken on the TKE-max line (see Sec.**??**) for each x/c_h. The PSD of the SJ and PA commonly show the peak at the actuation frequency $F^+ = 6.0$ and its harmonics near the leading edge. On the other hand, the PSD of $St = 6.0$ of the actuation frequency is approximately 10 times larger in the SJ than PA although the momentum coefficients (C_μ) are set to almost the same value ($C_\mu = 2.00 \times 10^{-5}$ for SJ; $C_\mu = 5.15 \times 10^{-5}$ for PA). This indicates that the velocity

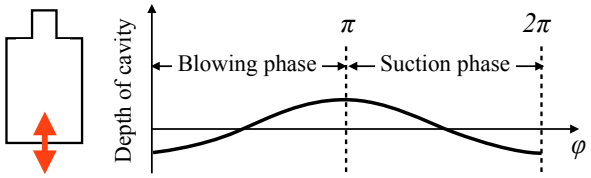

(a) Phase diagram

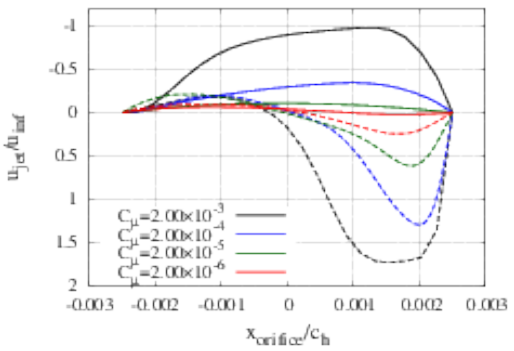

(b) Wall-normal velocity

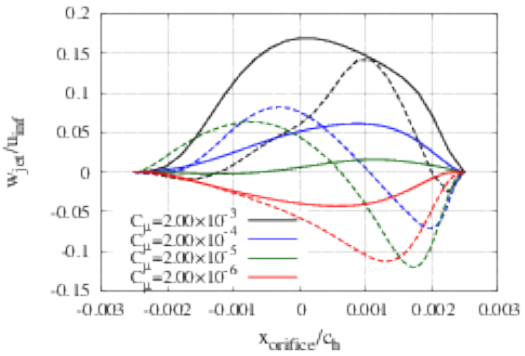

(c) Wall-tangential velocity

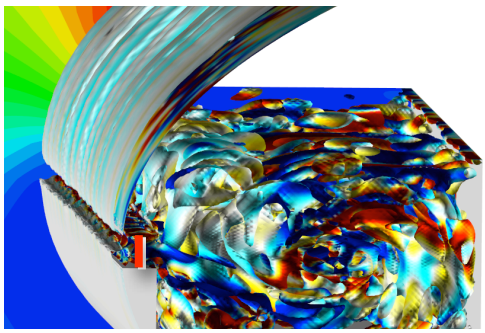

(d) Vortex structures inside the cavity ($C_\mu = 2.0 \times 10^{-3}, F^+ = 6.0$)

Fig. 7.1: Phase-averaged velocity profile inside the orifice of SJ. Solid/broken lines show the blowing ($\varphi = \pi/2$) /suction ($\varphi = 3\pi/2$) phases, respectively: (a) wall-normal velocity; (b) wall-tangential velocity; (d) instantaneous vortex structures inside the cavity.

of the induced flow at the referened point is different although the input momentum is almost the same order because the present PSD shows the wall-normal component of the fluctuation.

Figure 7.3 shows the spatial profile of time- and spanwise-averaged induced flow by PA and SJ. The induced flow of SJ is evaluated from the flow field inside the orifice in the separatin controlled cases, where the r.m.s is taken for the wall-normal component (w_{jet}) at the half depth of the orifice. Note that for the consiseness, the vertical axis of Fig.7.3 is the coordinate along the orifice exit plane (x_{jet} in Fig.7.1(a) and (b)) for the profile of SJ fluctuation. The induced flow of PA is computed in the quisent flow [5] because the induced flow of PA cannot be easily evaluated in the separation controlled flow. For the profile of PA fluctuation, the vertical axis of Fig.7.3 is the coordinate in the wall-normal direction. Each profiles in Fig.7.3 (solid lines show the SJ; dotted lines show the PA) are not exactly the same between SJ and PA, but it shows that the induced flow is locally larger and more localized in the flucutation of SJ than that of PA. This trend for the locality of the induced flow would be similarly expected in the separation controlled flow using PA, which is shown in the schematic of the induced flow in Fig.7.4. In the present flow/actuator conditions, the boundary layer covers the leading edge where the SJ and PA is implemented. The thickness of the boundary layer is so small at the leading edge that the SJ can more effectively introduce the fluctuation into the boundary layer than PA. As a result, the introduced and developing fluctuation inside the boundary layer is larger in the SJ than PA, which would affect the PSD in the separated shear layer as shown in Fig.7.2.

However, the spatial profiles of induced flow by SJ can be changed by and based on the orifice width, and the distance between the separated shear layer and the orifice exit significantly depends on the flow condition (e.g., AoA) and the location of the SJ. Therefore, the locality of the induced flow by SJ is not always superior to that by PA, which should be carefully discussed in the different flow/actuator conditions. Additionally, the difference of the locality of the induced flow would not be so large that the order of the induced flow is different by 10 times between SJ and PA in Fig.7.2.

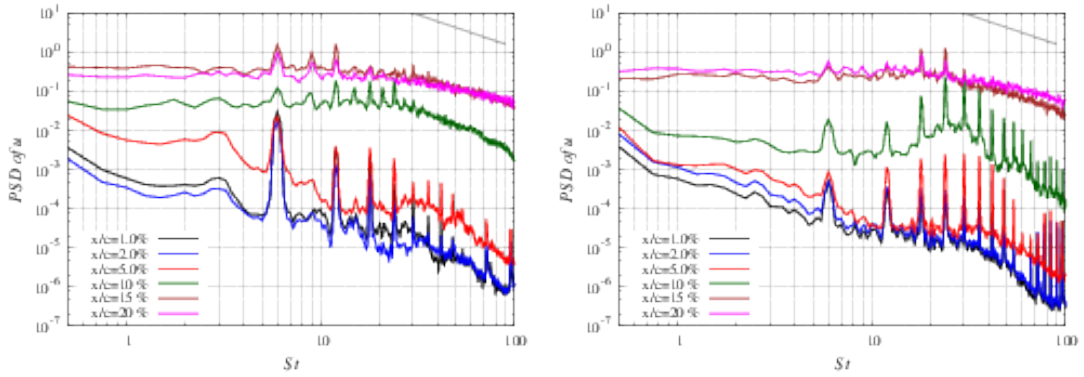

(a) $SJ, C_\mu = 2.00 \times 10^{-5}, F^+ = 6.0$ (b) $PA, C_\mu = 5.15 \times 10^{-5}, F^+ = 6.0$

Fig. 7.2: PSD of wall-tangential velocity fluctuation near the airfoil surface in separation control. The straight line with gray color shows Kolmogorov's 5/3 law in each figure.

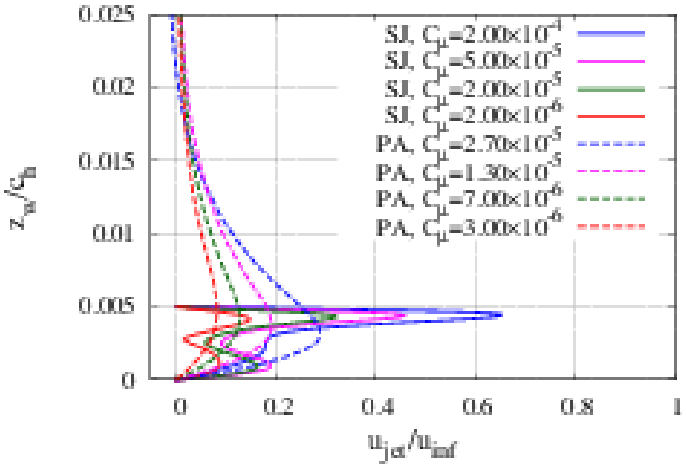

Fig. 7.3: Comparison of time-averaged velocity profiles of the fluctuation (wall-tangential component for PA; wall-nomral component for SJ).

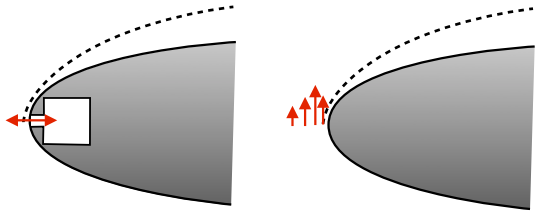

Fig. 7.4: Schematics of induced flow near the leading edge by SJ (left) and PA (right); grey region shows a zoomed view of the leading edge of an airfoil; red arrows indicate the induced flucuation; black dotted lines show separation streamlines.

C. Fluctuation in spanwise direction (three-dimensional structure in the induced flow)

Figure 7.5 (a) show the turbulent component of the spanwise velocity inside the orifice for the four controlled cases using the SJ (actuation frequency is fixed to $F^+ = 6.0$). The solid and dashed lines show the blowing and suction phases, respectively ($\varphi = \pi/2$ and $3\pi/2$). The stronger input momentum provides larger turbulent component of the spanwise fluctuation inside the cavity, which indicates the strong three-dimensional structure of the input fluctuation. Such an effect of input momentum coefficient on the three-dimensional structure of the induced flow has been reported in the previous studies on the induced flow from the SJ for the quisent condition [**?**], where the effect of the actuation frequency has been also arranged. Figure 7.6 shows the instantaneous vortex structures inside the cavity for three different C_μ at each phase $\varphi/2\pi = 1/10$ to $9/10$, where the isosurface is of the second invariant of the velocity gradient tensor colored by the chordwise vorticity. These figures show the strong three-dimensional structure appear inside the cavity even with the separation controlled cases in the present conditions.

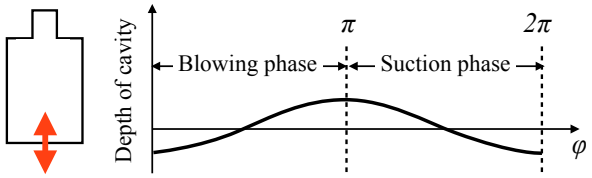

(a) Phase diagram

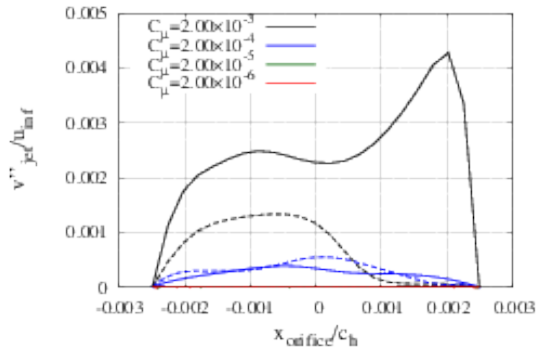

(b) Spanwise fluctuation

Fig. 7.5: Phase-averaged velocity profile inside the orifice of SJ. Solid/broken lines show the blowing ($\varphi = \pi/2$) /suction ($\varphi = 3\pi/2$) phases, respectively.

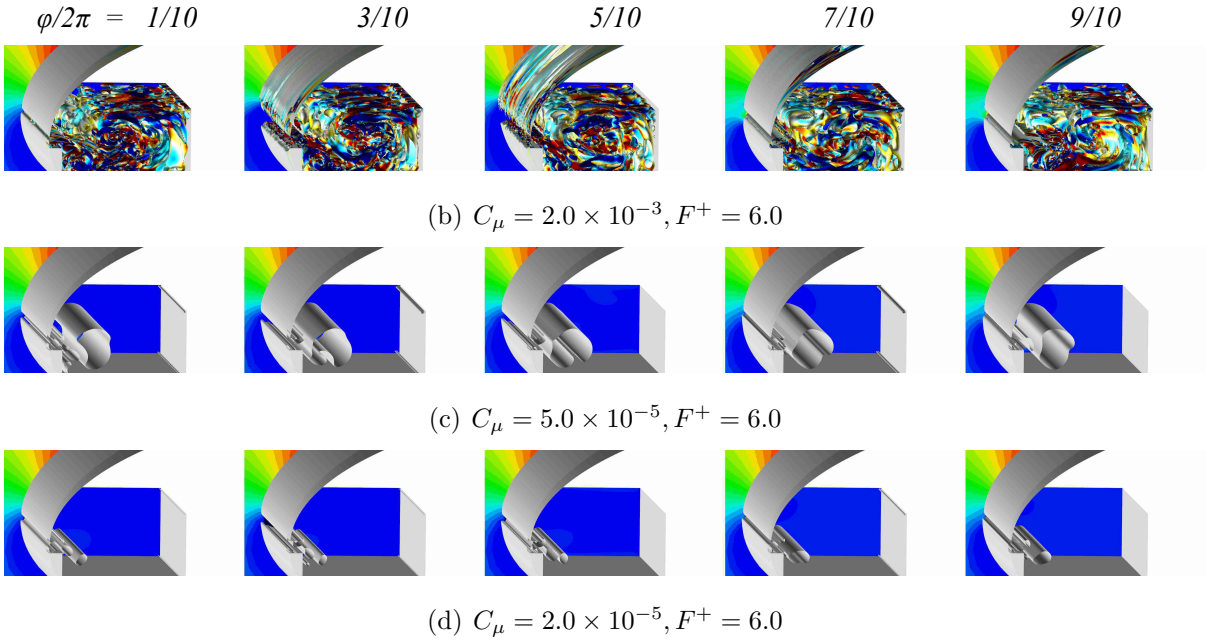

(b) $C_\mu = 2.0 \times 10^{-3}, F^+ = 6.0$

(c) $C_\mu = 5.0 \times 10^{-5}, F^+ = 6.0$

(d) $C_\mu = 2.0 \times 10^{-5}, F^+ = 6.0$

Fig. 7.6: Instantaneous vortex structure inside the cavity for three different C_μ with $F^+ = 6.0$.

On the other hand, the body force model for the PA adopts the spanwise uniform (two-dimensional) profiles so that the three-dimensional flow structure would not be generated in the present study. Note that the three-dimensionality of the body force (spanwise fluctuation) is recently reported by several researchers, which would not significantlly affect the three-dimensional structures of the induced flow[**?**]. For these observation, the differences for the SJ and PA arise in the spanwise fluctuation (three-dimensional structure of the induced flow) when the input momentum coefficient C_μ is strong, which would affect the quickness and smoothness of turbulent transition inside the separated shear layer near the leading edge. The cases with weak input momentum ($C_\mu = O(10^-5)$ in the present condition) do not show the strong spanwise fluctuation even in the SJ, therefore the induced flow from the SJ and PA do not show significant differences.

D. Timewise fluctuation of the induced flow

In the PSD of the wall-normal fluctuation (Fig.7.2), the PSD of high frequency modes at $St \simeq 100$ is larger in PA than SJ near the leading edge, where the fluctuation of induced flow directly affects its profile. Therefore, the difference between SJ and PA in such

high frequency domain is caused by the timewise fluctuation of the induced flow. The actuation frequency $F^+ = 6.0$ is common for each devices so that the PSD of $St = 6.0$ and its harmonics are discretely enhanced even in the downstream direction. On the other hand, only the PA contains the higher ($St \geq 100$) frequencies in the induced flow because of the base frequency of AC input vortage. Figures **??**(a) and (b) clearly show the differences in the history of input fluctuations. Similar trend in the large amplitude of higher frequency fluctuation ($St \geq 100$) has been reported in the previous studies for the PA [27][5], where the operation using the burst mode (duty cycle) is adopted.

In order to clarify the effect of base frequency in the PA operation, the following computations are additionally conducted for the SJ in the quisent flow. The geometry of the SJ is the same as that in the previous section in this thesis. Figure 7.7 shows the PSD of burst and normal actuation using SJ in the quisent flow. The PSD is taken at the center of the orifice exit for the wall-normal component of the flow velocity. The result clearly shows that the PSD of higher frequencies ($St \simeq 100$) is largely enhanced in the burst actuation case than the normal case. This indicates that the burst actuation can introduce the higher frequency fluctuation of the base frequency in the induced flow.

Such a higher frequency mode can affect the nonlinear growth regime in the separation controlled cases (see Sec.**??**). On the other hand, the variation of the base frequency do not so much affect the capability of the separation control using the burst actuation of PA [28], whereas the differences from the normal actuation case without such higher frequency fluctuation (such as the present SJ operation) are not well discussed.

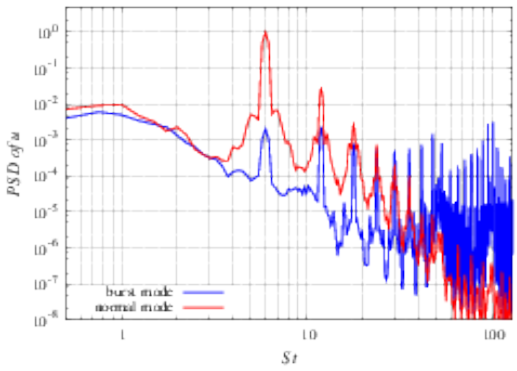

Fig. 7.7: PSD of wall-tangential velocity fluctuation near the airfoil surface in separation control. The straight line with gray color shows Kolmogorov's 5/3 law in each figure.

7.4 Comparison of the capabilities for separation control

7.4.1 Time-averaged aerodynamic coefficients

In this section, the capabillities of the SJ and PA are compared in terms of time-averaged aerodynamic coefficients. Figure 7.8 show time-averaged aerodynamic coefficients, where the horizontal axis indicates the actuation frequency F^+, and the vertical axis shows each time-averaged coefficients using the SJ and PA. Red, blue, and black lines show the strong, weak, and off controlled cases; and the solid and dashed lines show the SJ and PA result, respectively. The capabilities of the sepation control is evaluated based on the time-averaged lift-drag ratio throughout this chapter. In both of the SJ and PA, the lift-drag ratio is the most recovered at $6 \leq St \leq 20$ for either strong or weak input momentum, therefore the optimal frequency for the separation control in the present flow condition would be localized commonly for each devices. In order to discuss the mechanism of the locality of the optimal actuation frequency, the controlled flow fields of $F^+ = 1.0$ and 6.0 are mainly focused on in each devices hereafter.

In the cases with a weak input ($C_\mu = 2.00 \times 10^{-5}$ for SJ; $C_\mu = 5.15 \times 10^{-5}$ for PA), the lift-drag ratio of PA is lower than that of PA in the $F^+ = 6.0, 10$, and 15 cases. Specifically, the case with $F^+ = 20$ can suppress the separation only when the SJ is adopted. In this way, in the cases with a weak input momentum, the SJ achieves slightly better control capabilities for the wide range of F^+ although the C_μ value of PA is approximately two times larger than that of SJ. Such a difference would be partially caused by the locality of the induced flow described in Sec.**??** (B. Locality of). That is, the energy of input fluctuation (e.g., wall-normal fluctuation) introduced from the devices into the separated shear layer is larger in SJ than PA, which causes the turbulent transition in more upstream position and thus the size of the separation bubble is kept smaller (see the red lines in Fig.**??**). Note that in the case with $F^+ = 1.0$ (both devices cannot suppress the separation), the lift-drag ratio, lift, and drag coefficients are better in PA than SJ. This would be related to the existence of the higher frequency fluctuations in the induced flows (see D. Timewise fluctuation of the induced flow in Sec.**??**), which will be discussed in Sec.**??** in detail. On the other hand, in the cases with a strong input

($C_\mu = 2.00\times10^{-3}$ for SJ and PA), the lift-drag ratio of PA is better than that of SJ in each actuation frequencies. This would be caused by the difference of the direct momentum addition in the induced flow (see A. in Sec.**??**), where the PA can more directly introduce the momentum in the freestream direction. The effect of direct momentum addition is thought to be more significant than the other effects such as three-dimensional structure of the induced flow (See C. in Sec.**??**) and locality of the induced flow (B. in Sec.**??**) in the present condition. This is because the turbulent transition occurs at more upstream in the case of SJ than PA, which affects the size of the separation bubble (see blue lines in Fig.**??**).

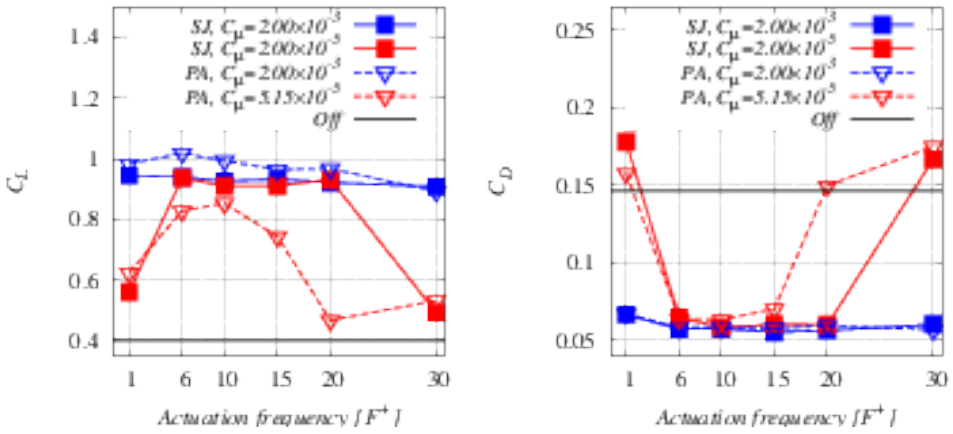

(a) C_L (b) C_D

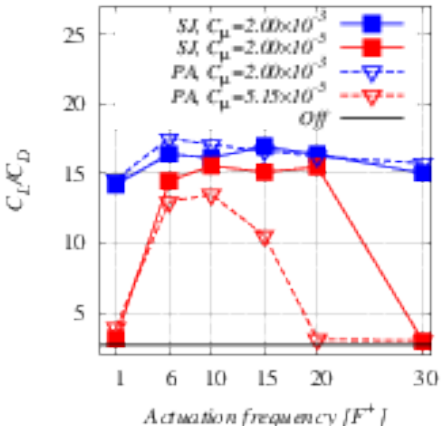

(c) C_L/C_D

Fig. 7.8: Aerodynamic coefficients arranged by F^+. Blue and red solid lines show SJ results of $C_\mu = 2.0 \times 10^{-3}$ and 2.0×10^{-5}; blue and red dashed lines indicates PA results of $C_\mu = 2.0 \times 10^{-3}$ and 5.15×10^{-5}, respectively.

7.4.2 Controlled flows

Figure7.9 shows the time- and spanwise averaged flows of the chordwise velocity component u/u_∞ in the cases with $F^+ = 1.0$ and 6.0. In the strong input cases (Fig.7.9 (a)–(d)), attached flows are obtained using both of the SJ and PA. The separation bubbles are generated near the leading edge in the cases with both devices, where the size of the separation bubble is smaller in $F^+ = 6.0$ than 1.0. Such a trend in the size of the separation bubble is more clearly observed in the reversed flow region shown in Fig.7.10. On the other hand, in Fig.7.10, the size of the separation bubble becomes smaller in the cases with SJ than PA for each actuation conditions. This difference between each devices will be precisely discussed in the context of a turbulent transition in the separated shear layer in the next subsection.

Figure **??** shows the instantaneous flow fields, where the isosurfaces are a second invariant of the velocity gradient tensor colored by the chordwise vorticity. In each cases, the two-dimensional (spanwise uniform) vortex structures are emitted from the separated shear layer, which shedding downstream with a three-dimensional fluctuation. When the flow is controlled (except for the cases with $F^+ = 1.0$ of a weak input for SJ and PA), the both devices achieve the separation controlled flow with a laminer separation bubble and turbulent boundary layer is developed over the airfoil surface. In the case with a strong input, the SJ introduces three-dimensional fluctuation near the leading edge while the PA only introduce the two-dimensional fluctuation, which is discussed in B. in Sec.**??**.

7.4.3 Decomposition of turbulent statistics by the phase-averaging procedure

Figure 7.12 shows the periodic and nonperiodic (turbulent) components of the Reynolds shear stress: $\overline{u'w'} = \overline{\tilde{u}\tilde{w}} + \overline{u''w''}$. The left column shows the overall component of $\overline{u'w'}$, middle and right column shows the phase and turbulent components of $\overline{\tilde{u}\tilde{w}}$ and $\overline{u''w''}$. All the cases using PA show that the turbulent component $\overline{u''w''}$ is dominant and turbulent vortex structures mainly contribute to an exchange of the chordwise-momentum. This is similar to the cases using SJ as discussed in Sec.**??** (see Fig.4.18). On the other hand, the slight difference appears for the SJ and PA cases in terms of the periodic component of the Reynolds shear stress. For example, the strong input case ($C_\mu = 2.0 \times 10^{-3}$) with

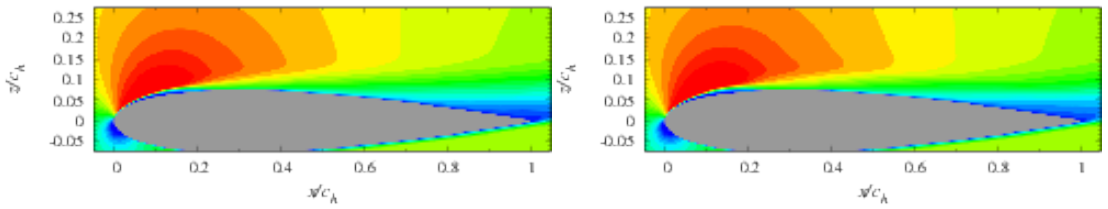

(a) $C_\mu = 2.00 \times 10^{-3}, F^+ = 1.0$ (SJ)

(b) $C_\mu = 2.00 \times 10^{-3}, F^+ = 1.0$ (PA)

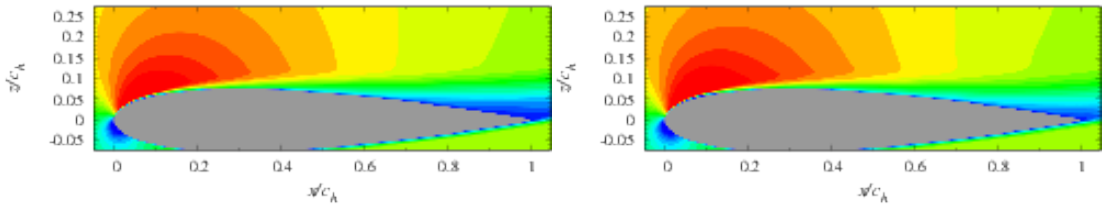

(c) $C_\mu = 2.00 \times 10^{-3}, F^+ = 6.0$ (SJ)

(d) $C_\mu = 2.00 \times 10^{-3}, F^+ = 6.0$ (PA)

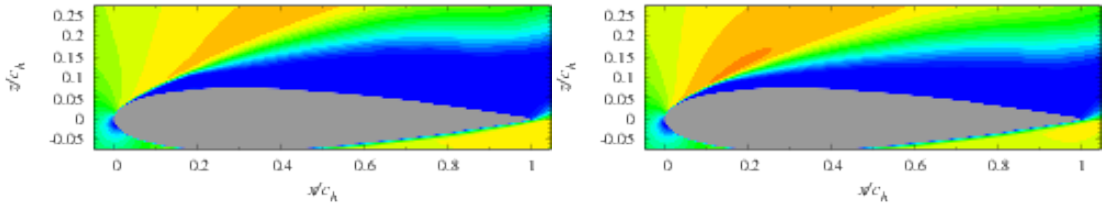

(e) $C_\mu = 2.00 \times 10^{-5}, F^+ = 1.0$ (SJ)

(f) $C_\mu = 5.15 \times 10^{-5}, F^+ = 1.0$ (PA)

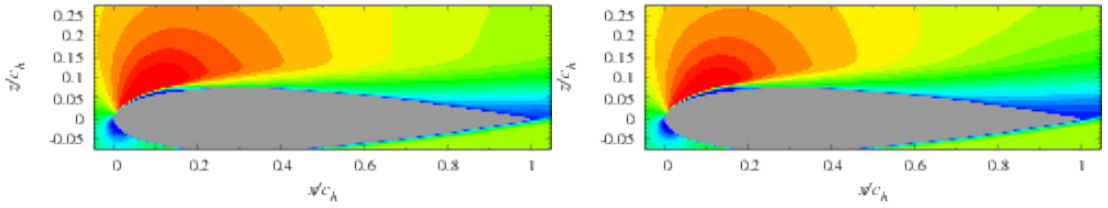

(g) $C_\mu = 2.00 \times 10^{-5}, F^+ = 6.0$ (SJ)

(h) $C_\mu = 5.15 \times 10^{-5}, F^+ = 6.0$ (PA)

Fig. 7.9: Time averaged fields of u/u_∞ for 0.0 to 1.5.

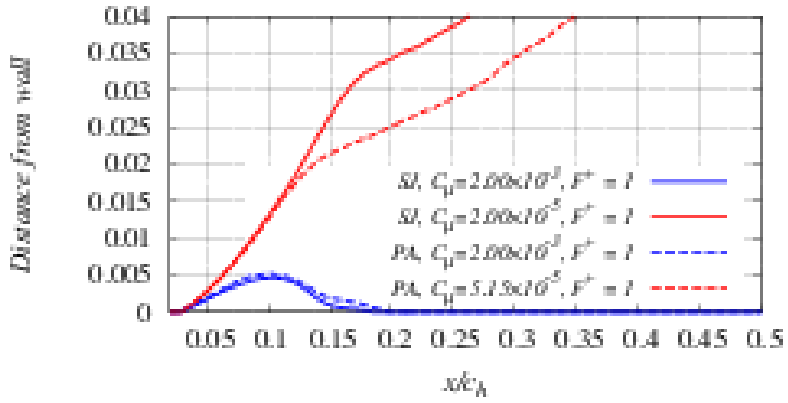

(a) $F^+ = 1.0$

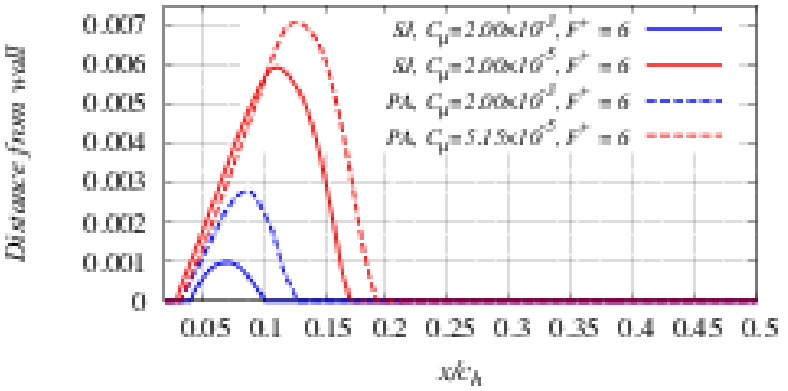

(b) $F^+ = 6.0$

Fig. 7.10: Reversed flow region near the leading edge: red lines show the case with $C_\mu = 2.0\times10^{-3}$; blue lines show the case with $C_\mu = 2.0\times10^{-5}$ for SJ and $C_\mu = 5.15\times10^{-5}$ for PA.

Fig. 7.11: Instantaneous flow field: contour plane is colored by chordwise velocity u/u_∞ for 0.0 to 1.5 ; isosurfaces is the second invariant of the velocity gradient tensor (colored by chordwise vorticity).

$F^+ = 1.0$ and 6.0 using the PA (Figs.7.12(a) and (b)) shows stronger periodic component at $x/c_h \simeq 0.5$ compared to the case using the SJ (Figs.4.18(a) and (b)). This is caused by the absense of the three-dimensional (spanwise-nonuniform) fluctuations introduced from the PA (see Sec.**??**: C.). Therefore, the two-dimensional vortex structure strongly remains farther in the case using the PA than SJ for these strong input cases, which would be related to the strength of the coherent vortex generated on the airfoil surface and the flow separation point near the trailing edge as discussed in Sec.**??** (see Fig.**??**). In the controllable and weak input momentum case ($C_\mu = 5.15 \times 10^{-5}$ with $F^+ = 6.0$: Fig.7.12(d)), the periodic component does not so much strongly appear that the turbulent component of the Reynolds shear stress is dominant similarlly to the case using the SJ (see Fig.4.18(d)). Therefore, totally speaking, an exchange of the chordwise momentum is mainly achived by the turbulent vortex structures regardless of devices in the present flow/actuator conditions although slight difference appears in the strength of periodic component when the input momenum is strong.

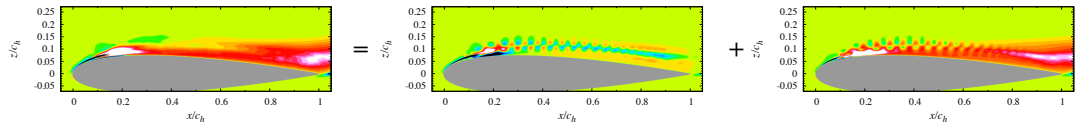

(a) $C_\mu = 2.00 \times 10^{-3}, F^+ = 1.0$ (PA)

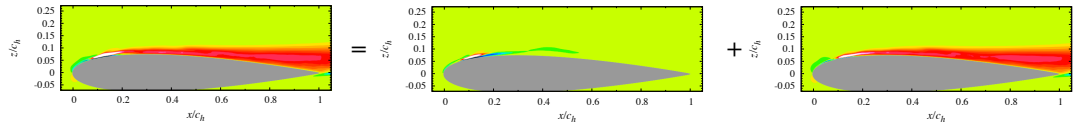

(b) $C_\mu = 2.00 \times 10^{-3}, F^+ = 6.0$ (PA)

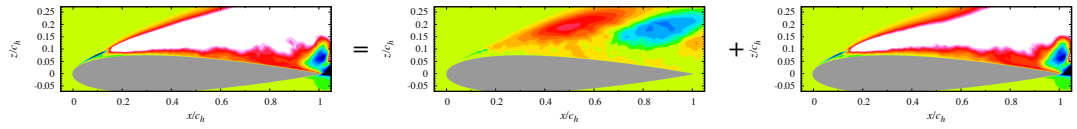

(c) $C_\mu = 5.15 \times 10^{-5}, F^+ = 1.0$ (PA)

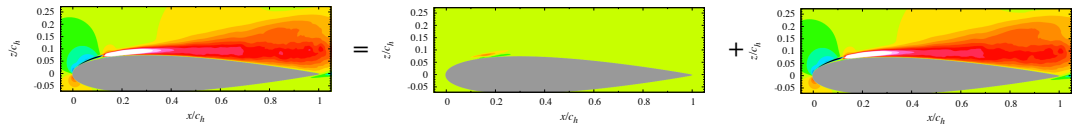

(d) $C_\mu = 5.15 \times 10^{-5}, F^+ = 6.0$ (PA)

Fig. 7.12: Spatial distribution of Reynolds shear stress $-\overline{u'w'}/u_\infty^2$. Reynolds shear stress is decomposed into periodic and turbulent (nonperiodic) components.

7.4.4 Coherent vortex structures and chordwise momentum exchange in phase-averaged flow fields

The following decomposition is conducted for the Reynolds shear stress at each phase angle (the phase angle was illustrated in Fig.4.10):

$$\langle u'w' \rangle_\varphi = \langle \tilde{u}\tilde{w} \rangle_\varphi + \langle u''w'' \rangle_\varphi. \tag{7.1}$$

Note that spanwise averaging procedure is also conducted but the symbol for this operation is omitted for the brevity. The detail of the computation of each Reynolds stress is explained in Sec.**??**. In Figs.7.13–**??**, the decomposition of the Reynolds shear stress is shown for the PA cases. The similar contours are shown in Figs.4.21–4.26 for the SJ cases. The black contour lines indicate the second invariant of the velocity gradient tensor, which corresponds to vortex structures with its axis along the spanwise (y) direction.

Similar to the cases using the SJ discussed in Sec.**??**, the 1) coherent vortex structures apper in the controllable cases with the period corresponding to the actuation frequency F^+. In addition, the 3) turbulent component of the Reynolds shear stress is dominant almost all over the airfoil surface, which is entrained by the coherent vortex structure convecting downstream. On the other hand, in the strong input cases, the 2) periodic component of the Reynolds shear stress appears more strongly than the cases using SJ (e.g., comparing Fig.4.21(a) and Fig.7.13(a) for the $F^+ = 1.0$ actuation). This is caused by the spanwise-uniform fluctuation introduced by the PA as discussed in the previous section. The strength of such coherent vortex would affect the entrainment of turbulent component of the Reynolds shear stress, e.g., the turbulent components around coherent vortex in Fig.7.13(c) and Fig.7.14(c) are stronger than those in Fig.4.21(c) and Fig.4.22(c). This would contribute to the larger exchange of the chordwise momentum in these strong input cases using PA, thus the aerodynamic performances are better in the PA than SJ (see blue lines in Fig.**??**). On the other hand, in the weak input/controllable cases, the difference does not significantly appear in the periodic component of the Reynolds shear stress and therefore the entrainment of the turbulent component around coherent vortex (see Fig.4.25(c) and Fig.**??**(c)). However, the distribution of turbulent component more widely spreads at $x/c_h \geq 0.5$ for farther from the airfoil surface in the PA than SJ (see Fig.4.25(c) and Fig.**??**(c)). This would be caused by the higher input frequency discussed

in Sec.??: D., which is the base frequnecy and burst modulation of the PA. The fluctuations of such higher frequencies can promote the turbulent transition and generate finer vortex structures compared to the case using the SJ, which will be more precisely discussed in the next section.

In summary, the mechanism of an exchange of the chordwise momentum based on the unsteady flow motion is almost the same between the SJ and PA cases, where the turbulent component of the Reynolds shear stress is dominant and entrained by large coherent vortex further downstream. On the other hand, in the strong input cases, the periodic component of the Reynolds stress and entrainment of turbulent component is slightly larger in PA than SJ due to spanwise-uniform fluctuation introduced from the PA.

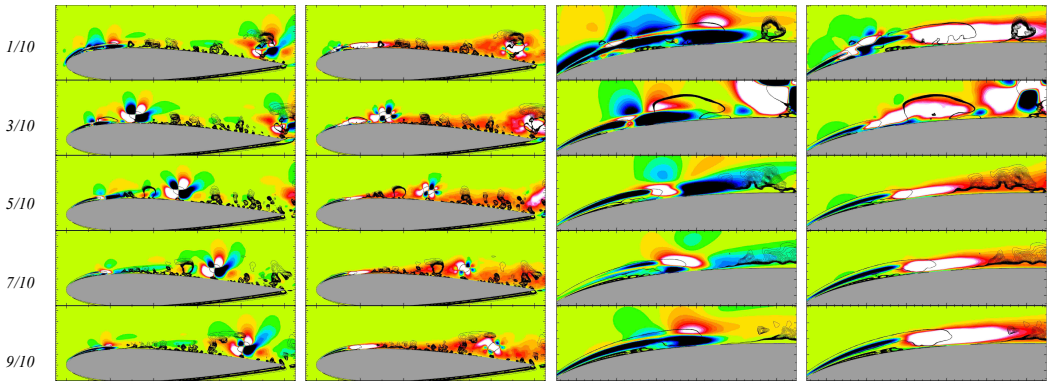

(b) Periodic (c) Turbulent (d) Periodic (e) Turbulent

Fig. 7.13: Coherent vortex structures and Reynolds shear stress: $C_\mu = 2.0 \times 10^{-3}, F^+ = 1.0$ case using the PA

7.5 Spatial development of the disturbances near the leading edge

In this section, the spatial growth rate of the wall-normal fluctuation is discussed by comparing the SJ and PA results. All the results of the SJ are the same in Sec.??.

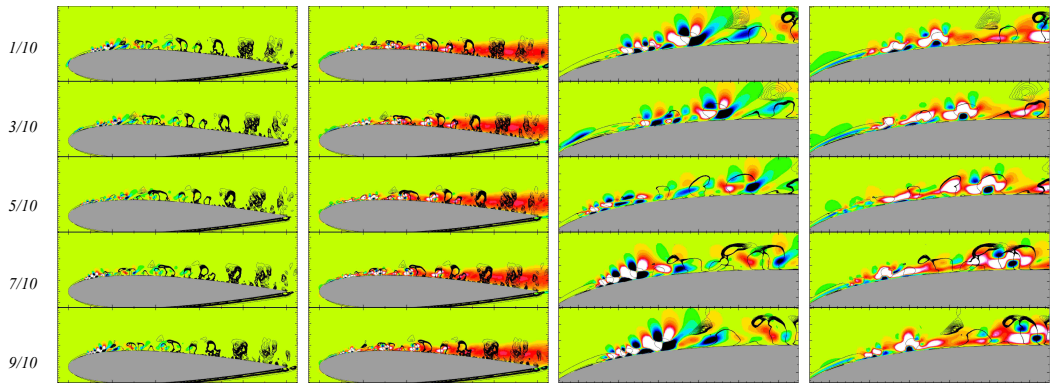

(b) Periodic (c) Turbulent (d) Periodic (e) Turbulent

Fig. 7.14: Coherent vortex structures and Reynolds shear stress: $C_\mu = 2.0 \times 10^{-3}, F^+ = 6.0$ case using the PA

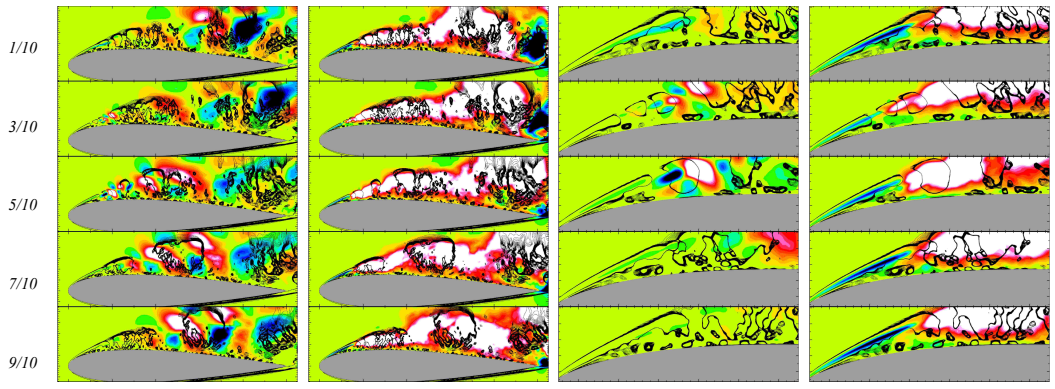

(b) Periodic (c) Turbulent (d) Periodic (e) Turbulent

Fig. 7.15: Coherent vortex structures and Reynolds shear stress: $C_\mu = 5.15 \times 10^{-5}, F^+ = 1.0$ case using the PA

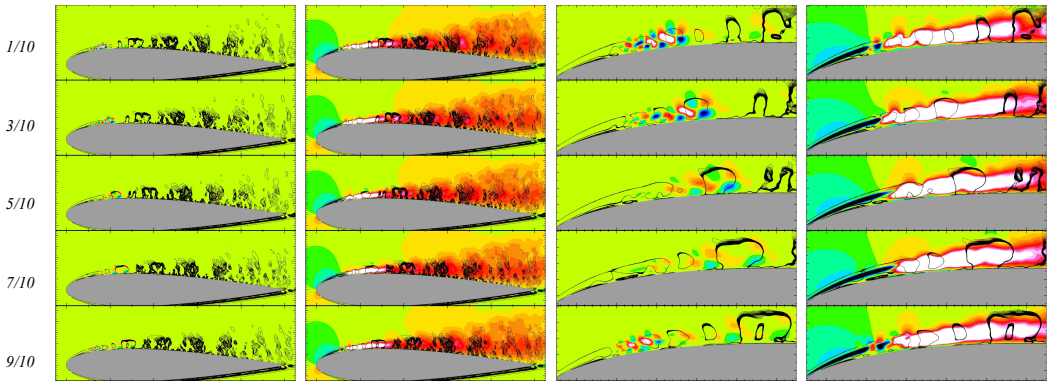

(b) Periodic (c) Turbulent (d) Periodic (e) Turbulent

Fig. 7.16: Coherent vortex structures and Reynolds shear stress: $C_\mu = 5.15 \times 10^{-5}$, $F^+ = 6.0$ case using the PA

7.5.1 Controllable cases

First, the two controllable cases with a strong input are discussed for each devices ($C_\mu = 2.0 \times 10^{-3}$ with $F^+ = 1.0$ and 10). Figure 7.17 shows the comparison of sptial growth rate α_i for LST and LES results. The details are explained in Sec.**??**. In the case with $F^+ = 1.0$ using the PA, the LST and LES data show good agreement at $x/c_h = 5\%$ in terms of the most unstable frequency $St \simeq 35$. At $x/c_h = 6\%$, the linear instability frequency is $St \simeq 30$ (red solid line), but the higher frequency modes $St \geq 60$ also shows comparable growth rate. At $x/c_h = 7\%$, the growth rate of lower frequencies is larger than that of the linear instability frequency. The transient sequence of spatial growth rate estimated by LST and LES data is similar to that discussed in Sec.**??** for the SJ, where linear, higher- and lower-nonlinear growth regimes appear. Similar trend is observed in the case with $F^+ = 10$ in Fig.7.17(c) and (d). On the other hand, the spatial growth rate of the case with $F^+ = 10$ is larger in PA than SJ (Fig.7.17(c) and (d)); and the spatial growth rate estimated by the LES data (black dots) are oscillating in the frequency (St) direction. This would be caused by the higher frequency modes introduced by the PA due to the burst actuation with higher base frequency. Figures 7.18 show the spatial growth rate α_i on a St-x plane for $0.0 \leq x/c_h \leq 0.2$. In this plot, the transient sequence of linear to nonlinear growth regime can be more clearly observed. In addition, it is also shown that the growth rate of the PA is larger than that of SJ in both of the LST and LES-data estimation.

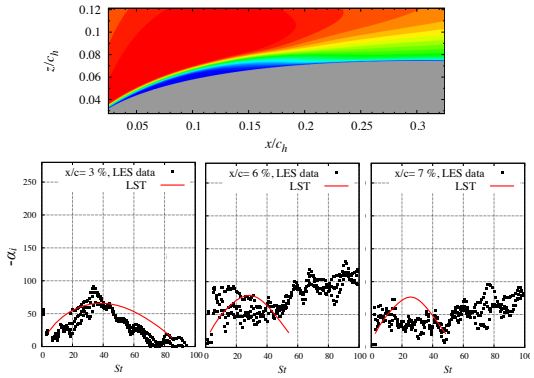

(a) $C_\mu = 2.0 \times 10^{-3}, F^+ = 1.0$, SJ

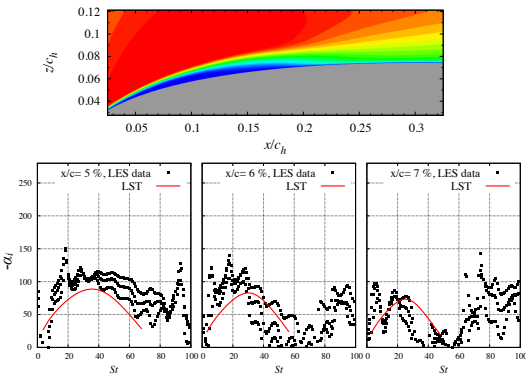

(b) $C_\mu = 2.0 \times 10^{-3}, F^+ = 1.0$, PA

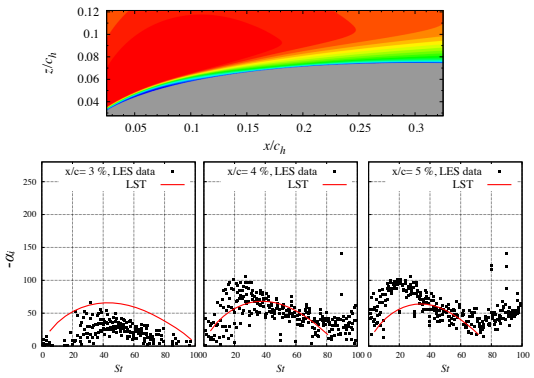

(c) $C_\mu = 2.0 \times 10^{-3}, F^+ = 10$, SJ

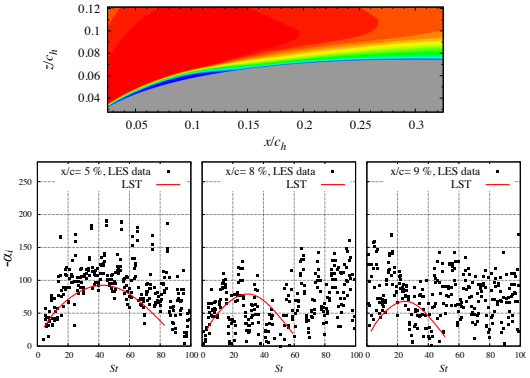

(d) $C_\mu = 2.0 \times 10^{-3}, F^+ = 10$, PA

Fig. 7.17: Controlled cases with a strong input momentum ($C_\mu = 2.0 \times 10^{-3}$): top figure shows time-averaged u/u_∞; bottom figures show the spatial growth rate α_i estimated by LST and FFT analysis for LES data.

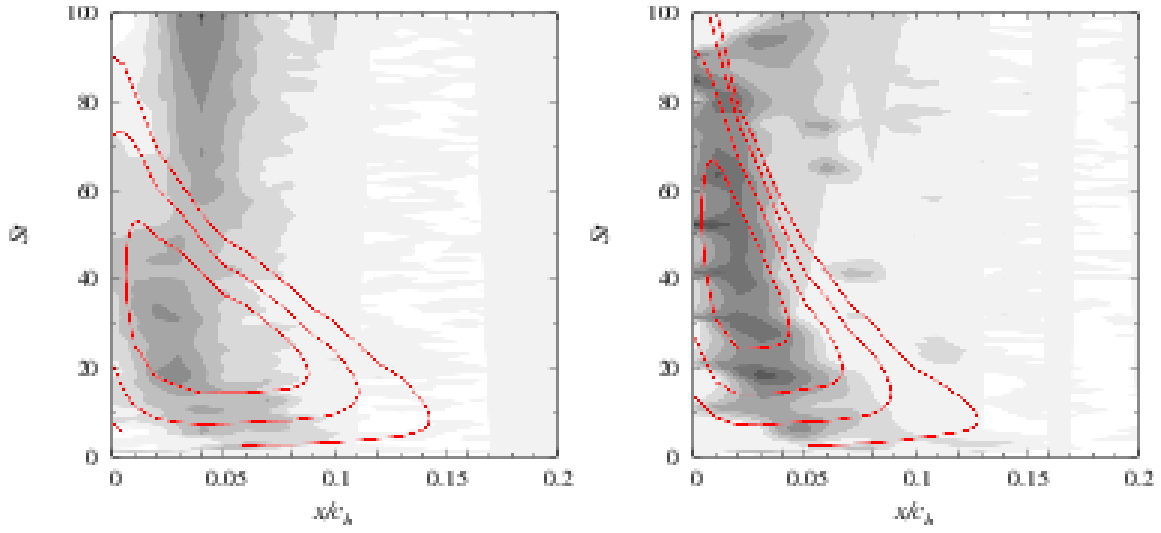

(a) $C_\mu = 2.0 \times 10^{-3}, F^+ = 1.0$, SJ

(b) $C_\mu = 2.0 \times 10^{-3}, F^+ = 1.0$, PA

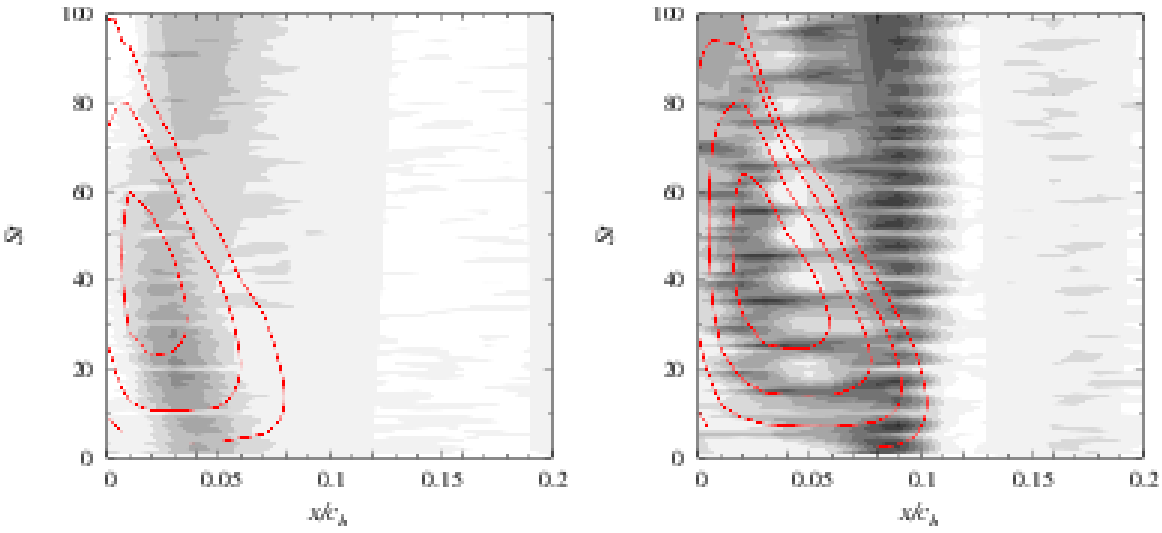

(c) $C_\mu = 2.0 \times 10^{-3}, F^+ = 10$, SJ

(d) $C_\mu = 2.0 \times 10^{-3}, F^+ = 10$, PA

Fig. 7.18: $C_\mu = 2.0 \times 10^{-3}$ cases: spatial distributions of α_i; black-to-white contour and red contour lines show LES and LST results, respectively ($0 \leq -\alpha_i \leq 50$).

Second, the controllable cases with a weak input are discussed for each devices ($C_\mu = 2.0 \times 10^{-5}$ for the SJ and $C_\mu = 5.15 \times 10^{-5}$ for the PA with $F^+ = 6.0$ and 10).

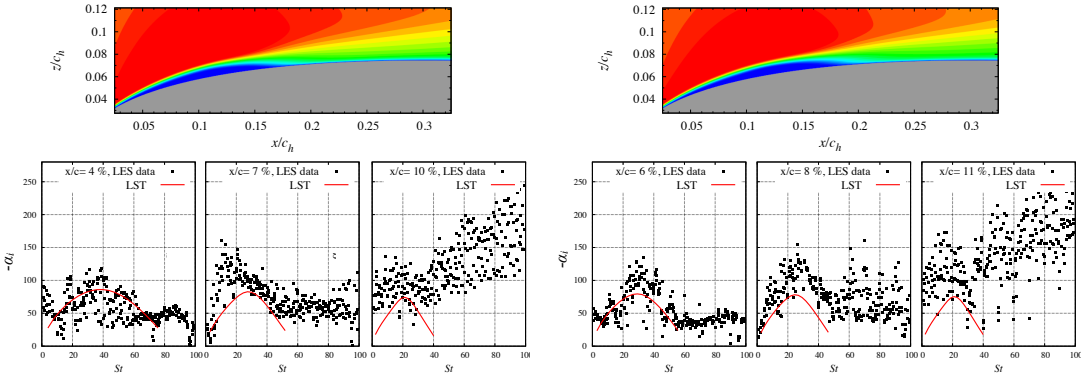

(a) $C_\mu = 2.0 \times 10^{-5}, F^+ = 6.0$, SJ

(b) $C_\mu = 5.15 \times 10^{-5}, F^+ = 6.0$, PA

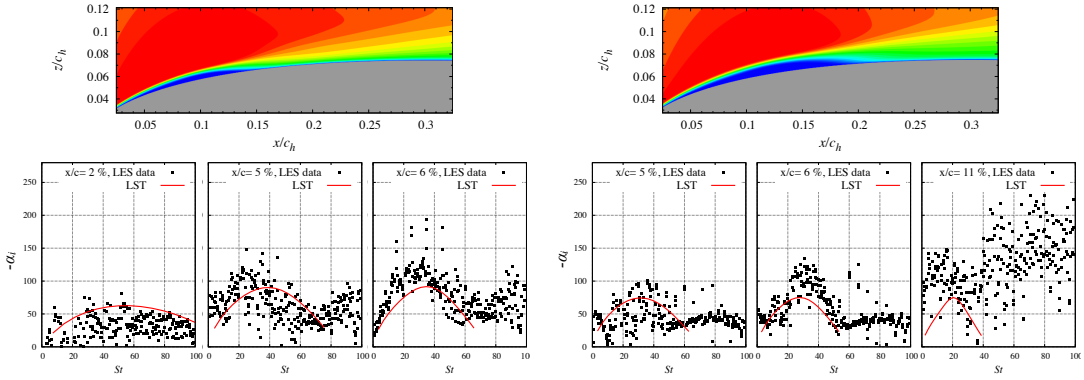

(c) $C_\mu = 2.0 \times 10^{-5}, F^+ = 10$, SJ

(d) $C_\mu = 5.15 \times 10^{-5}, F^+ = 10$, PA

Fig. 7.19: Controlled cases with a strong input momentum ($C_\mu = 2.0 \times 10^{-5}$): top figure shows time-averaged u/u_∞; bottom figures show the spatial growth rate α_i estimated by LST and FFT analysis for LES data.

7.5.2 Uncontrollable cases

7.6 Summary

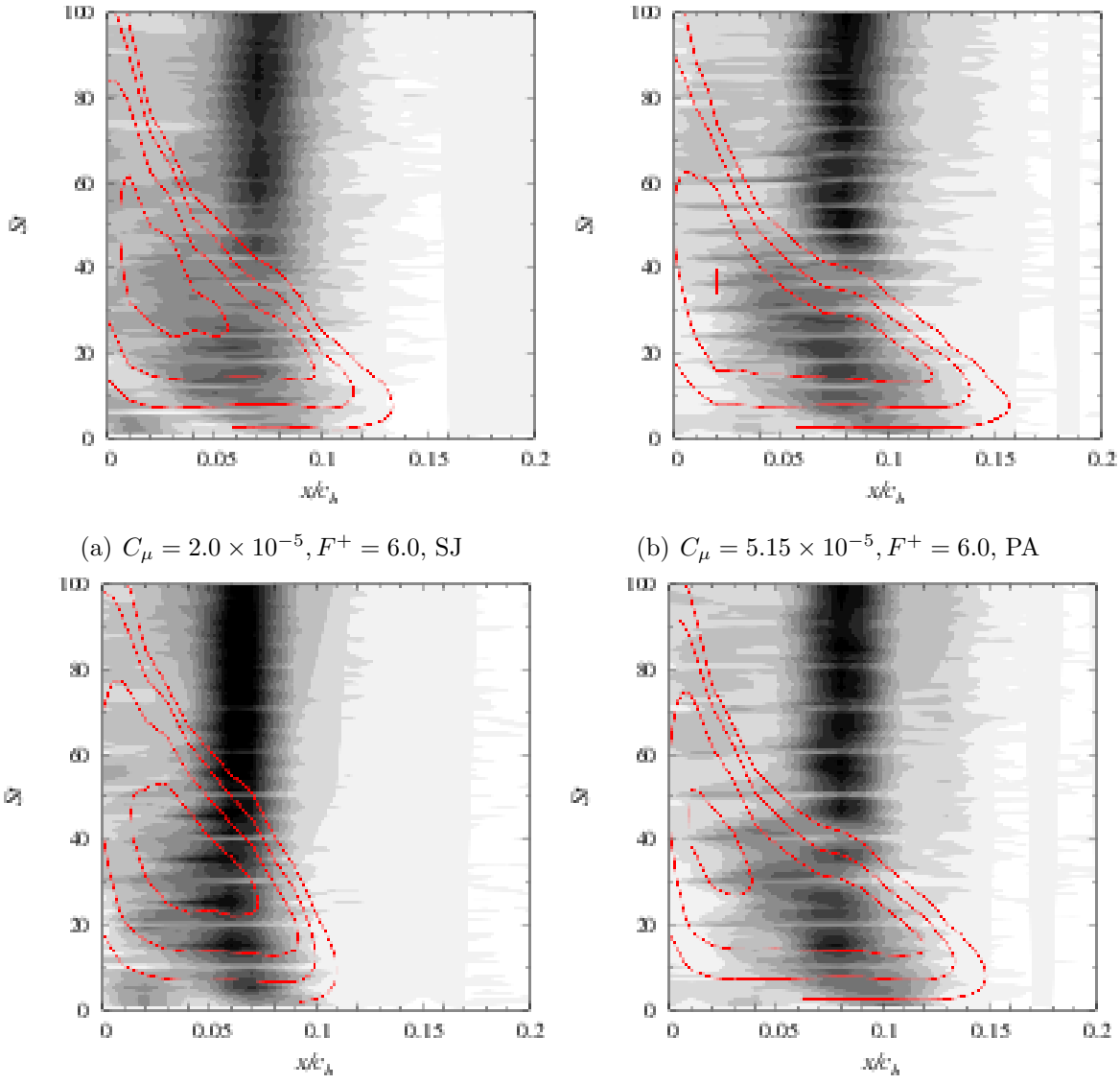

(a) $C_\mu = 2.0 \times 10^{-5}, F^+ = 6.0$, SJ

(b) $C_\mu = 5.15 \times 10^{-5}, F^+ = 6.0$, PA

(c) $C_\mu = 2.0 \times 10^{-5}, F^+ = 10$, SJ

(d) $C_\mu = 5.15 \times 10^{-5}, F^+ = 10$, PA

Fig. 7.20: $C_\mu = 2.0 \times 10^{-3}$ cases: spatial distributions of α_i; black-to-white contour and red contour lines show LES and LST results, respectively ($0 \leq -\alpha_i \leq 50$).

Chapter 8

Concluding remarks

The computation of separation control around NACA0015 airfoil with a synthetic jet (angle of attack is 12 [deg] and chord Reynolds number is 63,000) is conducted using 6th-order compact scheme.The effect of actuation frequency and position of the synthetic jet is arranged by varying the actuation frequency and position of the synthetic jet, and the control performance is surveyed in terms of aerodynamic coefficients. The controlled flow is investigated by time averaged fields, and the relation between separated regions on the suction surface and aerodynamic coefficients is discussed. The significant turbulent statistics is also extracted in terms of momentum addition in freestream direction by the mixing, and the related vortex structure is detected by phase-averaging procedure based on actuation frequency. The $u'w'$ component of Reynolds shear stress is especially focused in this thesis, and turbulent component is mainly enhanced almost all over the airfoil surface. In addition, two-dimensional vortex structure is extracted in phase and span-averaged flow fields, and the Reynolds shear stress is found to be locally enhanced between each vortex structure.

Bibliography

[1] Y. Abe, N. Iizuka, T. Nonomura, and K. Fujii. Conservative metric evaluation for high-order finite difference schemes with the gcl identities on moving and deforming grids. *Journal of Computational Physics*, 232:14–21, 2013.

[2] Y. Abe, K. Okada, T. Nonomura, and K. Fujii. The effects of actuation frequency on the separation control over an airfoil using a synthetic jet. *EUCASS Flight Physics Book*, 7, 2013.

[3] Y. Abe, K. Okada, M. Sato, T. Nonomura, and K. Fujii. Significance of three-dimensional unsteady flows inside the cavity on separated-flow control around an naca0015 using a synthetic jet. In *AIAA 2013-2748*, 2013.

[4] M. Amitay and A. Glezer. Role of actuation frequency in controlled flow reattachment over a stalled airfoil. *AIAA Journal*, 40(2):209–216, February 2002.

[5] H. Aono, S. Sekimoto, M. Sato, A. Yakeno, T. Nonomura, and K. Fujii. Computational and experimental analysis of flow structures induced by a plasma actuator with burst modulations in quiescent air. *Mechanical Engineering Journal*, 2, 2015.

[6] K. Asada. *Computational Analysis of the Flow Fields Induced by a DBD Plasma Actuator toward Separated-Flow Control*. PhD thesis, The University of Tokyo, 2014.

[7] K. Asada and K. Fujii. Computational analysis of unsteady flow-field induced by plasma actuator in burst mode. In *AIAA-2010-5090*, June 2010.

[8] H. Choi and P. Moin. Effects of the computational time step on numerical solutions of turbulent flow. *Journal of Computational Physics*, 113:1–4, 1994.

[9] J. F. Donovan, L. D. Kral, and A. W. Cary. Active flow control applied to an airfoil. In *AIAA-1998-210*, 1998.

[10] K. Fujii. Developing an accurate and efficient method for compressible flow simulations -example of cfd in aeronautics-. *The Proceedings: Fifth International Conference on Numerical Ship Hydrodynamics*, 1990.

[11] K. Fujii and T. Ogawa. Aerodynamics of high speed trains passing by each other. *Computers & Fluids*, 24:897–908, 1995.

[12] D. V. Gaitonde and M. R. Visbal. Padé-type higher-order boundary filters for the navier-stokes equations. *AIAA Journal*, 38(11):2103–2112, 2000.

[13] A. Glezer and M. Amitay. Synthetic jets. *Annual Review of Fluid Mechanics*, 34:503–529, 2002.

[14] D. Greenblatt and I. J. Wygnanski. The control of flow separation by periodic excitation. *Progress in Aerospace Sciences*, 36:487–545, 2000.

[15] I. Kaneda, S. Sekimoto, T. Nonomura, K. Asada, A. Oyama, and K. Fujii. An effective three-dimensional layout of actuation body force for separation control. *International Journal of Aerospace Engineering*, 2012, 2012.

[16] S. Kawai and K. Fujii. Compact scheme with filtering for large-eddy simulation of transitional boundary layer. *AIAA Journal*, 46(3):690–700, March 2008.

[17] J. Kim and H. J. Sung. Wall pressure fluctuations and flow-induced noise in a turbulent boundary layer over a bump. *Journal of Fluid Mechanics*, 558:79–102, 2006.

[18] S. K. Lele. Compact finite difference schemes with spectral-like resolution. *Journal of Computational Physics*, 103(1):16–42, 1992.

[19] M. A. McVeigh, H. Nagib, T. Wood, and I. Wygnanski. Full-scale flight tests of active flow control to reduce tiltrotor aircraft download. *Journal of Aircraft*, 48(3):786–796, 2011.

[20] R. B. Melville, S. A. Moiton, and D. P. Rizzetta. Implementation of a fully-implicit, aeroelastic navier-stokes solver. In *AIAA-1997-2039*, 1997.

[21] H. Nishida and T. Nonomura. Adi-sgs scheme on ideal magnetohydrodynamics. *Journal of Computational Physics*, 228:3182–3188, 2009.

[22] T. Nonomura, H. Aono, M. Sato, A. Yakeno, K. Okada, Y. Abe, and K. Fujii. Control mechanism of plasma actuator for separated flow around naca0015 at reynolds number 63,000 -separation bubble related mechanisms-. In *AIAA 2013-0853*, 2013.

[23] K. Okada, T. Nonomura, K. Fujii, and K. Miyaji. Computational analysis of vortex structures induced by a synthetic jet to control separated flows. *International Journal of Flow Control*, 4(1+2):47–65, June 2012.

[24] K. Okada, A. Oyama, K. Fujii, and K. Miyaji. Computational study on effect of synthetic jet design parameters. *International Journal of Aerospace Engineering*, 2010, 2010.

[25] K. Okada, A. Oyama, K. Fujii, and K. Miyaji. Computational study of effects of nondimensional parameters on synthetic jets. *Transactions of the Japan Society for Aeronautical and Space Sciences*, 55(1):1–11, 2012.

[26] B. R. Ravi, R. Mittal, and F. M. Najjar. Study of three-dimensional synthetic jet flowfields using direct-numerical simulation. In *AIAA-2004-91*, 2004.

[27] M. Sato, T. Nonomura, K. Okada, K. Asada, H. Aono, A. Yakeno, Y. Abe, and K. Fujii. Mechanisms for laminar separated-flow control using dbd plasma actuator at low reynolds number. *Physics of Fluids (Accepted for publication)*, 2015.

[28] M. Sato, K. Okada, T. Nonomura, H. Aono, A. Yakeno, K. Asada, and K. Fujii. Multifactorial effects of operating conditions of dielectric-barrier-discharge plasma actuator on laminar-separated-flow control. In *AIAA journal*, 2015.

[29] S. Teramoto. *Computational Study on the Dynamic Stability of a Blunt Reentry Capsule at Transonic Speeds*. PhD thesis, The Institute of Space and Astronautical Science, 2 2000.

[30] M. R. Visbal and D. V. Gaitonde. Computation of aeroacoustic fields on general geometries using compact differencing and filtering schemes. In *AIAA-1999-3706*, 1999.

[31] M. R. Visbal and D. V. Gaitonde. On the use of higher-order finite-difference schemes on curvilinear and deforming meshes. *Journal of Computational Physics*, 181(1):155–185, 2002.

[32] M. R. Visbal and D. P. Rizzetta. Large-eddy simulation on general geometries using compact differencing and filtering schemes. In *AIAA-2002-288*, 2002.

[33] D. You and P. Moin. Active control of flow separation over an airfoil using synthetic jets. *Journal of Fluids and Structures*, 24:1349–1357, 2008.

[34] W. Zhang and R. Samtaney. A direct numerical simulation investigation of the synthetic jet frequency effects on separation control of low-re flow past an airfoil. *Physics of Fluids*, 2015.

Appendix A

8.1 Basic characteristics of noncontrolled flows

In this section, the basic characteristics of noncontrolled flows are discussed. The cases of $AoA = 12$ and 10 [deg.] are described. The noncontrolled case of $AoA = 12$ [deg.] is the baseline flow for the separation control throughout this thesis. The case of $AoA = 10$ [deg.] is the attached flow with a laminar separation bublle near the leading edge, which is refered in Sec.**??** for the comparison with the controlled flow in terms of spatial development of disturbances.

8.1.1 Time-averaged fields

Pressure coefficient and skin friction

Chordwise velocity fields

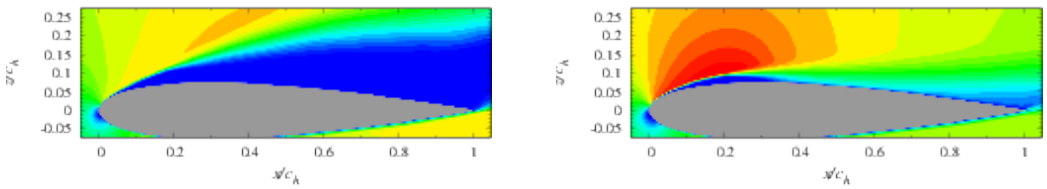

(a) $AoA = 12$ deg. (b) $AoA = 10$ deg.

Fig. 8.1: Chordwise velocity field (u/u_∞) of noncontrolled cases: $0.0 \leq u/u_\infty \leq 1.5$

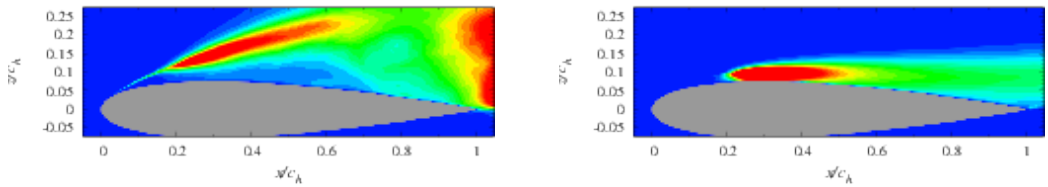

(a) $AoA = 12$ deg. (b) $AoA = 10$ deg.

Fig. 8.2: Turbulent kinetic energy of noncontrolled cases: $0.0 \leq u/u_\infty \leq 1.5$

Reversed flow region

Turbulent kinetic energy

8.1.2 Unsteady characteristics

PSD of wall-normal velocity component

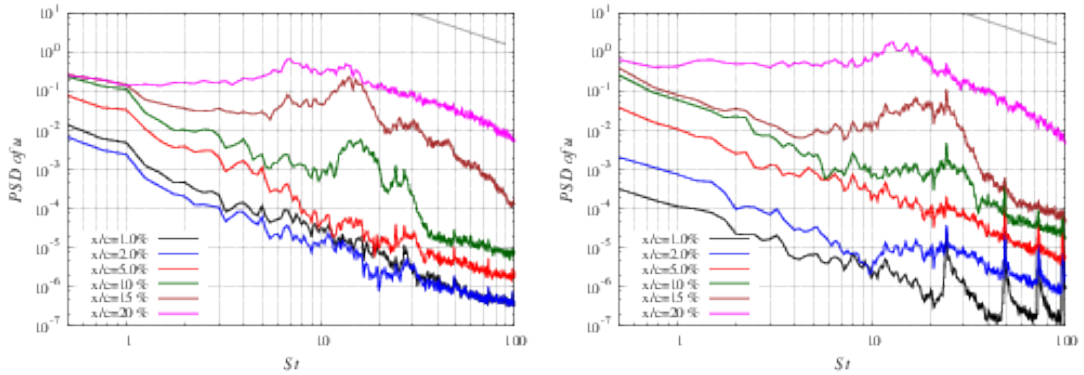

(a) $AoA = 12$ deg. (b) $AoA = 10$ deg.

Fig. 8.3: Power spectra of wall-normal velocity component; the horizontal axis is a frequency normalized by freestream velocity and chord length. The straight line in grey color shows the Kolmogorov's 5/3 law.

The coherent vortices are emitted from the separation bubble at $x/c_h \simeq 20\%$, where the $St = 15$ and 12 show the peak of the $AoA = 14$ and 12 [deg.] cases, respectively. Therefore, the phase decomposition will be conducted based on the $St = 15$ and 12 for each cases for discussion on the unsteady flow motion at the edge of the separated shear layer.

Instantaneous flow fields

Figure 8.4 shows the closed view of instantaneous flows at each phase angle ($\varphi/2\pi$ = $1/10, 3/10, 5/10, 7/10$, and $9/10$).

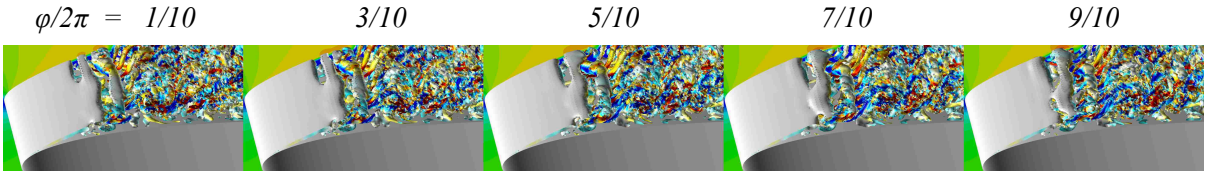

(b) $AoA = 12$ deg.

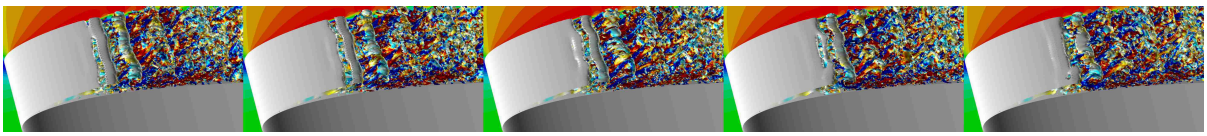

(c) $AoA = 10$ deg.

Fig. 8.4: Instantaneous flow fields (u/u_∞): $0.0 \leq u/u_\infty \leq 1.5$

Phase-averaged flows

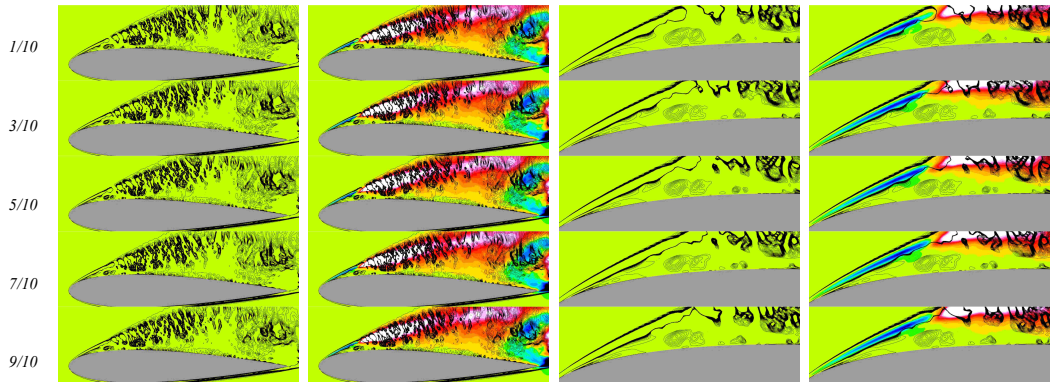

(b) Periodic (c) Turbulent (d) Periodic (e) Turbulent

Fig. 8.5: Coherent vortex structures and Reynolds shear stress: $AoA = 12$ [deg.] case

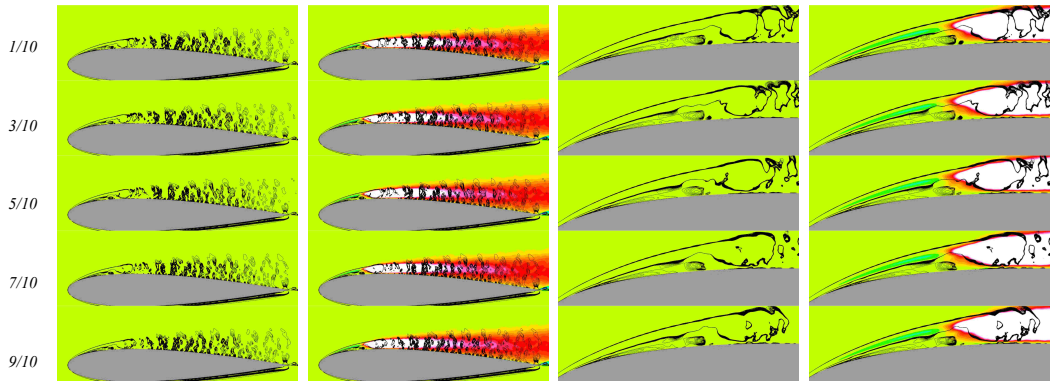

(b) Periodic (c) Turbulent (d) Periodic (e) Turbulent

Fig. 8.6: Coherent vortex structures and Reynolds shear stress: $AoA = 10$ [deg.] case